

Accepted Manuscript

Continuous SiC Fiber, CVI SiC Matrix Composites for Nuclear Applications:
Properties and Irradiation Effects

Yutai Katoh, Kazumi Ozawa, Chunghao Shih, Takashi Nozawa, Robert J.
Shinavski, Akira Hasegawa, Lance L. Snead

PII: S0022-3115(13)00864-7

DOI: <http://dx.doi.org/10.1016/j.jnucmat.2013.06.040>

Reference: NUMA 47578



To appear in: *Journal of Nuclear Materials*

Please cite this article as: Y. Katoh, K. Ozawa, C. Shih, T. Nozawa, R.J. Shinavski, A. Hasegawa, L.L. Snead, Continuous SiC Fiber, CVI SiC Matrix Composites for Nuclear Applications: Properties and Irradiation Effects, *Journal of Nuclear Materials* (2013), doi: <http://dx.doi.org/10.1016/j.jnucmat.2013.06.040>

This is a PDF file of an unedited manuscript that has been accepted for publication. As a service to our customers we are providing this early version of the manuscript. The manuscript will undergo copyediting, typesetting, and review of the resulting proof before it is published in its final form. Please note that during the production process errors may be discovered which could affect the content, and all legal disclaimers that apply to the journal pertain.

**Continuous SiC Fiber, CVI SiC Matrix Composites for Nuclear Applications:
Properties and Irradiation Effects**

| | |
|-------------------------------|--|
| Submitted to: | Journal of Nuclear Materials |
| Date initially submitted: | April 8, 2013 |
| Date Revision 1 is submitted: | June 18, 2013 |
| Corresponding author: | Dr. Yutai Katoh Materials Science and Technology Division Oak Ridge National Laboratory P.O. Box 2008, Oak Ridge, TN 37831-6138, USA E-mail: katohy@ornl.gov Phone: +1 (865) 576-5996 |
| Complete list of authors: | Yutai Katoh, Oak Ridge National Laboratory, USA Kazumi Ozawa, Oak Ridge National Laboratory, USA (currently at Japan Atomic Energy Agency, Japan) Chunghao Shih, Oak Ridge National Laboratory, USA Takashi Nozawa, Oak Ridge National Laboratory, USA (currently at Japan Atomic Energy Agency, Japan) Robert J. Shinavski, Hyper-Therm High Temperature Composites, Inc., USA Akira Hasegawa, Tohoku University, Japan Lance Snead, Oak Ridge National Laboratory, USA |
| Key words: | SiC/SiC composite, irradiation effect, mechanical properties, thermo-physical properties, design methodology |

Significance of the work:

Silicon carbide composites are materials of high interest for nuclear and fusion energy applications. This paper provides a summary compilation of the properties of nuclear-grade silicon carbide composites, specifically those with the chemically vapor-infiltrated (CVI) SiC matrices, including newly obtained results. The properties discussed are both in unirradiated condition and after neutron irradiation to intermediate fluence levels at 300–1300°C.

Continuous SiC Fiber, CVI SiC Matrix Composites for Nuclear Applications: Properties and Irradiation Effects

Yutai Katoh¹, Kazumi Ozawa^{1,*}, Chunghao Shih¹, Takashi Nozawa^{1,*}, Robert J. Shinavski², Akira Hasegawa³, Lance L. Snead¹

¹ Oak Ridge National Laboratory, Oak Ridge, Tennessee, USA

² Hyper-Therm High Temperature Composites, Inc., Huntington Beach, California, USA

³ Tohoku University, Sendai, Miyagi-ken, Japan

* Currently at Japan Atomic Energy Agency, Rokkasho, Aomori-ken, Japan

Abstract

Silicon carbide (SiC) continuous fiber-reinforced, SiC-matrix composites (SiC/SiC composites) are industrially available materials that are promising for applications in nuclear environments. The SiC/SiC composites consisting of near-stoichiometric SiC fibers, stoichiometric and fully crystalline SiC matrices, and the pyrocarbon (PyC) or multilayered PyC/SiC interphase between the fiber and the matrix are considered particularly resistant to very high radiation environments. This paper provides a summary compilation of the properties of these composites, specifically those with the chemically vapor-infiltrated (CVI) SiC matrices, including newly obtained results. The properties discussed are both in unirradiated condition and after neutron irradiation to intermediate fluence levels (most data are for <~10 displacement per atom) at 300–1300°C.

1 Introduction

Silicon carbide (SiC) is an engineering ceramic material that uniquely combines strength and chemical inertness up to very high temperatures. SiC materials in stoichiometric and crystalline forms have exhibited unique and exceptional stability in high radiation environments, in addition to the known low induced-activation / low after-heat properties, making them particularly attractive for use in harsh radiation environments [1-4]. Although monolithic SiC is a brittle ceramic, continuous SiC fiber-reinforced SiC-matrix composites (SiC/SiC, SiC_f/SiC, or SiC_f/SiC_m composites) offer enhanced reliability with predictable mechanical properties and greatly increased damage tolerance in addition to the above-mentioned inherent advantages of SiC, allowing use of these materials for structural applications [5].

Certain SiC/SiC composites that are made for enhanced radiation resistance are specifically referred to as the nuclear-grade SiC/SiC composites. The nuclear-grade SiC/SiC composites are considered attractive and promising materials for components for light water reactor (LWR) fuel cladding and channel boxes [6, 7], fuel and in-vessel components for advanced fission reactors such as high-temperature gas-cooled reactors (HTGR's) [8, 9], fluoride-salt-cooled high-temperature reactors (FHR's) [10], and gas-cooled fast reactors (GFR's) [11, 12], future fusion energy [2, 13, 14], and other extreme radiation services. The current nuclear-grade SiC/SiC composites consist of (near-) stoichiometric and crystalline beta-phase SiC for both fibers and matrices and the minimal amount of less-radiation-stable material for the debond/sliding layer(s) between the fibers and the matrices, often referred to as the interphase. Currently nuclear-grade SiC/SiC composites are commercially available on a custom-order basis from a fair number of vendors worldwide.

Recently, Oak Ridge National Laboratory completed the post-irradiation examination campaign for the US/Japan collaborative RB-18J experiment, which involved the most comprehensive irradiation of the advanced SiC/SiC composites that were available at the time of preparatory phase. In this experiment, a variety of nuclear-grade SiC/SiC composites were evaluated for various mechanical and thermo-physical properties before and after neutron irradiation. The first objective of this paper is to report and discuss the result of this experiment for the chemically vapor-infiltrated (CVI) SiC-matrix composites. In addition to the results from the RB-18J experiment, this paper attempts to provide a summary compilation of the properties of nuclear-grade SiC/SiC composites, specifically those with the CVI SiC matrices as the reference materials, with the intention to serve the increasing need for the baseline and

irradiated properties data for nuclear-grade SiC/SiC for prospective applications in LWR's, advanced fission reactors, and future fusion energy systems.

2 Materials

2.1 Constituents for Nuclear-Grade SiC/SiC

As briefly described above, constituents that possess adequate resistance against neutron irradiation make up nuclear-grade SiC/SiC composite materials. In addition to irradiation tolerance, essential requirements of nuclear-grade materials generally include a sufficiently small neutron cross-section and chemical compatibility with the coolant and fuel systems. However, discussion of chemical compatibility requirements and issues will be left out of this paper's scope because they are very specific to the coolant and fuel systems of interest.

Among the common materials used to make continuous fiber ceramic matrix composites, stoichiometric and crystalline SiC is known to be irradiation resistant. Polycrystalline beta-phase SiC has successfully been used as the coating material for TRISO fuel since the 1960's [15]. Since then, substantial work has been performed to examine the effects of neutron irradiation on this material with most of the results positively addressing its exceptional irradiation resistance [16, 17]. Although some alpha-phase SiC-based ceramics have proved reasonable irradiation resistance in certain conditions, they are not the preferred materials over cubic beta-phase materials because under irradiation the hexagonal crystallites in general tend to experience anisotropic swelling, often causing eventual intergranular cracking. Pramono et al. report isotropic and anisotropic swelling of 6H-SiC with and without the presence of transmutation helium, respectively [18]. Carbon materials are less stable than SiC in severe radiation environments; however, they have proven to retain adequate mechanical properties up to tens of dpa at elevated temperatures [19-22]. Based on the understanding above, composites with near-stoichiometric SiC fibers, stoichiometric polycrystalline beta-phase SiC matrices, and carbon interphase composites are currently considered the primary nuclear-grade SiC/SiC. Properties of the reinforcing fibers, interphase, and matrices are equally important in determining the overall properties of the composites.

2.1.1 Reinforcement and Architecture

The SiC fibers that are commercially available are produced based on the polymer precursor process first introduced by Yajima [23] and later made commercially available by Yajima's

successors under the trade names Nicalon™ and Tyranno Fiber™. The first stage of these fiber processes involves the low-temperature melt-spinning of the polycarbosilane (PCS) or polytitanocarbosilane (PTCS) polymer. These green state fibers are then cured at elevated temperature either by exposure to oxygen or through electron beam curing and then successively ceramized in an inert atmosphere. Because of their relatively low price, good mechanical properties, and excellent weavability, these Generation I SiC fibers have found widespread use both in the laboratory as well as in industry. Typical appearances of the SiC fiber and the two-dimensionally (2D) woven fabric are shown in Figure 1.

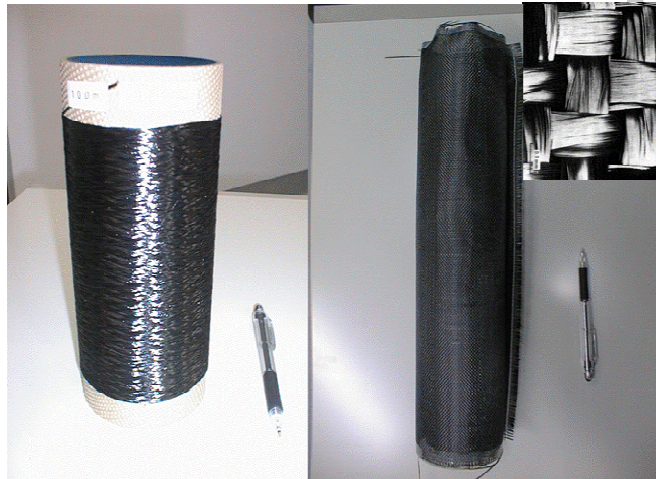


Figure 1. Polymer-derived multi-filament SiC fiber tow (left) and 2D fabric (right). Inset shows a close-up view of 2D fabric of ceramic-grade Nicalon fibers.

It is important to note that due to the presence of excess oxygen and carbon, these Generation I fibers are more correctly classified as SiC-based fibers, rather than SiC fibers. For example, the original “ceramic-grade” Nicalon is 65 % SiC with 23 % SiO₂ and 11 % free carbon [24]. The SiC crystallites are extremely small or poorly crystallized, and set in a continuum of glassy Si-O_x-C_y phase. Because of the presence of these silica and carbon phases, these fibers undergo structural instability accompanying substantial volumetric contraction when exposed to radiation by high-energy neutrons or particles. As a result, SiC/SiC composites with the Generation I fibers exhibited a major loss of strength arising from extensive fiber-matrix debonding [25-27]. In the next-generation Hi-Nicalon™ fiber, the relative amount of oxygen was reduced to less than 1% by cross-linking the green fiber with ionizing radiation. However, radiation tolerance was improved only moderately in the Generation II SiC because of the radiation-unstable microstructure still consisting of SiC nano-crystallites embedded in a continuum of carbon [24, 28].

The Generation III SiC fibers are defined by near-stoichiometric chemical composition and crystallinity that is largely enhanced beyond the Generation II, in addition to the reduced oxygen content. These features are achieved by various high-temperature processes including thermochemical decarburation treatment and sintering with additives such as alumina and boron. Commercially available Generation III SiC fibers include Hi-Nicalon Type S (Nippon Carbon Co., Tokyo, Japan, "HNLS" hereafter) [24, 29, 30], Tyranno SA3 (Ube Industries, Ltd., Ube, Japan, "SA3" hereafter) [31], Sylramic™ (COI Ceramics, San Diego, CA) [32], and CefNITE™ (IEST Co., Ltd., Moriyama, Japan) [33].

The Generation III SiC fibers consist primarily of beta-phase SiC grains of sizes typically ranging from tens to hundreds of nanometers and excess carbon as poorly graphitized carbon pockets in multi-grain junctions [28]. The grain sizes in the fibers are reflected in the surface roughness, as shown in Figure 2, where the very smooth surface of nanocrystalline Hi-Nicalon contrasts with the less smooth surface of HNLS fiber and the obviously more rugged surface of SA3 fiber. These surface roughness features reportedly influence the interfacial shear debond criteria and frictional stress [34, 35]. The early Generation III SiC fibers, HNLS and SA3, have been evaluated and positively addressed for neutron resistance in various irradiation conditions as composite reinforcements and as bare fibers [36-38]. It should be noted, however, the excess carbon, sintering additives, and impurities may adversely influence the stability of these fibers in more aggressive irradiation conditions than previously reported.

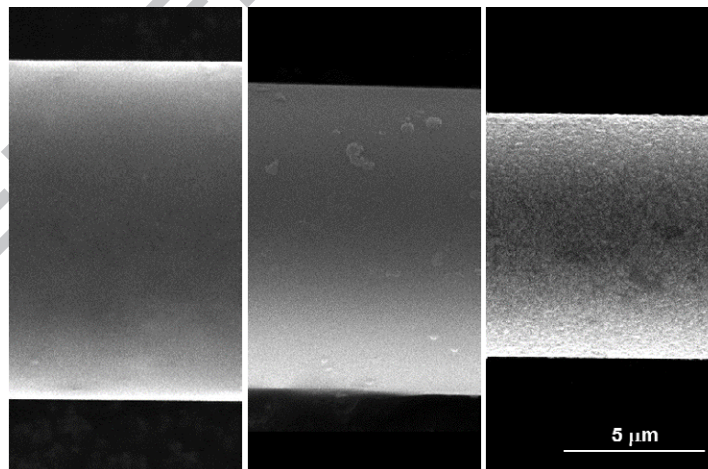


Figure 2. SEM images of surfaces of Hi-Nicalon (left), Hi-Nicalon Type S (middle), and Tyranno SA3 (right) fibers.

Properties of the representative SiC(-based) fibers are compared in Table 1. Because of the enhanced stoichiometry and crystallinity, the Generation III fibers possess higher elastic

modulus and thermal conductivity, smaller elongation, a coefficient of thermal expansion (CTE) that is close to that of pure beta-SiC, and often increased surface roughness as mentioned above. Because of these differences, certain mechanical, physical, and thermal properties of composites with the Generation III SiC fibers are substantially different from those of previous generation SiC fiber composites.

Table 1. Properties of commercially available near-stoichiometric SiC fibers and comparison with representative non-stoichiometric SiC-based fibers.

| Trade Name | CG-Nicalon NL-202 | Hi-Nicalon | Hi-Nicalon Type S | Tyranno SA3 | Sylramic | Pure β SiC. |
|------------------------------|-------------------|------------|-------------------|------------------|------------------|-----------------------|
| Manufacturer | NCK ¹ | NCK | NCK | Ube ² | COI ³ | |
| SiC Fiber Generation | I | II | III | III | III | (CVD SiC) |
| C/Si Atomic Ratio | 1.31 | 1.39 | 1.05 | 1.07 | 1.00 | 1.00 |
| Oxygen Mass Concentration | 11.7% | 0.5% | 0.2% | <1% | 0.8% | 0% |
| Other Additives | | | | Al | B, N, Ti | |
| SiC Grain Size | ~2 nm | ~10 nm | ~50 nm | ~200 nm | ~100 nm | |
| Young's Modulus, RT [GPa] | 220 | 270 | 420 | 380 | 380 | 450 |
| Tensile Strength, RT [GPa] | 3.0 | 2.8 | 2.6 | 2.8 | 3.2 | ~0.4 ⁴ |
| Elongation | 1.4% | 1.0% | 0.6% | 0.7% | 0.8% | ~0.1% ⁴ |
| Density [g/cm ³] | 2.55 | 2.74 | 3.10 | 3.10 | 3.0-3.1 | 3.21 |
| CTE [ppm/K], to 500°C | 3.2 | 3.5 | 5.1 | 4.5 ⁵ | 5.4 ⁵ | 3.9, 4.5 ⁵ |
| Thermal Cond., RT [W/m-K] | 3.0 | 7.8 | 18.4 | 65 | 46 | ~<400 ⁶ |

1: Nippon Carbon (Tokyo, Japan), 2: Ube Industry (Ube, Japan), 3: COI Ceramics (San Diego, CA), 4: Strength and elongation of monolithic SiC widely vary depending on effective surface and machining, 5: to 1000°C, 6: Thermal conductivity of SiC varies significantly depending on purity and grain size.

Given certain properties for the constituent materials, the composite properties are determined by the fiber architecture. Obviously the reinforcing fibers provide benefits such as strength and toughness most effectively in directions parallel to the fiber axis. More precisely, the composite properties are to a large extent determined by the volume fractions and orientations of the fibers in relation with the orientation of interest for certain properties.

Two-dimensional (2D) woven architectures, including plain-weave (PW) and satin-weave (SW, most commonly 5-harness and 8-harness), are most commonly used to make planar components. A choice between PW and SW usually does not impose significant impact on the composite properties. The 0°/90° stacking of orthogonally woven fabrics results in orthotropic properties, whereas the 0°/±30° stacking, for example, allows more isotropic in-plane

properties at the expense of somewhat reduced on-axis strength. The materials discussed in this work are mostly 2D composites. Among non-2D architectures, the uni-directional (UD) architecture is often useful to enable high strength in one direction as well as to produce model composite samples for research purposes. Orthogonal three-dimensional (3D) architectures with various x:y:z fiber ratios are utilized to tailor anisotropic properties three-dimensionally. Braiding can also be employed to produce 3-D tubular geometries. However, the properties of braided components approach 2D when wall thickness is small compared to the tube diameter. More complex architectures have also been developed and used for specific purposes.

2.1.2 Interphase

The roles of interphases to accommodate adequate fiber-matrix load transfer, debond, and sliding are very important for continuous fiber ceramic matrix composites. For SiC/SiC composites, interphases of PyC, boron nitride (BN), and multilayer PyC/SiC or BN/SiC are most commonly applied as the coating onto the fiber surfaces before the matrix densification [5]. With regard to the fast fracture properties, multilayer interphase composites behave in a similar manner to monolayer interphase composites, with the innermost PyC or BN layer acting mostly as the sole interphase [39, 40]. However, multilayer interphases are known to provide extra rupture life in oxidative environments [40]. Moreover, multilayer interphases reportedly impose substantial effects on the through-thickness electrical conductivity [41].

BN interphase is generally considered inadequate for nuclear applications, unless isotopically separated boron is used, due to the rapid transmutation of ^{10}B under neutron irradiation. For this reason, PyC is commonly used as the interphase material by itself or in combination with SiC to form the multilayer interphase. The PyC interphase is typically formed by chemical vapor deposition (CVD) onto the fiber surface using a gaseous hydrocarbon precursor in an isothermal, isobaric condition. Examples of the monolayer PyC and multilayer PyC/SiC interphases in SiC/SiC composites are shown in Figure 3. Carbon materials including PyC are known to undergo moderate, yet substantial, irradiation effects including early contraction followed by swelling, eventually leading to amorphization at temperatures of typical technological interest [19, 20, 42]. This radiation instability of PyC presents an opportunity for the development of an alternative interphase for SiC/SiC composites for radiation services. Interestingly, however, PyC interphase SiC/SiC composites have been shown to retain adequate mechanical properties and fracture behavior to high neutron fluence levels where very significant radiation damage is expected in carbon [43].

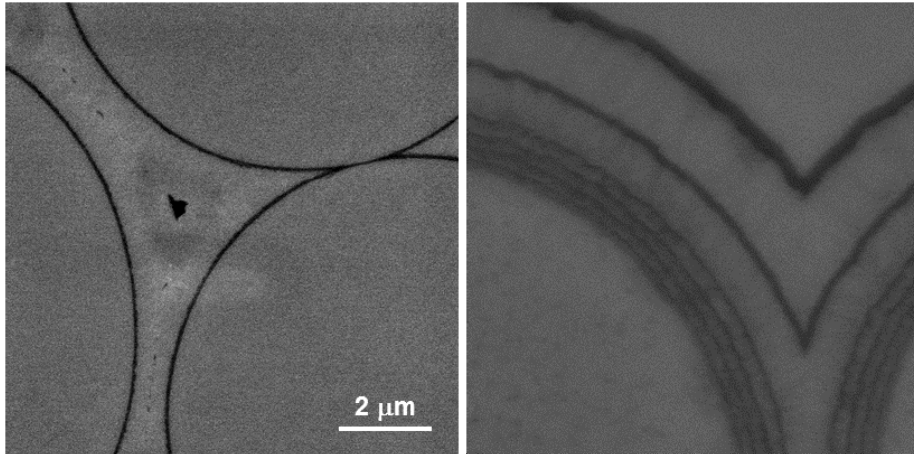


Figure 3. Backscattered electron images of monolayer pyrocarbon (PyC) and multilayer PyC/SiC interphases in SiC/SiC composites.

The typical thickness of PyC interphase ranges between ~20 nm (for the case of the innermost layer in the multilayer interphase) and ~500 nm. It is generally understood that an interphase that is too thin results in brittle failure, even for composites, due to excessive frictional stress at the fiber-matrix interface. Alternatively, an interphase that is too thick tends to compromise strength due to insufficient load transfer between the fiber and the matrix [44-48]. Based on limited systematic studies on the effect of interphase thickness on mechanical properties, 50 to 200 nm is most commonly used for the PyC interphase in Generation III SiC fiber, CVI SiC matrix composites. Because of the rather limited irradiation stability of PyC, thicker interphases are anticipated to be disadvantageous in terms of the irradiation tolerance. However, experiments have not demonstrated any outstanding disadvantages of the composites with relatively thick PyC interphases [49].

It should also be noted that the vapor-deposited interphase thickness often varies substantially in different locations within the preform and even within a fiber bundle. The nominal interphase thickness is most commonly determined by the mass gain during the deposition process divided by estimated total fiber surface or by averaging the physical thickness values measured at multiple locations by backscattered electron microscopy.

2.1.3 Matrix

Similar to SiC fibers, the matrices in SiC/SiC composites are generally more radiation stable when they are of stoichiometric composition, of high crystallinity, and contain lesser amounts

of second phases, which tend to impose detrimental irradiation effects. Among the various techniques commonly used for matrix processing for SiC/SiC composites, chemical vapor infiltration (CVI) produces SiC matrices that best satisfy these criteria [5]. For this reason, CVI composites have been evaluated most extensively, often as the basic or reference materials for nuclear-grade SiC/SiC composites.

The CVI matrix densification process is essentially a CVD of SiC onto the fiber surfaces (then the open pore surfaces) in the composite preforms. Methyltrichlorosilane (MTS) and ethyltrichlorosilane (ETS) carried by hydrogen gas are commonly used as the precursor [5, 50-53]. Because the typical deposition temperatures of 1000 to 1200°C are significantly lower than the processing temperatures of other methods for SiC matrix densification, CVI is considered a low-temperature processing method for the fabrication of SiC matrix composites with the benefits of minimal process-induced damage to the fibers and reduced residual thermal stress. During the process of CVI, the fiber bundles in the preform first get solidified, forming an interconnected skeleton of “mini-composites,” or fiber bundles, with the internal and relatively thin surrounding matrices. This is followed by additional matrix deposition onto surfaces of the open pores that continues until a sufficient matrix density is achieved with most pores closed. Therefore, when the process is complete, the CVI composites inherently consist of fabric lay-up architectures made up of small elongated inter-fiber (intra-bundle) pores in mini-composite elements with more macroscopic inter-bundle pores whose size and shapes are determined primarily by the fiber architecture, and interlaminar pores (often connected with inter-bundle pores).

Figure 4 presents micrographs showing typical pores in 2D CVI SiC/SiC composites. Typical final porosity for 2D CVI SiC/SiC composites is 10 to 20 percent. The porosity values often exhibit mild correlations with the composite strength and thermal conductivity. However, among the pores of various types, the interlaminar pores impose particularly pronounced effects on key properties such as through-thickness thermal conductivity and interlaminar strength.

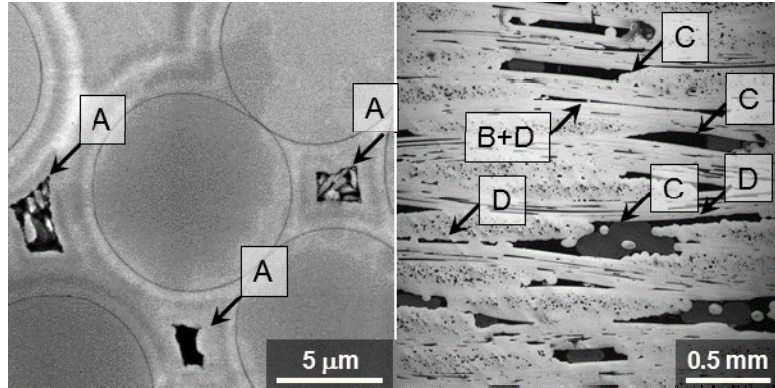


Figure 4. Micrographs representing different types of pores in typical 2D CVI SiC/SiC composites: A) intra-bundle micro-pores, B) inter-bundle mesh pores, C) inter-layer pores, and D) pores along inclined fiber segments. B, C, D are often connected with each other.

Besides CVI, the nano-infiltration and transient eutectic-phase (NITE) process, which utilizes sintering of nano-phase SiC powder assisted by external pressure and oxide additives to form the matrix, produces SiC-matrix composites that proved to be radiation resistant [54, 55]. Compared to CVI SiC/SiC, which is inherently very porous, NITE SiC/SiC composites offer nearly fully dense matrices, typically resulting in higher matrix cracking stress and higher thermal conductivity at the expense of chemical purity [56, 57]. The results from the RB-18J experiment on the NITE SiC/SiC composites are reported in a separate communication [58].

Effects of neutron irradiation on SiC/SiC composites made through other fabrication routes, such as polymer impregnation and pyrolysis (PIP) and melt-infiltration (MI), have not been extensively studied due to demonstrated and/or anticipated poor radiation stability of polymer-derived non-stoichiometric / nano-crystalline SiC and the reaction-bonded SiC/Si cermet [59, 60]. Formation of SiC matrices with decent irradiation performance through a polymer precursor route or a direct reaction is considered achievable, but may require substantial development effort [61-63].

2.1.4 Microstructures

Detailed microstructures of CVI SiC matrix composites may vary substantially, depending on the processing conditions. This also implies that the properties of the composites may be, to some extent, tailorable if the relationship between microstructure and the properties of interest can be adequately understood. For example, microstructures within the interphases and around their interfaces with fibers and/or matrices are known to influence the interfacial

debond and sliding properties [64]. Typical microstructures of nuclear-grade CVI SiC/SiC composites as observed by transmission electron microscopy are shown in Figure 5. Both the HNLS and SA3 fibers consist primarily of beta-phase SiC grains (which are often densely stacking faulted and significantly larger in size for the SA3 fiber) with the carbon pockets and pores in multi-grain junctions. Variations in microstructures and the corresponding properties for these near-stoichiometric SiC fibers of different grades are summarized by Bunsell and Piant [28].

Depending on the deposition condition, microstructure of the pyrolytic carbon interphases may range from well-oriented graphite to near-isotropic carbon. Whereas the oriented graphite interphase has been explored to achieve optimum interfacial debond behavior by Naslain et al. [40], near-isotropic carbon interphase is widely used in commercial CVI SiC/SiC due to ease of processing and preferred near-isotropic properties. The typical pyrolytic carbon interphase in the commercial materials, seen in Figure 5 (bottom center), is often considered as turbostratic graphite. Electron energy loss spectrometry analysis confirmed that the bonding in these interphases is predominantly sp^2 hybrid [65]. The specific mass of turbostratic carbon interphase in a typical CVI SiC/SiC composite was estimated to be ~ 1.9 based on combustion analysis [66], slightly higher than typical isotropic graphite but significantly lower than oriented graphite. Therefore, the typical CVD PyC interphase in a nuclear-grade SiC/SiC composite may be considered a fairly high-density turbostratic graphite. Note that these interphases are not necessarily near isotropic but are sometimes anisotropic with the basal planes slightly to moderately aligned parallel with the fiber surface. The CVI SiC matrices are essentially CVD SiC deposited onto the fiber and pore surfaces; thus, they exhibit typical columnar structure along the growth direction, as seen in Figure 5 (bottom right). The crystallographic orientation is commonly along one of the $\{111\}$ planes, which typically involves very high-density stacking faults, moderately aligned perpendicular to the columnar axis.

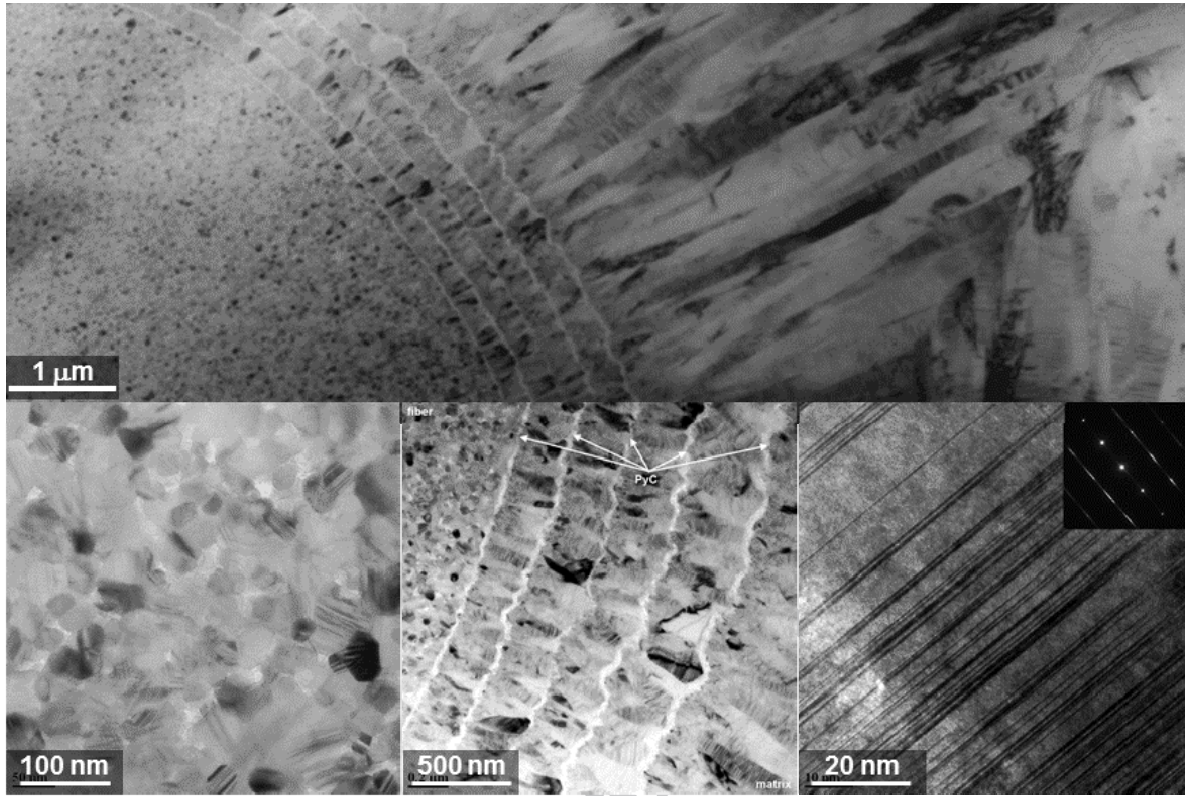


Figure 5. Transmission electron microscopy images of Hi-Nicalon Type S near-stoichiometric SiC fiber-reinforced, purocarbon/SiC multilayer interphase, and chemically vapor-infiltrated SiC-matrix composite (top). Higher magnification micrographs are given in the bottom for the fiber interior (left), interphase (center), and matrix (right).

noza

2.2 Composite Materials Used

The composite materials studied are listed in Table 2. The material designator in the table indicates the combination of fiber grade, HNLS or SA3, and the interphase, PyC for pyrocarbon (PyC150 denotes pyrocarbon interphase that is nominally 150 nm thick) or ML for pyrocarbon/SiC multilayer, followed by an additional suffix that distinguishes different fabrication batches. The ML interphase consists of five repeating layers of nominally 20-nm-thick pyrocarbon separated by pyrolytic (CVD) SiC nominally 100 nm thick. More details of this interphase are found elsewhere [67]. As discussed previously, this ML interphase acts as single 20-nm-thick PyC interphase during fast fracture under typical mechanical testing while providing additional protection to fibers during slow failure in oxidative environments. The matrices for all composites are high-purity CVI SiC. The composite fabrication was performed by Hyper-Therm High-Temperature Composites (Huntington Beach, CA), with the exception of HNL/PyC150-B, which was provided by GE Energy (Newark, DE).

Table 2. Detailed information of composite materials evaluated in this work. Note that matrices in all materials are high-purity, stoichiometric, polycrystalline beta-phase SiC deposited through chemical vapor infiltration process.

| Material Designator | Fiber | Architecture | Interphase | Apparent Density [g/cm ³] | Porosity | Fiber Volume Fraction | Ref. |
|---------------------|--------------------------------|---|---------------------------|---------------------------------------|----------|-----------------------|------------------|
| SA3/PyC150-A | Tyranno SA3 ¹ | PW ⁶ , 17x17 tpi ⁷ 0°/90° | PyC ⁹ , 150 nm | 2.58 | 0.18 | 0.38 | Katoh, 2011[68] |
| SA3/PyC50-A | Tyranno SA3 ¹ | PW, 17x17 tpi 0°/90° | PyC, 50 nm | 2.62 | 0.17 | 0.38 | " |
| SA3T/PyC150-A | Tyranno SA3T ² | PW, 17x17 tpi 0°/90° | PyC, 150 nm | 2.50 | 0.20 | 0.37 | " |
| HNLS/PyC150-A | Hi-Nicalon Type S ³ | PW, 25x25 tpi 0°/90° | PyC, 150 nm | 2.40 | 0.23 | 0.46 | " |
| HNLS/PyC50-A | Hi-Nicalon Type S ³ | PW, 25x25 tpi 0°/90° | PyC, 50 nm | 2.31 | 0.26 | 0.46 | " |
| HNLS/ML-A | Hi-Nicalon Type S ⁴ | 5H-SW ⁸ , 16x16 tpi, 0°/90° | Multilayer ¹⁰ | 2.47 | 0.24 | 0.37 | " |
| HNLS/PyC150-B | Hi-Nicalon Type S ⁴ | 5H-SW, 16x16 tpi, 0°/90° | PyC, 150 nm | 2.71 | 0.14 | 0.40 | - |
| SA3/PyC150-C | Tyranno SA3 ¹ | PW, 17x17 tpi 0°/90° | PyC, 150 nm | 2.53 | 0.18 | 0.40 | Nozawa, 2005[69] |
| HNLS/PyC150-C | Hi-Nicalon Type S ⁴ | 5H-SW, 16x16 tpi, 0°/90° | PyC, 150 nm | 2.52 | 0.19 | 0.44 | " |
| HNLS/PyC150-D | Hi-Nicalon Type S ⁴ | 5H-SW, 16x16 tpi, 0°/90° | PyC, 150 nm | 2.65 | 0.15 | ~0.4 | Nozawa, 2007[70] |
| SA3/PyC150-D | Tyranno SA3 ¹ | PW, 17x17 tpi 0°/90° | PyC, 150 nm | 2.62 | 0.16 | ~0.4 | - |
| SA3/PyC150-E | Tyranno SA3 ¹ | PW, 17x17 tpi 0°/90° | PyC, 150 nm | n/a ¹¹ | n/a | n/a | Nozawa, 2012[71] |
| SA3-P120/PyC150 | SA3 / P-120S ⁵ | Orthogonal 3D | PyC, 150 nm | 2.27 | n/a | n/a | Katoh, 2006[72] |
| SA3/ML-F | Tyranno SA3 ¹ | 8H-SW, 22x22 tpi, 0°/90° | Multilayer ¹⁰ | 2.65 | 0.12 | 0.33 | Katoh, 2010[73] |
| HNLS/ML-F | Hi-Nicalon Type S ⁴ | 8H-SW, 20x20 tpi, 0°/90° | Multilayer ¹⁰ | 2.74 | 0.11 | 0.31 | " |

1: 7.5 micron, 1600 filament/yarn, SA3-S1116PX, 2: 10 micron-diameter thick fiber, 800 filament/yarn, SA3-S1F08PX, 3: 900 denier (250 filament/yarn), Lot#383213, 4: 1800 denier (500 filament/yarn), lot# unknown, 5: Hybrid 3D fabric of Tyranno SA3 in x/y directions and pitch-based P120S graphite fiber in z direction, 6: plain-weave, 7: thread per inch, 8: 5-harness satin-weave, 9: pyrocarbon, 10: 5 x (PyC 20 nm + SiC 100 nm), 11: not available.

It is worth noting that non-standard fabrics or fibers were used for some of the composites. For HNLS/PyC50-A and HNLS/PyC150-A, 24 x 24 thread-per-inch (TPI) plain-weave fabrics with 250 filament yarns were used instead of the standard 16 x 16 TPI satin-weave fabric with 500 filament yarns. These fine weave fabrics were used with an expectation that the small specimens used for irradiation studies would better represent the bulk properties. However, as seen in Table 2, the higher fiber loading and the smaller dimensions of open channels in the fabric preform resulted in the unusually large final porosity, somewhat compromising the composite properties, as discussed later.

The SA3T/PyC150-A composite used plain-weave fabrics of 800 filament yarn thick (nominally 10-micron diameter) SA3 fibers instead of the common 1600 filament yarn 7.5-micron-diameter SA3 fibers. The SA3-P120/PyC150 composite was fabricated using hybrid plain-weave fabrics into which alternating threads of SA3 and pitch-based Cytec-Thornel P120 graphite fibers were woven. Detailed description of this hybrid fabric is found elsewhere [72].

The fiber volume fraction (V_f) in Table 2 was determined by a geometrical approach in the following manner [74]:

$$V_f = \pi r_f^2 N_f N_t N_p , \quad (1)$$

where r_f denotes fiber radius, N_f the number of filaments in a tow, N_t the total (x and y) thread counts for the fabric, and N_p the number of fabric layers in a unit thickness. Using the apparent density for composite (ρ), the composite porosity value (V_p) is derived by

$$V_p = 1 - \left(V_f + \frac{\rho_c - m_f N_p}{\rho_m} + \frac{\rho_m - \rho_i}{\rho_m} \cdot \frac{2m_f N_p t_i}{r_f \rho_f} \right), \quad (2)$$

where m_f is the fabric mass, $\rho_{h,i,f}$ denote specific masses of matrix, interphase, and fiber, respectively, and t_i is the interphase thickness.

Figure 6 presents low-magnification SEM images of polished cross-sections for most of the composite materials used in this work, showing the mesoscopic structures including the various type pores typical of the CVI SiC matrix composites of 2-D fabric layup architectures. The observed mesostructures appear generally consistent with the porosity and the fiber volume fraction values in Table 2. For example, relatively low matrix density with the extensive inter-laminar porosity can be seen for the HNLS/PyC50-A and HNLS/PyC150-A composites. The SA3-P120 hybrid fabric composite (not shown in Figure 6) underwent extensive matrix cracking because of the major mismatch in thermal expansion between the SiC matrix and the P120 graphite fibers.

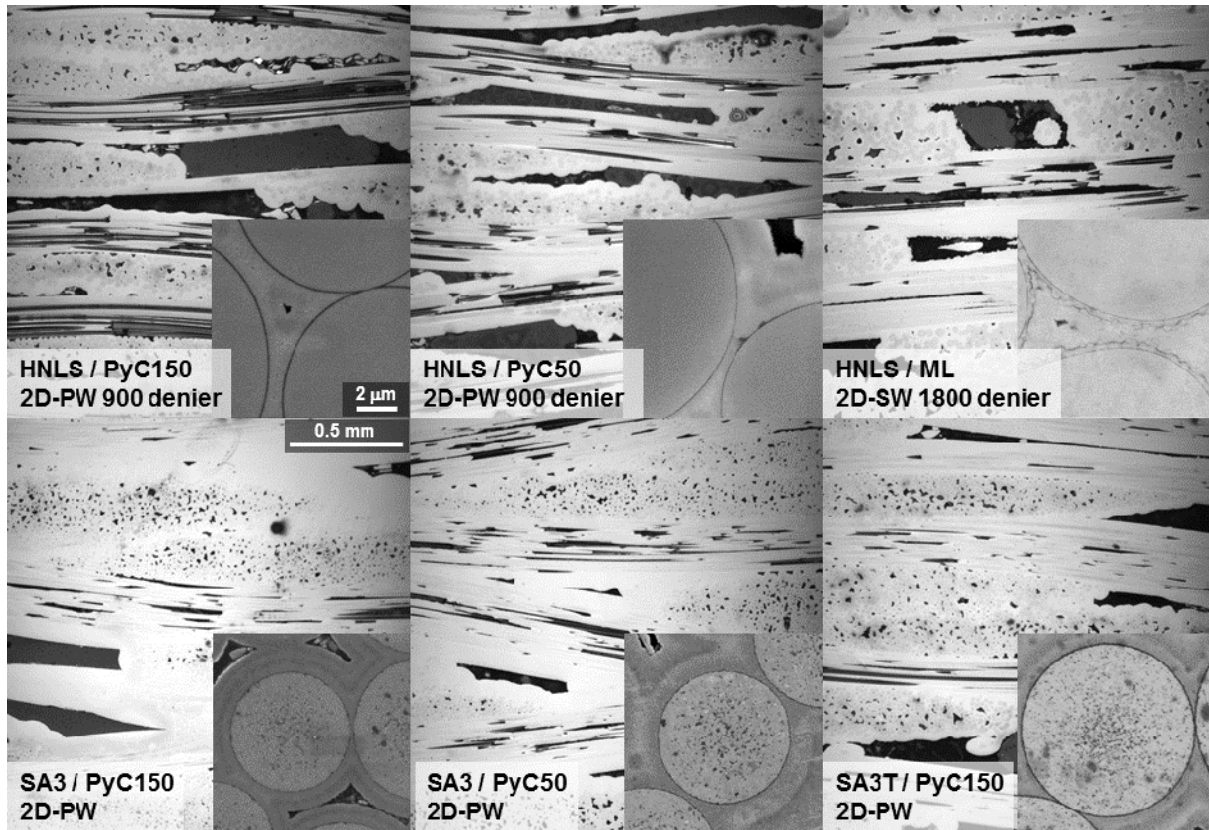


Figure 6. Low-magnification scanning electron micrographs showing cross-sectional meso-structures representing materials examined.

3 Experimental Method

3.1 Methods of Properties Evaluations

All property information presented in this paper is original data generated at Oak Ridge National Laboratory (ORNL), unless references indicate otherwise, through the methods briefly described below. Post-neutron irradiation examination was performed in the Low Activation Materials Development and Analysis (LAMDA) Facility at ORNL.

Thermal and physical properties

The coefficient of linear thermal expansion (CTE) was measured per ASTM Standard E228-06 using a push-rod dilatometer Netzsch DIL 402 CD at a constant heating rate equal to or slower than 5 K/min. Thermal diffusivity was measured by the flash method according to ASTM E1461-07. The instruments used were a Netzsch LFA 447 and 457 and an Anter Flashline 3000. Thermal conductivity was calculated using the measured thermal diffusivity, the measured specific gravity for the individual specimen, and the standard specific heat values found in Reference [17] for SiC. The influence of the presence of graphitic interphase on the specific heat of the composite was estimated to be less than 1 percent and thus was neglected.

The dynamic Young's modulus was determined at room temperature based on the fundamental resonance measurement by the method of impulse excitation and vibration per ASTM C1259-08 using a JW Lemmens GrindoSonic Instrument.

Swelling

Swelling, or volumetric expansion induced by neutron irradiation, was determined based on the envelope dimensions for rectangular test specimens measured before and after irradiation using a caliper (for length) and a micrometer (for width and thickness). The standard specimen dimensions before irradiation were 40 mm x 4 mm x 2 mm. Considering the typical equipment calibration error and the measurement error, uncertainty in swelling determination is estimated to be less than 0.2 percent.

In-plane mechanical properties

The in-plane tensile properties were determined following the general guidelines in ASTM C1275-00. However, an intermittent unloading-reloading scheme was employed in order to extract information on the residual thermal stress, extent of the matrix cracking, and the fiber-

matrix interfacial sliding resistance as a function of the peak load. Previous work confirmed the lack of effects of this loading scheme on the measured tensile properties for similar composite materials as compared with a monotonic loading scheme. Strain was monitored by a pair of strain gauges attached to opposite faces within the gauge section. The average of the readings from the two strain gauges was used as the strain value. Tests with fractional bending, also determined by readings from the two strain gauges, reaching 10 percent within the proportional limit loading were considered invalid.

Straight beam specimens measuring 40 mm x 4 mm x 2 mm were used for all tests, with the exception of the HNLS/PyC50-A and HNLS/PyC150-A tests, which utilized specimens that were 1.5 mm thick but otherwise identical. The gauge section length was 12 mm. A MTS pneumatic gripping system was used and aluminum tabs were adhered to both sides of the grip sections of the specimens to prevent gripping-induced compressive failure.

Tangent modulus of the composites was determined by the least-squares method for the initial loading over a range of 20–40 MPa. The proportional limit stress (PLS) was defined as the stress at the intersection with the 95 percent tangent modulus slope.

Interface mechanical properties

Two important micro-mechanical properties of interest for the fiber-matrix interface in ceramic matrix composites are the sliding stress and the shear debond stress. The sliding stress is often determined or estimated based on the single-fiber push-out test [75], hysteresis analysis of the intermittent unloading-reloading during the in-plane tensile test [76, 77], or fiber pull-out length observation of the tensile fracture surface [78]. The shear debond stress can be estimated from the single-fiber push-out test. In the present work, the single-fiber push-out test was chosen as the method of evaluating the interfacial mechanical properties and the test was conducted using an MTS Nano-Indenter system. More details of the testing and analytical procedures are discussed in Section 4.3.4.

Trans-plane mechanical properties

The inter-laminar shear strength (ILSS) of the 2D laminate composite materials was determined by compression testing of double-notched shear (DNS) specimens per ASTM C1292-00. Specimen dimensions of 20 mm x 4 mm x 2 mm and a notch separation of 6 mm were employed. These specimen dimensions, smaller than the recommendation in the ASTM test standard, have been shown to generate reasonable ILSS values for similar materials, though such reduced size specimens may suffer a minor size effect [79-81].

The trans-thickness tensile strength (TTS) was determined by diametral compression testing at room temperature. In this test, the diametral compressive load, applied to a small-diameter

disc (or truncated disc) specimen, is converted to tensile load in the perpendicular orientation, leading to the failure in trans-thickness tension. Details of the test procedure are given in [82, 83].

Damage tolerance

Damage tolerance was evaluated using miniature single-edged notched beam (SENB) specimens. Details of the test procedure and the effects of the test specimen size have been discussed elsewhere [84]. The SENB tests were conducted at room temperature using an electromechanical testing machine. Test specimens were loaded using a three-point flexural fixture with a support span of 16 mm under a constant crosshead displacement rate of 0.05 mm/min. The load-point displacement was measured with a clip-on crack opening gauge. The unloading-reloading sequences were applied to evaluate the damage accumulation behavior during testing. Crack length at each loading-unloading cycle was evaluated by optical microscopy of replica films.

3.2 Neutron Irradiation

Neutron irradiation was conducted in the High Flux Isotope Reactor (HFIR) at ORNL as a part of the RB-18J high-temperature neutron irradiation campaign. The 18J capsule included subcapsules, each of which is actively temperature controlled through the gas composition adjustment. The fast neutron fluences were $\sim 5.9 \times 10^{25} \text{ n/m}^2$ ($E > 0.1 \text{ MeV}$) for the nominally 800°C temperature zone and $\sim 5.8 \times 10^{25} \text{ n/m}^2$ for the nominally 1300°C zone. An equivalence of one displacement per atom (dpa) = $1 \times 10^{25} \text{ n/m}^2$ ($E > 0.1 \text{ MeV}$) is assumed in the following discussion.

The actual irradiation temperatures for specimens were determined by electrical resistivity measurements with selected CVD SiC specimens at room temperature after isochronal annealing. These specimens consistently indicated the onset of resistivity annealing at $\sim 830^\circ\text{C}$ and $\sim 1270^\circ\text{C}$ for the nominally 800°C and 1300°C temperature zones. The typical error in determination of actual irradiation temperature by this method is estimated to be $\sim 25^\circ\text{C}$ [85].

4 Properties and Effects of Neutron Irradiation

4.1 General Effects of Irradiation and Dimensional Stability

4.1.1 General Effects of Irradiation

In this section, data for various thermal, physical, and mechanical properties in both unirradiated and neutron-irradiated conditions are presented and discussed. Before elaborating on the individual properties and the irradiation effects, the effects of irradiation on SiC/SiC composites are briefly reviewed in a generic sense. A comprehensive review of the properties for conventional (non-nuclear-grade) SiC fiber and CVI SiC matrix composites in an unirradiated condition was previously compiled by Lara-Curzio [86].

Obviously, the properties of a composite material are determined by the properties of its constituents, namely, matrix, fiber, and interface, and the constitutive laws that are in many cases for the specific reinforcement architecture. The “interface” may involve the interphase as a substance and the interfaces between the interphase and the neighboring matrix or fiber. Constitutive models for various composite properties have been studied and developed as mentioned in the discussion below. However, these models have often been established to an insufficient extent to predict properties of the composites due to the complex interplays among constituents in the 2D architecture.

As compared to SiC in other forms, the effects of neutron irradiation and the underlying physical processes are relatively well understood for high-purity beta-phase SiC [17], which reasonably represents the matrix material for CVI SiC matrix composites. Briefly, neutron bombardment produces Frenkel defects in both C and Si sublattices, antisite defects of both types, and clusters of these defects in the face-centered cubic sublattices overlapping in beta-phase SiC. In the temperature range for point defect swelling (or “transient swelling,” approximately 150°C to 1000°C) where vacancies of both types have no or very limited mobility, the matrix defects build up until pseudo-equilibrium is reached. This defect build-up causes swelling corresponding with the total excess volumes from various defects, significant thermal conductivity decrease by added phonon-scattering centers, and a slight decrease in Young’s modulus due to an increase in mean interatomic distance. All of these properties saturate at relatively low fluences, typically on the order of ~1 dpa. At higher temperatures exceeding ~1400°C where both types of vacancies are anticipated to be mobile, progressive changes in properties occur including void swelling caused by unstable growth of vacancy clusters.

Between $\sim 1000^{\circ}\text{C}$ and $\sim 1400^{\circ}\text{C}$ is considered the transitional temperature regime where the progressive microstructural evolutions and the resultant fluence-dependent property changes proceed steadily but only slowly. The effects of neutron irradiation on properties of CVD SiC are summarized by Snead et al., in Ref. [17].

Near-stoichiometric beta-phase SiC fibers are considered to behave in a manner similar to high-purity CVD SiC. In fact, lack of significant differential swelling (from CVI SiC matrices) or any other substantial changes in properties under irradiation has been previously reported [36, 73, 87], in contrast to that of conventional non-stoichiometric SiC-based fibers which underwent substantial volume contraction by exposure to neutrons [26]. However, the potential influences of specific features of those fibers including the chemical impurities or additive elements, the presence of carbon pockets, and the inhomogeneity in grain microstructures along radial locations on the radiation stability at extended fluence levels all remain to be clarified.

Similarly, irradiation response of the PyC interphase is not adequately understood. Under irradiation, the PyC interphase as highly imperfect graphite is anticipated to behave like other carbon materials such as poorly graphitized graphite and glassy carbon. Nuclear-grade graphite materials undergo early contraction accompanied by an increase in strength, elastic modulus, and thermal and electrical conductivity. This is followed by swelling and a reversal of all other property changes in the opposite direction, which eventually leads to a loss of mechanical integrity [19, 20]. The very limited information on effects of irradiation on glassy carbon implies similar behavior [22]. However, it is unclear how closely the irradiated PyC interphase follows the path and fate of irradiated nuclear graphite and how the thin-layer interphase that is mechanically constrained by very high modulus SiC on both faces behaves as compared to the unconstrained bulk material.

In addition to the general effects of irradiation discussed above, significant effects of nuclear transmutations are anticipated for all properties when these materials are irradiated with very high-energy neutrons such as those anticipated in deuterium-tritium fusion reactors and the nuclear spallation targets. The nuclear transmutation effect is particularly anticipated to be an important life-limiting factor, in addition to the environmentally assisted degradation discussed in Section 4.3.7, because of the time-dependent accumulation of various transmutation products. Discussion on the transmutation phenomena in fusion spectrum and the potential consequences are found in Ref.[88]. The scope of present work does not include those transmutation effects.

4.1.2 Transient Swelling

As briefly described above, irradiated crystalline SiC undergoes swelling that saturates at low fluence levels in a temperature range below ~1000°C. Beyond ~1000°C up to ~1400°C, swelling is considered to be a mixture of the transition point defect swelling (that saturates) and the slowly developing void swelling. Swelling measured in the present work is summarized in Table 3 along with the data reported in literature [67, 89]. These data are also plotted in Figure 7 for the purpose of comparison with the extensive published data for high-purity CVD SiC [15, 27, 90-93]. The swelling trends for the CVI composites and the CVD SiC agree well, although the composite swelling in general appears slightly less than the monolithic CVD. However, considering the unfortunately large errors associated with the composite swelling measurement in the present and previous works, this difference may be considered insignificant. There is no significant difference noted between the HNLS and the SA3 fiber composites. Hegeman et al. [94] reports almost identical longitudinal linear swellings for CVD SiC and SA-Tyrannohex™, which is a uni-directional bonded SA3 fiber composite, irradiated side by side in the High Flux Reactor (HFR, Petten) at 600°C and 900°C to 1.1 to 2.0 dpa. Katoh [95] reports swelling for SA-Tyrannohex close to typical swelling for CVD SiC after irradiation in HFIR at 320°C to ~6 dpa. These two reports imply no significant difference in swelling behavior between the high-purity CVD SiC and the SA3 fiber. Collectively considering these results, there is no convincing reason to believe that the nuclear-grade SiC/SiC composites undergo swelling to an extent significantly different from that of CVD SiC.

Table 3. Irradiation-induced swelling for CVI SiC matrix composites.

| Material | Irradiation Condition | Swelling (%) | Ref. |
|-----------------|-----------------------|--------------|-------------------|
| SA3/PyC150-A | 830°C, 5.9 dpa | 0.50 (0.07) | - |
| | 1270°C, 5.8 dpa | 0.58 (0.30) | - |
| SA3/PyC50-A | 830°C, 5.9 dpa | 0.55 (0.14) | - |
| | 1270°C, 5.8 dpa | 0.56 (0.23) | - |
| SA3T/PyC150-A | 830°C, 5.9 dpa | 0.61 (0.15) | - |
| HNLS/PyC150-A | 830°C, 5.9 dpa | 0.52 (0.16) | - |
| | 1270°C, 5.8 dpa | 0.21 (0.08) | - |
| HNLS/PyC50-A | 830°C, 5.9 dpa | 0.28 (0.09) | - |
| HNLS/ML-A | 830°C, 5.9 dpa | 0.39 (0.20) | - |
| | 1270°C, 5.8 dpa | 0.49 (0.31) | - |
| HNLS/PyC150-B | 300°C, 1.2 - 3.4 dpa | 1.59 (0.49) | Newsome, 2007[67] |
| | 800°C, 1.6 - 2.4 dpa | 0.81 (0.13) | Newsome, 2007[67] |
| SA3-P120/PyC150 | 830°C, 5.9 dpa | 0.67 (0.28) | - |
| | 1270°C, 5.8 dpa | 0.45 (0.14) | - |
| | 830°C, 5.9 dpa | 0.56 (0.16) | - |

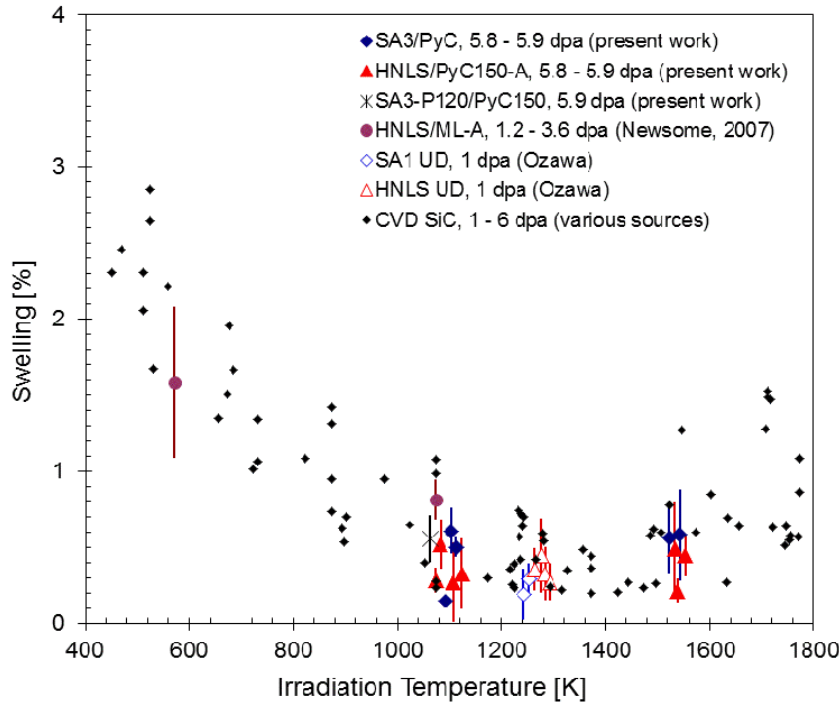


Figure 7. Volume swelling of CVI SiC matrix composites by neutron irradiation as a function of irradiation temperature. Error bars indicate \pm one standard deviation. Additional composite swelling data were taken from refs. [67, 89]. Data for high-purity CVD SiC in a monolithic form from various references are shown together as dot symbols [15, 27, 90-93].

Transient swelling behavior of CVD SiC has been given by the following equation by Katoh et al. [Katoh, 2013 #1088]:

$$\dot{S} = k_s \gamma^{-1/3} \exp\left(-\frac{\gamma}{\gamma_{sc}}\right), \quad (3)$$

where \dot{S} denotes swelling rate, k_s the rate constant for swelling, γ the fast fluence, and γ_{sc} the characteristic fluence for swelling saturation by the negative feedback mechanism. The $-1/3$ exponent for fluence dependence comes of assumptions that the isolated self-interstitial atoms (SIA's) migrate to annihilate with immobile vacancies through mutual recombination or to form/grow immobile SIA clusters in planar configurations [96]. The exponential function represents swelling saturation by unspecified negative feedback mechanisms under an assumption that the sole negative term in a rate equation for the total SIA cluster volume is proportional to the total SIA cluster volume itself. Such mechanisms may include the cascade resolution of the SIA clusters and the physical overlapping of growing SIA clusters with neighboring vacancies. The model neglects likely contributions from antisite defects to swelling. Using the currently available experimental data for neutron irradiation swelling of high-purity

CVD SiC in the temperature range 200–800°C [17], the following polynomial fits may be suggested for the rate constant and the characteristic saturation fluence as functions of irradiation temperature in K.

$$k_s(T) = 0.10612 - 1.5904 \times 10^{-4} T + 6.0631 \times 10^{-8} T^2$$

$$\chi_c (\text{dpa}) = 0.51801 - 2.7651 \times 10^{-3} T + 9.4807 \times 10^{-6} T^2 - 1.3095 \times 10^{-8} T^3 + 6.7221 \times 10^{-12} T^4$$

$$(473\text{K} < T < 1073\text{K}) \quad (4)$$

Result of calculated fluence-dependent build-up of swelling is given in Figure 8 for a few selected temperatures. It is noted that very high accuracy may not be expected for these fitting functions due to the limited quality and quantity of swelling data previously published for high-purity CVD SiC.

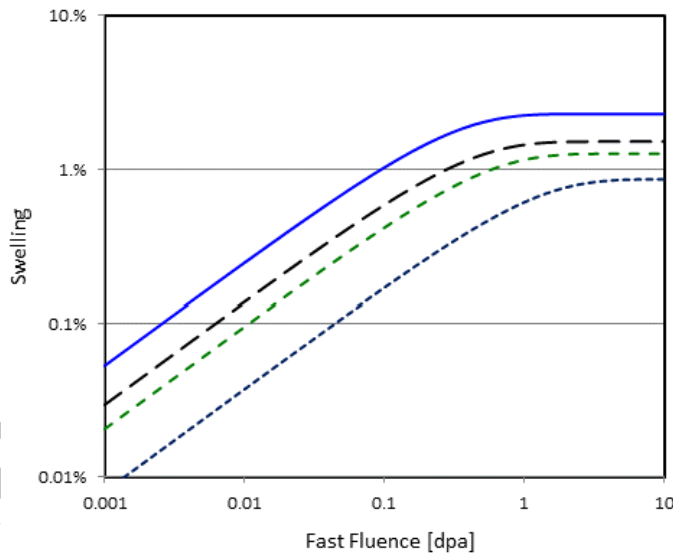


Figure 8. Dose-dependent evolutions of swelling given by Equations 3 and 4 for CVD SiC and nuclear-grade CVI SiC/SiC.

4.2 Thermal and Physical Properties

4.2.1 Thermal Expansion

4.2.1.1 Non-irradiated property

The CTE values measured for SA3/PyC150-A, HNLS/PyC150-A, and HNLS/PyC50-A are plotted in Figure 9 as the temperature-dependent instantaneous values. Samples of the Rohm & Haas high-purity CVD SiC were also measured side by side with one of the composites in a parallel dilatometry unit, and the result is plotted for comparison. The averages of two samples for each material were plotted; however, the differences between the replicate samples appeared negligible. As seen in Figure 9, all four materials exhibited exactly the same linear thermal expansion behavior with no detectable differences between the CVI composites and high-purity CVD SiC. A polynomial approximation found in the literature for 3C-SiC thermal expansion [17] is also plotted showing reasonable agreement with the experimental data for the temperature range below ~750K. This is obviously because the polynominal fit in Ref. [17] is appropriate only up to ~750K. The present data can be fit by the following polynomial expression:

$$\alpha(10^{-6}/K) = -0.7765 + 1.4350 \times 10^{-2}T - 1.2209 \times 10^{-5}T^2 + 3.8289 \times 10^{-9}T^3 \quad (5)$$

for $293K < T < 1273K$.

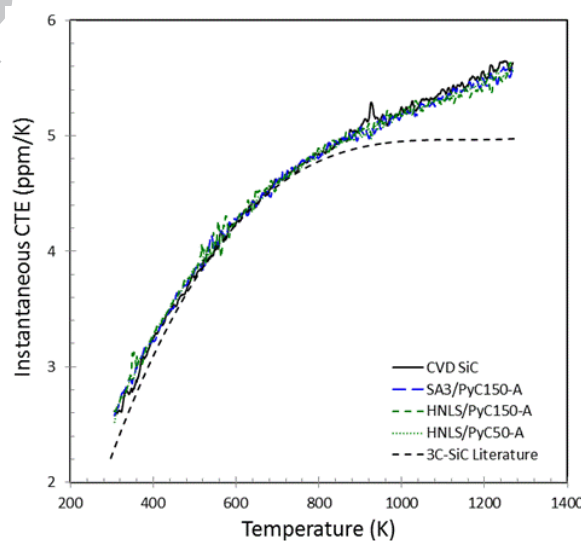


Figure 9. Thermal expansion of 2D SiC/SiC composites and comparison with that for high-purity CVD SiC. Measurement orientation for 2D SiC/SiC samples was in-plane along one of the fiber axes. 3C-SiC literature data was taken from Ref. [17].

As seen in Table 2, the typical fiber volume fraction and the typical porosity for the 2D composites tested are ~40% and ~20%, respectively. This means that the fibers and the matrix should be contributing to the composite CTE to about the same extent. Assuming that the fiber CTE's do not significantly differ between the axial and radial orientations based on the microstructure shown in Figure 5, and because the CTE for the CVI matrix has to be very similar to that for CVD SiC, the present result indicates CTE values for the matrix SiC and the fibers are very close to each other for the composites with both fiber types. The CTE for SA3 fiber is reported by manufacturer to be 4.5 ppm/K for RT-1000°C, agreeing with the present data very well. The manufacturer-claimed value of CTE for HNLS fiber is 5.1 ppm/K for RT-500°C, more than 20 percent higher than both the literature value for pure SiC and data obtained in the present work for composites containing this fiber. However, based on the present result, it is concluded that the CTE for the HNLS fibers used in this work is closer to that of pure SiC than the manufacturer-claimed values.

4.2.1.2 Effect of irradiation

The instantaneous CTE values measured for irradiated composite samples in the present work are plotted in Figure 9 as a function of temperature. The effects of irradiation appear minor for both irradiation temperatures and for the composites with both fiber types. The current result confirms the little to minor effect of irradiation on CTE for the near-stoichiometric SiC composite materials. A closer look at Figure 10 suggests the slight, yet constant, CTE decrease over the entire temperature range after irradiation at 830°C for the composites with both fiber types, possibly indicating the effect of lattice swelling on thermal expansion. In contrast, the SA3 composite irradiated at 1270°C did not exhibit a hint of CTE modification. The slight increase in CTE for the HNLS composite found after irradiation at 1270°C cannot be explained but is considered insignificant.

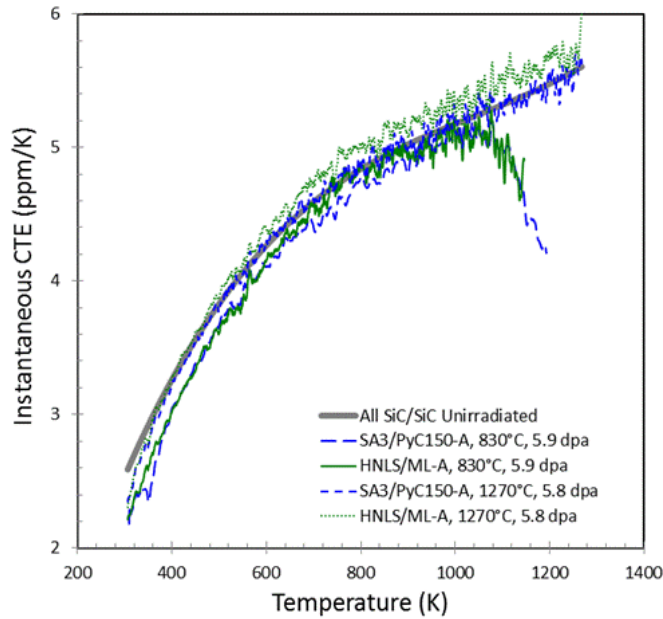


Figure 10. Effect of neutron irradiation on linear thermal expansion of 2D SiC/SiC composites. Orientation of composite samples was in-plane along one of the fiber axes.

Figure 10 also shows the onset of recovery of the transient swelling when the temperature exceeds the irradiation temperature. The recovery behavior for these two composite samples indicates that the actual irradiation temperature of $\sim 810 \pm 20^\circ\text{C}$ agrees reasonably well with the irradiation temperature determined, as described in Section **Error! Reference source not found.** The current result demonstrates that the CVI SiC-matrix composites with the Generation III SiC fibers may be used as the irradiation temperature monitor as well as the high-purity CVD SiC. Moreover, it proves that dilatometry-based SiC thermometry is useful for irradiation temperatures well above 800°C , where the previous work only reports results up to 760°C [97].

4.2.2 Thermal Conductivity

4.2.2.1 Non-irradiated property

Thermal conductivity for nuclear-grade 2D CVI SiC/SiC composites measured at room temperature in the present work is summarized in Table 4, along with the data found in open literature [69, 73]. The room temperature thermal conductivity values in the through-thickness direction for these materials vary widely in the range of 8.5–18.1 W/m·K for the HNLS composites and 15.2–23.7 W/m·K for the SA3 composites. These numbers are substantially higher than the typical through-thickness thermal conductivity for the non-stoichiometric SiC

fiber composites (4–8 W/m-K) [86], owing to the increased thermal conductivity of HNLS (18.4 W/m-K) and SA3 (65 W/m-K) as compared to ceramic-grade Nicalon (~3 W/m-K) and Hi-Nicalon (7.8 W/m-K). The consistent difference between the HNLS and SA3 composites reflects the different thermal conductivity between the two fiber grades.

Table 4. Room-temperature thermal conductivity for various 2D SiC/SiC composites in unirradiated condition.

| Material | Orientation | RT Thermal Conductivity (W/m-K) | Ref. |
|-----------------|------------------|---------------------------------|------------------|
| SA3/PyC150-A | T/T ¹ | 21.2 (0.4) ³ | - |
| SA3/PyC50-A | T/T | 23.7 (0.4) | - |
| HNLS/ML-A | T/T | 10.6 (0.2) | - |
| SA3/PyC150-C | T/T | 18.9 (0.3) | Nozawa, 2005[69] |
| HNLS/PyC150-C | T/T | 18.1 (0.3) | Nozawa, 2005[69] |
| HNLS/PyC150-D | T/T | 14.1 (0.3) | - |
| SA3/PyC150-D | T/T | 15.2 (0.4) | - |
| SA3-P120/PyC150 | T/T | 53.0 (13.5) | - |
| SA3/ML-F | T/T | 22.9 (2.2) | Katoh, 2010[73] |
| HNLS/ML-F | T/T | 8.5 (2.0) | Katoh, 2010[73] |
| SA3/PyC150-C | I/P ² | 47.8 (1.3) | Nozawa, 2005[69] |
| HNLS/PyC150-C | I/P | 34.7 (1.3) | Nozawa, 2005[69] |
| SA3-P120/PyC150 | I/P | 32.6 (0.5) | Nozawa, 2005[69] |

1: through-thickness; 2: in-plane; 3: numbers in parentheses are one standard deviations

It is noted that the variations in through-thickness thermal conductivity for similar 2D CVI SiC-matrix composites with the identical fiber grade appear substantial, reaching $\pm 40\%$, as compared with the typical specimen-to-specimen variations from plates of the identical lot material, which do not often exceed $\sim 10\%$ when measured by flash diffusivity method using 6- to 10-mm-diameter specimens. Materials of particularly high porosity should exhibit notably low thermal conductivity for an obvious reason. However, data listed in Table 4 do not present a meaningful correlation with porosity of the composites. The likely reason for this is that the through-thickness thermal conductivity for the 2D architecture composites is not determined by the total porosity but by primarily by interlaminar porosity. The effectiveness of pores of various types discussed in Section 2.1.3 on the composite thermal conductivity has been well demonstrated using a simple constitutive model such as the serial-parallel approach [72, 98]. One such model explains the experimental through-thickness and in-plane thermal conductivity data compared with the bulk thermal conductivity of ~ 70 W/m-K for the CVI SiC matrix material and 2 to 5 W/m-K for the PyC interphase [72]. The in-plane thermal conductivity, which is less important for most applications, is governed primarily by the effective axial fiber fraction along the direction of heat transport and the matrix surrounding the axial fiber bundles [72].

The temperature dependence of trans-thickness thermal conductivity for selected materials is shown in Figure 11. Thermal conductivity of SiC composites often exhibits a peak or a bump below 373K because of the steep increase in heat capacity with temperature up to about that temperature and the increased Umklapp contribution with increasing temperature. The temperature dependence is well depicted by plotting the reciprocal thermal diffusivity against temperature in Figure 12 where an approximately linear relationship is observed for all materials examined. It is noted that the temperature coefficients for the reciprocal thermal diffusivity fall in a range $0.02 \pm 0.005 \text{ s/cm}^2\text{-K}$ for most composites, enabling prediction of elevated temperature thermal conductivity based on the room-temperature values with reasonably small uncertainty.

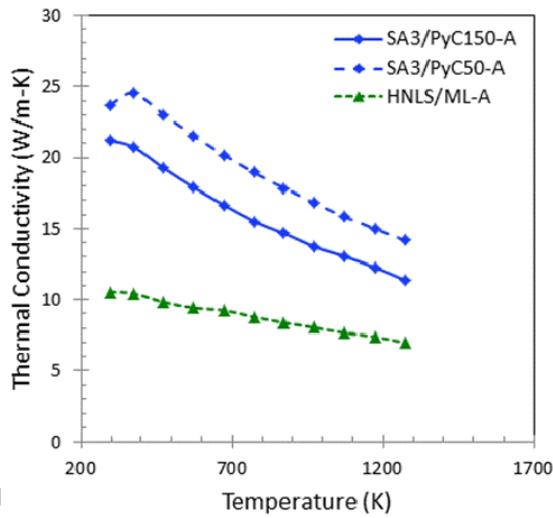


Figure 11. Temperature dependence of thermal conductivity for 2D SiC/SiC composites in unirradiated condition.

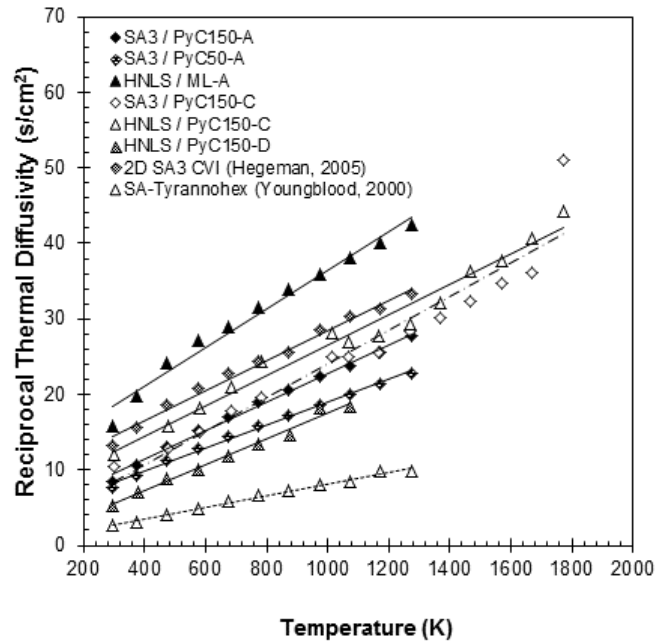


Figure 12. Reciprocal thermal diffusivity for 2D SiC/SiC composites plotted against temperature. Some of data were derived from literature [94, 99].

4.2.2.2 Effect of irradiation

The post-irradiation thermal conductivity for the nuclear-grade composites measured at room temperature is compiled in Table 5 [73, 100]. Significant decrease is obvious regardless of irradiation condition. The change in thermal conductivity during irradiation saturates at relatively low fluence levels, typically before a few dpa is reached, depending on irradiation temperature in the same way that the transient swelling saturates. No departure from the saturation at higher fluences has thus far been confirmed up to >70 dpa at 800°C.

Table 5. Through-thickness thermal conductivity at room temperature for 2D SiC/SiC composites in irradiated conditions.

| Material | Irradiation Condition | RT Thermal Conductivity (W/m-K) | RT Radiation Defect Thermal Resistivity (W/m-K) ⁻¹ | Ref. |
|--------------|-----------------------|---------------------------------|---|-----------------|
| SA3/PyC150-A | 830°C, 5.9 dpa | 6.2 | 0.11 | - |
| | 1270°C, 5.8 dpa | 10.5 | 0.048 | - |
| SA3/PyC50-A | 830°C, 5.9 dpa | 8.1 | 0.081 | - |
| | 1270°C, 5.8 dpa | 11.7 | 0.043 | - |
| HNLS/ML-A | 830°C, 5.9 dpa | 4.0 | 0.16 | - |
| | 1270°C, 5.8 dpa | 6.4 | 0.062 | - |
| | 800°C, 40.7 dpa | 2.7 | 0.28 | Katoh, |
| | 800°C, 71 dpa | 4.2 (0.9) ¹ | 0.14 | |
| | 500°C, 74 dpa | 1.2 (0.2) | 0.74 | |
| | 300°C, 71 dpa | 1.2 (0.3) | 0.74 | |
| SA3/ML-F | 440°C, 0.8 dpa | 3.8 | 0.22 | Katoh, 2010[73] |
| | 450°C, 2.0 dpa | 3.3 | 0.26 | |
| | 500°C, 3.0 dpa | 3.9 | 0.21 | |
| | 850°C, 3.5 dpa | 5.6 | 0.14 | |
| | 860°C, 5.3 dpa | 7.3 | 0.093 | |
| | 440°C, 0.8 dpa | 1.3 | 0.65 | Katoh, 2010[73] |
| HNLS/ML-F | 450°C, 2.0 dpa | 1.5 | 0.55 | |
| | 500°C, 3.0 dpa | 2.4 | 0.30 | |
| | 850°C, 3.5 dpa | 2.4 | 0.30 | |
| | 860°C, 5.3 dpa | 2.6 | 0.27 | |

1: numbers in parentheses are one standard deviations

The effect of irradiation on the thermal conductivity of ceramics can be adequately described by the defect thermal resistivity model proposed by Snead et al. [101],

$$K_{irr}^{-1} = K_0^{-1} + K_{rd}^{-1}, \quad (6)$$

where K_{irr}^{-1} and K_0^{-1} denote irradiated and unirradiated thermal resistivity, respectively, and K_{rd}^{-1} is the radiation defect thermal resistivity that represents collective contributions from various radiation-produced defects to the volume thermal resistivity. Note that the unirradiated thermal resistivity may further be broken down into Umklapp and as-fabricated defect contributions. The radiation defect thermal resistivity values have been demonstrated to be proportional to the magnitude of transient swelling [93].

In Figure 13, irradiation temperature dependence of the radiation defect thermal resistivity is shown for 2D SiC/SiC composites [73, 94]. Plotted together are the data for high-purity CVD SiC replotted from Refs. [17, 102-104], showing a linear relationship between the radiation-defect thermal diffusivity and irradiation temperature. It is interesting to note that while the trend of temperature dependence is similar for all materials, different materials exhibit

different radiation-defect thermal resistivity with a ranking order of HNLS composites > SA3 composites ~ SA-Tyrannohex (hot-pressed SA3 fiber composite without the matrix) > CVD SiC. This observation indicates an interesting trend that the materials with the greater as-fabricated thermal resistivity develop the greater radiation defect thermal resistivity for a given irradiation condition.

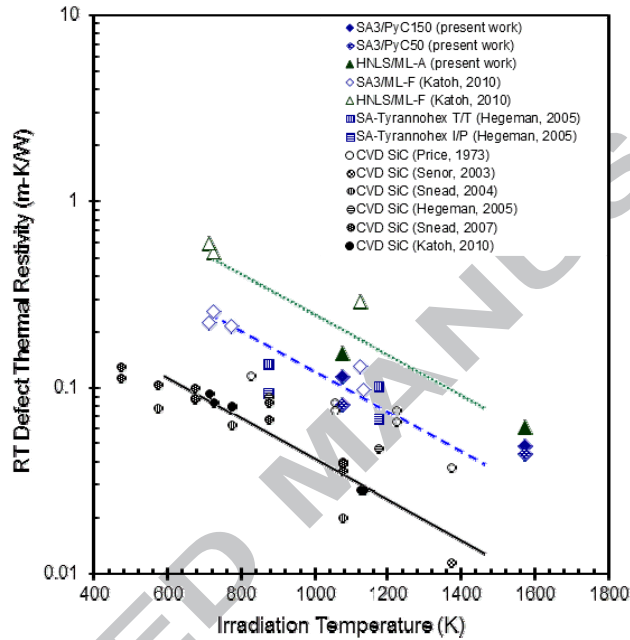


Figure 13. Radiation-defect thermal resistivity at room temperature for neutron-irradiated 2D SiC/SiC composites plotted against irradiation temperature [17, 73, 94, 102-104].

Figure 14 presents the thermal conductivity for the same materials plotted as a function of measurement temperature. The through-thickness thermal conductivity for these materials indicated only mild dependence on the measurement temperature, similar to the results from other work [73]. This is because the irradiated thermal resistivity in Eq. 6 is dominated by the radiation-defect resistivity that exhibits weak temperature dependence, as shown in Figure 15. The as-fabricated defect thermal resistivity is also anticipated to be insensitive to temperature. Because of the weak temperature dependence of these defect thermal resistivity factors, the thermal conductivity of the irradiated composites in general is only mildly correlated with the measurement temperature, exhibiting an increasingly negative correlation with the greater Umklapp contribution (or lesser defect contribution). The temperature-dependent thermal conductivity of irradiated SiC-based materials is predictable, to a certain extent, using Eq. 6, the relationship between temperature and thermal diffusivity in Figure 12, the fact that the

radiation defect thermal resistivity is roughly constant over temperature, and limited experimental data at room temperature.

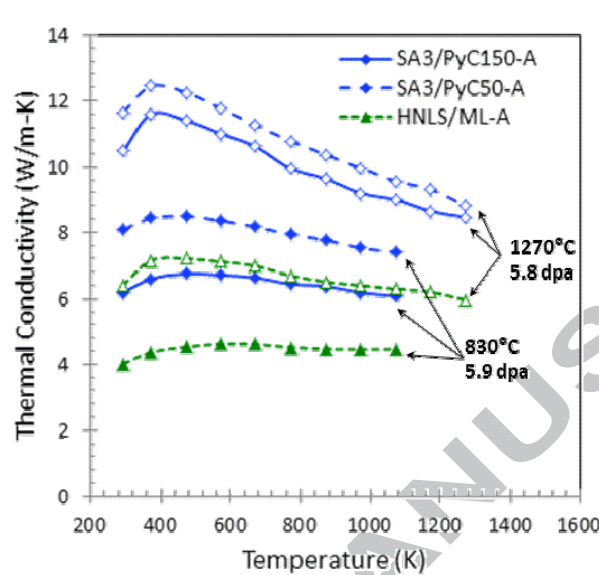


Figure 14. Through-thickness thermal conductivity of neutron-irradiated 2D SiC/SiC composites as a function of measurement temperature.

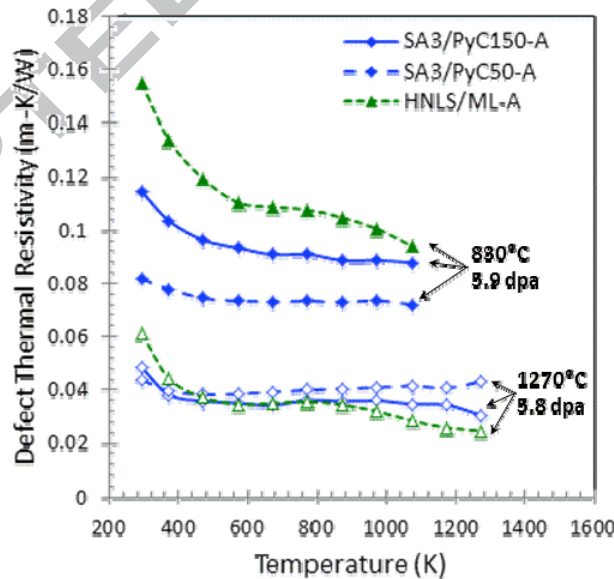


Figure 15. Radiation defect thermal diffusivity for neutron-irradiated 2D SiC/SiC composites as a function of measurement temperature.

4.2.3 Electrical Conductivity

4.2.3.1 Non-irradiated property

Electrical conductivity is an important property for SiC/SiC composites when they are considered for such applications as the flow channel inserts for liquid-metal-cooled fusion blankets and fission chambers for high-temperature reactors. While the volume electrical resistivity of pyrocarbon interphase typically falls in the range ~ 3 to $\sim 10 \times 10^4$ S/m [105] and is only weakly temperature dependent, SiC as a wide-gap impurity semiconductor is known to exhibit resistivity in a wide range from semi-insulating to >100 S/m, depending on the doping/impurity condition and temperature. In other words, the SiC matrix conductivity can be tailored in a fairly broad range, most commonly by adjusting the nitrogen content in the same way as to control the electrical resistivity of CVD SiC. In the SiC fiber-reinforced CVI SiC matrix composites, therefore, it is anticipated that the electrical conductivity values and their temperature dependence are significantly different between the fiber and the matrix.

Because of the strong temperature dependence of the SiC electrical conductivity, at relatively low temperatures (typically $<\sim 500^\circ\text{C}$), the CVI SiC/SiC composite may electrically be described as a body with conductive pyrocarbon interphase films embedded in the significantly less-conductive SiC matrix. In this regime of $\sigma_{\text{PyC}} \gg \sigma_{\text{SiC}}$, where σ denotes electrical conductivity, the bypass conduction through PyC dominates the composite conductivity when the interphase forms an interconnected network along the direction of electrical potential, whereas the less-conductive SiC dominates when the PyC network is disconnected. These trends are clearly seen in Figure 16 [41, 43, 106], which shows the nearly temperature-independent electrical conductivity for the in-plane (along one of the fiber axes) orientation for the 2D SiC/SiC composites due to the PyC bypass mechanism. In the through-thickness orientation, the composite exhibits lower electrical conductivity with a similar trend to the in-plane orientation when the PyC network is interconnected, whereas an Arrhenius-like trend becomes apparent when the PyC network is disconnected.

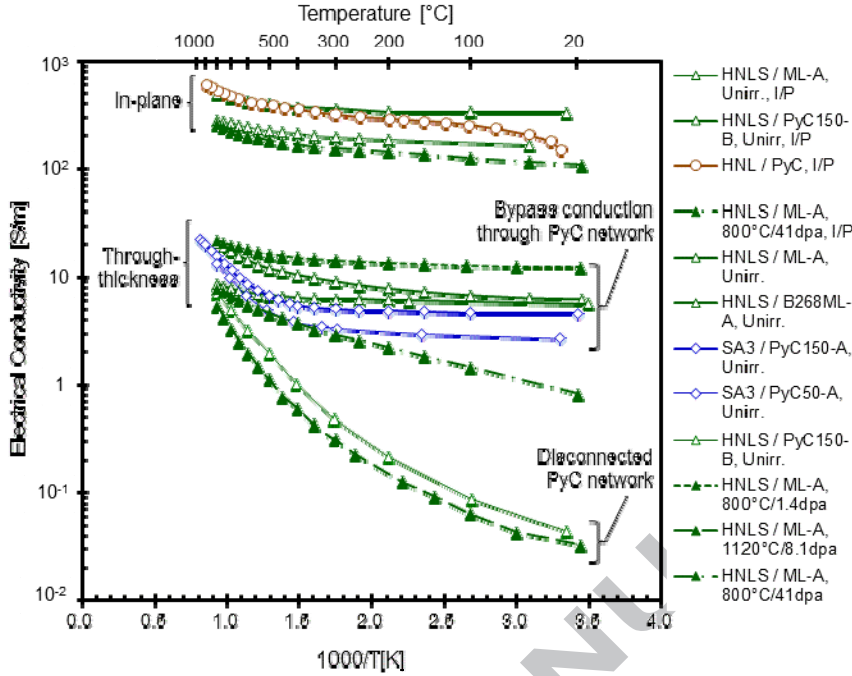


Figure 16. Temperature-dependent electrical conductivity for 2D SiC/SiC composites in unirradiated condition. Through-thickness electrical conductivity may be dominated by PyC bypass or SiC matrix, whereas in-plane conductivity is dominated by bypass mechanism. I/P stands for in-plane. [41, 43, 106]

Limited experimental data suggests that the simple model below gives reasonable approximation of the in-plane (c_{ip}) and through-thickness (c_{tt}) electrical conductivity for the orthogonal 2D SiC/SiC composites in the PyC network-domination regime.

$$c_{ip} \approx c_{PyC} f_{PyC} / 2 \quad (7)$$

$$c_{tt} \approx \eta c_{PyC} f_{PyC} / 2, \quad (8)$$

where f_{PyC} denotes the volume fraction of PyC in the composite. η (> 0) is the networking efficiency factor for the through-thickness conduction and is reported to takes values of ~ 1 to a few percent depending on the interphase thickness and the multi-layer configuration [41].

4.2.3.2 Effect of irradiation

The effect of neutron irradiation on electrical conductivity of SiC/SiC composites obviously depends on but may also alter the dominating conduction mechanism. The neutron irradiation may change the electrical conductivity of PyC by a factor of 2 without altering its very weak

temperature dependence. The change may be an increase or a decrease, depending on the initial quality of PyC and the irradiation condition. In contrast, the neutron irradiation effect on the SiC electrical conductivity is far more drastic because it involves alterations of species, concentration, and mobility of the carrier. Therefore, when the electrical conduction of the subject composite in the condition of interest is controlled by the PyC bypass mechanism, the effect of irradiation will be mild and more predictable. Otherwise, when the composite electrical conductivity is governed by the electrical properties of SiC, an experimental evaluation in the pertinent condition will likely be required to determine the effects of irradiation. Limited data that are available in the open literature indicate 0.1 to 10 S/m for the non-bypassed through-thickness conductivity of 2D SiC/SiC composites after neutron irradiation up to ~41 dpa and in a temperature range of 800 to 1120°C [41, 43].

4.3 Mechanical Properties

4.3.1 Elastic Constants

4.3.1.1 Non-irradiated property

The in-plane dynamic Young's modulus, tensile tangent modulus, tensile PLS, and the ultimate tensile stress (UTS) for various 2D near-stoichiometric SiC fiber CVI SiC matrix composites are compiled in Table 6 [68-71, 73]. The tensile tangent modulus determined by uni-axial mechanical testing typically falls in the range 200 to 280 GPa regardless of loading orientation. Modulus values below this range were observed for the three HNLS composites that bore unusually high porosity and for the SA3-P120/PyC150 due to the extensive matrix micro-cracking. In general, the tensile tangent modulus is found to be correlated with porosity, as shown in Figure 17.

Table 6. Compilation of in-plane dynamic Young's modulus, tensile tangent modulus, proportional limit stress, and ultimate tensile strength for various near-stoichiometric SiC fiber CVI SiC matrix composites in 2D architectures in unirradiated condition. All tests were conducted at room temperature. Limited in-plane compressive properties are also included. Numbers in parentheses denote one standard deviation.

| Material | Loading Mode | Dynamic Young's Modulus [GPa] | Tangent Modulus [GPa] | Proportional Limit Stress [MPa] | Ultimate Stress [MPa] | Strain to Failure [%] | No. of Tests | Ref. |
|-----------------|----------------------------|-------------------------------|-----------------------|---------------------------------|-----------------------|-----------------------|--------------|------------------|
| SA3/PyC150-A | Tensile, 0° | 254 (11) | 204 (14) | 119 (20) | 278 (22) | 0.24 (0.03) | 20 | - |
| SA3/PyC50-A | Tensile, 0° | 273 (12) | 232 (27) | 105 (9) | 287 (16) | 0.22 (0.03) | 8 | Katoh, 2011[68] |
| SA3T/PyC150-A | Tensile, 0° | 250 (16) | 204 (20) | 100 (17) | 318 (33) | 0.29 (0.05) | 13 | Katoh, 2011[68] |
| HNLS/PyC150-A | Tensile, 0° | 224 (11) | 151 (17) | 79 (21) | 343 (4) | 0.85 (0.12) | 4 | Katoh, 2011[68] |
| HNLS/PyC50-A | Tensile, 0° | 217 (22) | 163 (23) | 85 (8) | 306 (15) | 0.74 (0.08) | 8 | Katoh, 2011[68] |
| HNLS/ML-A | Tensile, 0° | 210 (18) | 176 (12) | 107 (15) | 230 (22) | 0.20 (0.03) | 6 | Katoh, 2011[68] |
| HNLS/PyC150-B | Tensile, 0° | - | 257 (37) | 110 (15) | 378 (51) | 0.61 (0.10) | 12 | - |
| SA3/PyC150-C | Tensile, 0° | - | 273 (23) | 103 (21) | 199 (2) | - | 2 | Nozawa, 2005[69] |
| HNLS/PyC150-C | Tensile, 0° | - | 244 (6) | 101 (9) | 226 (50) | - | 4 | Nozawa, 2005[69] |
| HNLS/PyC150-D | Tensile, 0° | 276 (9) | 277 (8) | 111 (14) | 346 (39) | 0.34 (0.05) | 30 | Nozawa, 2007[70] |
| | Tensile ¹ , 0° | - | 256 (27) | 114 (9) | 348 (38) | 0.62 (0.10) | 4 | Nozawa, 2007[70] |
| | Tensile, 45° | 232 (11) | 248 (21) | 136 (8) | 206 (19) | 0.33 (0.20) | 15 | Nozawa, 2007[70] |
| | Tensile ¹ , 45° | - | 232 (23) | 102 (11) | 206 (5) | 0.44 (0.06) | 4 | Nozawa, 2007[70] |
| SA3/PyC150-3 -D | Tensile, 0° | 249 (7) | 263 (15) | 117 (13) | 249 (23) | 0.13 (0.05) | 15 | - |
| | Tensile ¹ , 0° | - | 259 (16) | 93 (22) | 236 (1) | 0.19 (0.03) | 3 | - |
| SA3/PyC150-E | Tensile, 0° | - | 263 (21) | 116 (16) | 269 (23) | 0.20 (0.03) | n/r | Nozawa, 2012[71] |
| | Tensile, 45° | - | 220 (23) | 112 (16) | 174 (12) | 0.15 (0.03) | n/r | Nozawa, 2012[71] |
| | Compressive, 0° | - | 289 (4) | 396 (38) | 427 (33) | 0.15 (0.01) | n/r | Nozawa, 2012[71] |
| | Compressive, 45° | - | 249 (14) | 411 (57) | 426 (68) | 0.16 (0.02) | n/r | Nozawa, 2012[71] |
| SA3-P120/PyC150 | Tensile, 0° | 129 (21) | 103 (22) | 69 (28) | 141 (60) | 0.20 (0.10) | 10 | Nozawa, 2005[69] |
| | Tensile, 0° | - | 95 (10) | 47 (1) | 98 (1) | - | 4 | Nozawa, 2005[69] |
| HNLS/ML-F | Tensile ² , 0° | - | 226 (27) | 94 (18) | 281 (24) | 0.28 (0.07) | 15 | Katoh, 2010[73] |
| SA3/ML-F | Tensile ² , 0° | - | 218 (32) | 112 (30) | 266 (33) | 0.22 (0.05) | 10 | Katoh, 2010[73] |

1: Shoulder-loaded, gauge dimensions 32 mm (L) x 6.34 mm (W) x 3.38 mm (t); 2: Shoulder-loaded, gauge dimensions 15 mm (L) x 3 mm (W) x 2.3 mm (t); All other tensile tests were conducted by face-loading with gauge dimensions >16 mm (L) x 4 mm (W) x 1.5 – 2 mm (t).

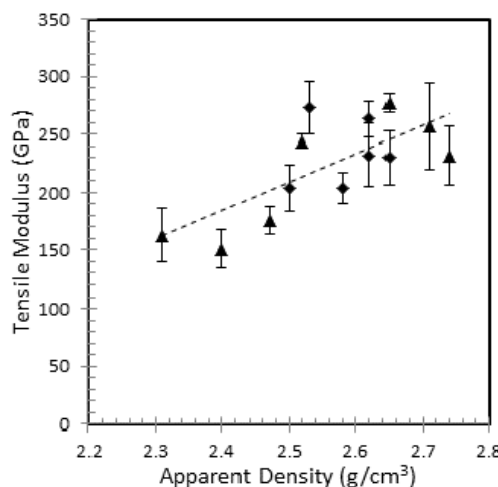


Figure 17. Correlation between tensile tangent modulus and porosity.

The dynamic Young's modulus determined by the impulse excitation and vibration method tends to be higher than the tensile tangent modulus (Fig. 18). The more pronounced difference observed in these two modulus values for the HNLS/PyC50-A and HNLS/PyC150-A, both of which are of very high porosity, is consistent with the explanation that the discrepancy may be attributed to the differences in deformation mode and the range of strain. Ishikawa et al. [98] and Morscher [107] have shown that rather simple constitutive models based on the rule of mixtures are capable of reasonably explaining the elastic modulus for ceramic matrix composite materials.

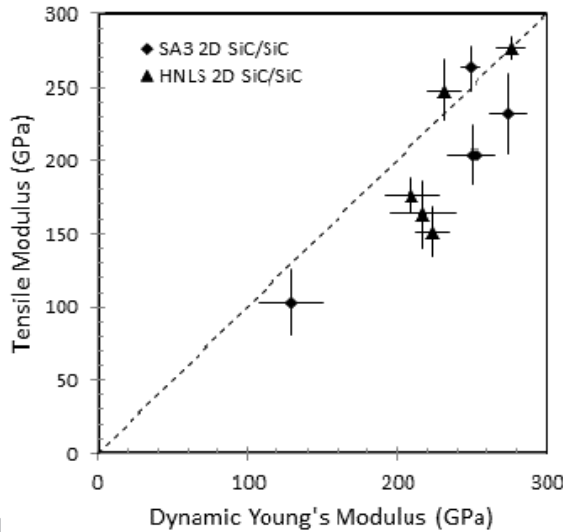


Figure 18. Correlation of dynamic Young's modulus and tensile tangent modulus for CVI SiC/SiC composites in unirradiated condition. Error bars indicate \pm one standard deviation.

Table 6 includes information for anisotropic elastic properties, which are important for the purpose of designing components with these materials. It is shown that the tangent modulus along the $\pm 45^\circ$ orientation in the 2D $0^\circ/90^\circ$ lay-up architecture is ~ 15 percent lower than in the major fiber axis ($0^\circ/90^\circ$) orientation. The classical ply theory [108, 109] predicts the gradual variation of tangent modulus with the rotation angle from its maximum at $0^\circ/90^\circ$ to the minimum at $\pm 45^\circ$. On the contrary, the in-plane Poisson's ratio takes its peak value at $\pm 45^\circ$ and minimum value at $\pm 0^\circ/90^\circ$. These trends are very consistent for both tensile and compressive loadings [71]. Owing to the matrix being made of high-modulus SiC, in-plane anisotropy in elastic properties is relatively insignificant for the CVI SiC-matrix composites compared to the other composites with less rigid matrices such as polymer-derived SiC and pyrolytic carbon.

Sakata and Ohnabe [110] report a lack of significant effects on elastic properties of CG-Nicalon CVI SiC composites at elevated temperature up to 1200°C. It is reasonable to assume that the near-stoichiometric SiC fiber composites, with the high-temperature stability improved and the CTE mismatch issue mitigated, maintain their room-temperature elastic properties up to the same temperature in inert environments. However, the elastic modulus of these composites should reflect the inherent temperature dependence of the elastic modulus for SiC, which shows an ~6% decrease from room-temperature value to 1000°C.

4.3.1.2 Effect of irradiation

The effects of neutron irradiation on the dynamic Young's modulus and tensile properties measured for the 2D SiC/SiC composites are summarized in Table 7 [69, 73, 87]. The irradiation-induced changes in the dynamic Young's modulus and the tensile tangent modulus are shown in Figure 19. Although individual data suffer relatively large uncertainties, as represented by the standard deviations shown by the vertical error bars, it is observed that in general the Young's modulus slightly decreased very slightly after irradiation at below ~1000°C. Since the Young's modulus for a fiber-reinforced composite material is determined by the rule of mixtures, the effect of irradiation for the composites may be assumed to follow the trend for a monolithic beta-phase SiC that is the sole constituent of the matrices and the main constituent of the fibers. The effect of irradiation on Young's modulus of CVD SiC, or the dense polycrystalline form beta-phase SiC, is well documented in Ref. [17] and is shown to decrease by up to a few percent for irradiation at 800°C. An approximately linear relationship is anticipated between the Young's modulus decrease and the linear swelling by point defect accumulation with a correlation factor of ~10, implying ~7% decrease in Young's modulus at 300°C after the swelling saturation at slightly over 2% in volume.

Table 7. Compilation of tensile tangent modulus, proportional limit stress, and ultimate tensile stress for CVI SiC/SiC composites in irradiated conditions.

| Material | Irradiation Condition | Dynamic Young's Modulus [GPa] | Tangent Modulus [GPa] | Proportional Limit Stress [MPa] | Ultimate Stress [MPa] | Strain to Failure [%] | No. of Tests | Ref. |
|------------------|------------------------------|-------------------------------|-----------------------|---------------------------------|-----------------------|-----------------------|--------------|------------------|
| SA3/PyC150-A | Unirradiated | 254 (11) | 204 (14) | 119 (20) | 278 (22) | 0.24 (0.03) | 20 | |
| | 830°C, 5.9 dpa | 249 (20) | 203 (18) | 106 (15) | 304 (38) | 0.32 (0.06) | 5 | |
| | 1270°C, 5.8 dpa | 248 (9) | 212 (32) | 96 (18) | 274 (28) | 0.26 (0.04) | 6 | |
| SA3/PyC50-A | Unirradiated | 273 (12) | 232 (27) | 105 (9) | 287 (16) | 0.22 (0.03) | 8 | |
| | 830°C, 5.9 dpa | 273 (-) | 200 (-) | 101 (-) | 269 (-) | 0.23 (-) | 1 | |
| | 1270°C, 5.8 dpa | 267 (15) | 218 (13) | 122 (21) | 279 (7) | 0.23 (0.01) | 5 | |
| SA3T/PyC150-A | Unirradiated | 250 (16) | 204 (20) | 100 (17) | 318 (33) | 0.29 (0.05) | 13 | |
| | 830°C, 5.9 dpa | 239 (14) | 185 (27) | 109 (17) | 273 (38) | 0.25 (0.06) | 5 | |
| | 1270°C, 5.8 dpa | 224 (11) | 151 (17) | 79 (21) | 343 (4) | 0.85 (0.12) | 4 | |
| HNLS/PyC150-A | Unirradiated | 202 (12) | 145 (20) | 77 (18) | 309 (14) | 0.73 (0.05) | 8 | |
| | 830°C, 5.9 dpa | 192 (8) | 169 (14) | 79 (15) | 290 (17) | 0.76 (0.09) | 4 | |
| | 1270°C, 5.8 dpa | 217 (22) | 163 (23) | 85 (8) | 306 (15) | 0.74 (0.08) | 8 | |
| HNLS/PyC50-A | Unirradiated | 216 (21) | 163 (23) | 85 (8) | 306 (15) | 0.74 (0.08) | 8 | |
| | 830°C, 5.9 dpa | 189 (13) | 164 (23) | 70 (18) | 300 (13) | 0.76 (0.08) | 8 | |
| | 1270°C, 5.8 dpa | 210 (18) | 176 (12) | 107 (15) | 230 (22) | 0.20 (0.03) | 6 | |
| HNLS/ML-A | Unirradiated | 206 (15) | 185 (25) | 103 (18) | 249 (28) | 0.27 (0.06) | 6 | |
| | 830°C, 5.9 dpa | 208 (10) | 177 (25) | 100 (18) | 234 (21) | 0.27 (0.06) | 6 | |
| | 1270°C, 5.8 dpa | - | 257 (37) | 110 (15) | 378 (51) | 0.61 (0.10) | 12 | |
| HNLS/PyC150-B | Unirradiated | 225 (6) | 204 (37) | 113 (15) | 295 (36) | 0.60 (0.12) | 6 | |
| | 830°C, 5.9 dpa | 283 (11) | 231 (14) | 104 (12) | 339 (40) | 0.74 (0.14) | 4 | |
| | 1270°C, 5.8 dpa | 129 (21) | 103 (22) | 69 (28) | 141 (60) | 0.20 (0.10) | 10 | Nozawa, 2005[69] |
| SA3-P120/PyC150 | Unirradiated | 112 (19) | 90 (13) | 62 (16) | 129 (33) | 0.25 (0.10) | 5 | |
| | 830°C, 5.9 dpa | - | 226 (27) | 94 (18) | 281 (24) | 0.28 (0.07) | 15 | Katoh, 2010[73] |
| | 1000°C, 5.3 dpa | - | 243 (37) | 136 (25) | 243 (41) | 0.17 (0.06) | 20 | |
| HNLS/ML-F | 220 - 350°C, 0.48 - 0.96 dpa | - | 212 (38) | 116 (15) | 229 (39) | 0.17 (0.05) | 8 | |
| | 480 - 610°C, 1.6 - 2.8 dpa | - | 213 (28) | 113 (18) | 182 (30) | 0.12 (0.04) | 11 | |
| | Unirradiated | - | 218 (32) | 112 (30) | 266 (33) | 0.22 (0.05) | 10 | Katoh, 2010[73] |
| SA3/ML-F | 380 - 420°C, 0.31 - 1 dpa | - | 220 (44) | 106 (40) | 241 (38) | 0.21 (0.04) | 9 | |
| | 460 - 530°C, 1.2 - 1.8 dpa | - | 211 (19) | 89 (19) | 269 (21) | 0.26 (0.04) | 11 | |
| | 610 - 780°C, 1.9 - 3.5 dpa | - | 207 (21) | 88 (17) | 248 (28) | 0.26 (0.05) | 15 | |
| SA3/PyC40, #1266 | Unirradiated | - | 257 (32) | 76 (31) | 218 (18) | - | 6 | Ozawa, 2007[87] |
| | 740°C, 3.1 dpa | - | 216 (11) | 80 (9) | 241 (30) | - | 3 | |
| | 750°C, 12 dpa | - | 198 (19) | 112 (12) | 209 (11) | - | 3 | |
| HNLS/PyC40,#1272 | Unirradiated | - | 253 (25) | 98 (17) | 227 (27) | - | 10 | Ozawa, 2007[87] |
| | 740°C, 3.1 dpa | - | 222 (33) | 107 (9) | 210 (18) | - | 3 | |
| | 750°C, 12 dpa | - | 200 (5) | 100 (18) | 220 (16) | - | 4 | |

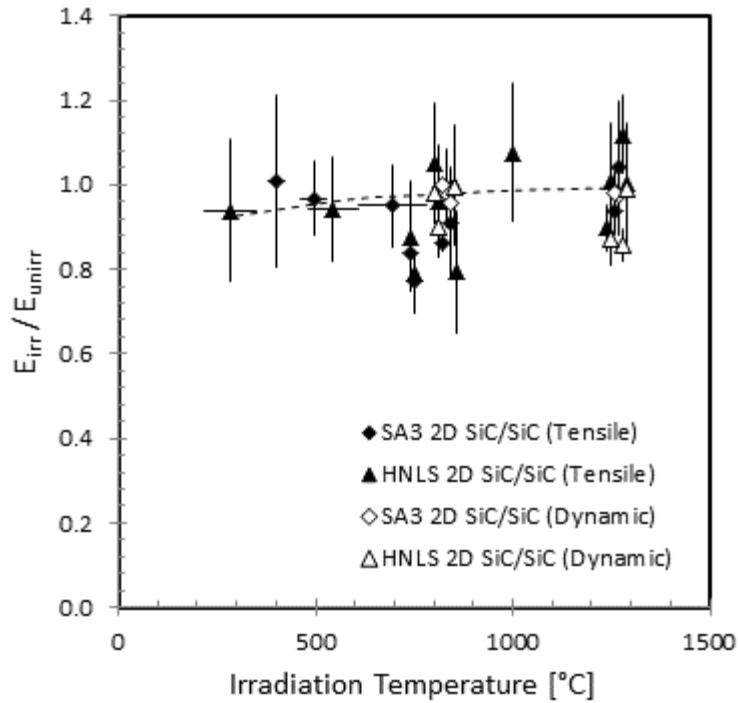


Figure 19. Tensile and dynamic Young's moduli for irradiated CVI SiC/SiC composites normalized to the unirradiated values. Vertical error bars indicate one standard deviation. Horizontal error bars indicate ranges of nominal irradiation temperature. Irradiation temperatures are slightly offset for visibility. The dashed line indicates prediction based on assumed modulus – swelling relationship (see text for discussion).

4.3.2 In-plane Strength

4.3.2.1 Non-irradiated properties

The PLS is considered to be the stress at which the matrix microcracks develop and start to open, accompanying fiber-matrix debond while the bridging fibers remain largely intact. The composites studied mostly exhibited the tensile PLS in the vicinity of 110 MPa, when tested using miniature beam specimens, excluding data for materials with unusually low density. The effects of specimen dimensions on the tensile properties are briefly discussed later. In Figure 20, the tensile PLS is plotted against the apparent mass density, clearly indicating the positive correlation between these two composite attributes. The figure also shows no obvious difference in the PLS between the 2D composites made with HNLS and SA3 fibers, despite the significant difference in surface roughness between the two fibers.

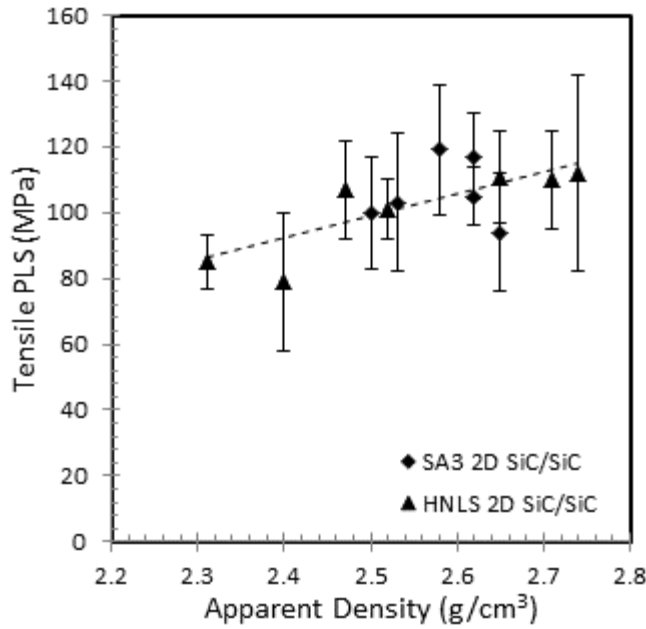


Figure 20. Correlation between composite density and tensile proportional limit stress.

The UTS values fell in the range 250 to 350 MPa for most composites evaluated or reported in literature. The UTS for a uni-directionally reinforced continuous fiber composite with a brittle matrix is given by Evans et al. [76] as

$$\sigma_{UTS} = V_f \sigma_c \cdot \left[\frac{2}{m+1} \right]^{\frac{1}{m+1}} \left(\frac{m+1}{m+2} \right), \quad (9)$$

where σ and m denote the Weibull scale and shape parameters, respectively, for the fiber strength. The typical volume fraction of aligned fibers (~ 19 percent) and measured fiber strength properties ($\sigma = \sim 2.6$ GPa for HNLS and ~ 2.0 GPa for SA3, and $m = 3$ to 4 for both fibers [73]) give an estimated UTS of slightly over 300 MPa for the HNLS composites and slightly over 250 MPa for the SA3 composites. Thus, the UTS values theoretically predicted for uni-directional composites agree reasonably well with the values measured for the 2D composites.

Typical stress-strain curves recorded during tensile tests of the composites are presented in Figure 21. Intermittent unloading-reloading sequences were incorporated in all of these tests in order to determine the matrix crack accumulation, residual mismatch stress, permanent strain, and the interfacial sliding stress parameters based on the hysteresis responses. Details of these hysteresis analyses are found in other publications [111, 112]. The intermittent unloading-reloading may possibly introduce additional damage as compared to monotonic loading,

though Katoh et al. have shown insignificant effects on the tensile properties determined due to a limited number of unloading-reloading sequences [73].

As shown in Figure 20, the HNLS composites generally show an extensive second linear segment in the tensile stress-strain behavior, whereas the SA3 composites tend to fail before the apparent matrix crack saturation is achieved. This difference is attributed to both a somewhat lower tensile strength and a larger interfacial sliding stress due to the enhanced surface roughness of the SA3 fiber. The previous study indicated that a PyC layer thickness greater than ~ 250 to ~ 650 nm is needed for the 2D SA3 fiber composites to achieve the extensive second linear behavior. The HNLS/ML exhibits similar tensile behavior to the SA3 composites, implying higher-than-optimum interfacial sliding stress. This indicates that the critical thickness of the PyC interphase for fully graceful failure of HNLS composites lies between ~ 20 nm, the thickness of the innermost PyC layer in the ML interphase in this work, and ~ 50 nm that has been shown to enable matrix crack saturation in this and previous [46] works. Beyond 50 nm, it has been shown that there is only very minor effects for PyC interphase thicknesses up to ~ 300 nm on PLS or UTS of near-stoichiometric CVI SiC/SiC [113]. The results of this study further confirmed this observation for the 2D HNLS fiber composites. The SA3-P120/PyC150-A composite exhibited poor tensile properties due primarily to the low axial fiber loading.

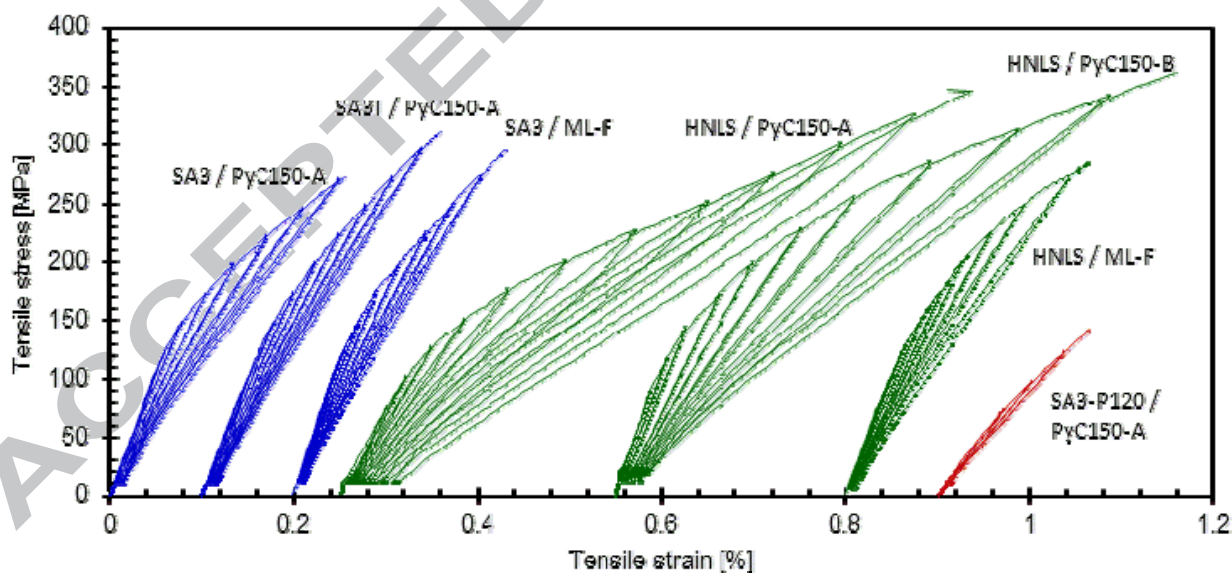


Figure 21. Representative stress-strain evolutions during tensile tests of 2D near-stoichiometric SiC fiber CVI SiC matrix composites at room temperature in unirradiated condition. Intermittent unloading-reloading sequences were incorporated to examine matrix cracking, permanent strain, residual stress, and hysteresis response.

In-plane shear properties are generally evaluated by the Iosipescu method (ASTM C1292) or the off-axial tensile method [114]. In the latter case, without considering the mixed failure mode criteria (e.g., Tsai-Wu criteria [115]), the obtained data are always underestimated regardless of material type or fabric architecture [71]. In contrast, the Iosipescu method, which can theoretically produce a purely shear in-plane stress field across the tested cross-section of concern, is more beneficial. Table 8 lists in-plane shear modulus and in-plane shear stress obtained by the Iosipescu method. Similar to the tensile case, the stress-strain curve generally shows initial linearity, followed by a non-linear section due mainly to progressive accumulation of micro-cracks beyond the proportional limit. The main crack then propagates between two notches at the maximum stress. In many cases, the tortuous crack path provides some biases on the data, requiring this issue to be carefully discussed in precise evaluation of the data.

Table 8 also lists the elastic properties, that is, tangent modulus and Poisson's ratios, by various test modes and loading directions. The elastic modulus generally decreases with increasing loading angle apart from the fiber longitudinal direction and vice versa for the Poisson's ratio. It is well known that the anisotropy of the elastic properties of most types of composites can simply be described using classical theories, that is, the rule of mixtures [108] and the ply theory [109]. The same is true for the nuclear-grade SiC/SiC composites.

Table 8. In-plane Poisson's ratios and shear properties for 2D SiC fiber CVI SiC matrix composites. [71]

| Material | Loading Mode | Poisson's Ratio | Tangent Modulus [GPa] | Shear Modulus [GPa] | Proportional Limit Shear Stress [MPa] | Ultimate Shear Stress [MPa] | Ref. |
|--------------|------------------|-----------------|-----------------------|-----------------------|---------------------------------------|-----------------------------|------------------|
| SA3/PyC150-E | Tensile, 0° | 0.13 (0.02) | 263 (21) | 116 (11) ¹ | | | Nozawa, 2012[71] |
| | Tensile, 45° | 0.25 (0.01) | 220 (23) | 88 (10) ¹ | | | |
| | Compressive, 0° | 0.13 (0.01) | 289 (4) | 131 (3) ¹ | | | |
| | Compressive, 45° | 0.23 (0.00) | 249 (14) | 107 (6) ¹ | | | |
| | Iosipescu, 0° | | | 99 (14) | 132 (31) | 153 (34) | |

1: Calculated from Poisson's ratio and tangent modulus.

4.3.2.2 Effects of gauge dimensions on in-plane tensile properties

For most irradiation studies, test specimens are used that are significantly smaller than the standard specimens recommended in the ASTM test standards or that are used in standard practices. Such compromises are in most cases inevitable because of the space availability (or affordability) in irradiation vehicles. Therefore, it is important to establish understanding of the effects of test specimen dimensions on the composite properties, in particular strength.

From many studies of the specimen size effect on various types of SiC/SiC composites through different processing routes [116-118], it is understood that there is no marked gauge size effect shown for the axial (0° loading) tensile strength in the case where at least a few numbers of the unit structure (e.g., fiber bundle interval) are included in the gauge. For the typical 2D woven fabric SiC/SiC composites with $n_t = \sim 0.6 \text{ mm}^{-1}$ in-plane and $n_p = \sim 4 \text{ mm}^{-1}$ through-thickness, tensile test specimens with a gauge width $>\sim 3 \text{ mm}$ and a thickness $>\sim 2 \text{ mm}$ are commonly used for neutron irradiation studies and have been demonstrated to provide on-axis tensile properties that are reasonably reproducible and comparable with the properties obtained using larger test specimens.

Conversely, if the specimen size is nearly equivalent to or smaller than the structural unit size, the actual fiber volume fraction and porosity significantly vary and unevenly distribute, resulting in apparent effects on the on-axis strength properties such as in-plane PLS and UTS. However in such cases, it has been shown that the PLS and UTS values still reasonably represent the properties of larger test specimens when normalized to the actual axial fiber volume fractions measured for individual test specimens [116, 117].

Contrary to the tensile strength in one of the principal fiber orientations, the off-axis in-plane tensile strength seems to decrease as the specimen width decreases, particularly to below twice the unit cell width [116, 118]. Typical fracture surfaces after off-axis tensile failure show the main crack propagation along the fibers rather than perpendicular to the loading direction. This indicates the importance of the roles of the in-plane shear and inter-laminar detachment modes, both of which are considered as major failure modes, and/or combined effects (e.g., tensile, compressive, in-plane shear, and inter-laminar detachment). In a separate discussion of the size effect on the in-plane shear properties by the Iosipescu tests, which can theoretically generate the pure in-plane shear stress field in the composites, no noticeable specimen width effect was reported [116, 118]. Alternatively, the inter-laminar shear detachment mode will impact the results, but the extent of the impact is presently uncertain. Further investigation is therefore necessary to find the key mechanism. In contrast, no notable specimen length and thickness effects are obtained.

4.3.2.3 Effect of irradiation

Table 7 summarizes the effects of neutron irradiation on the in-plane tensile properties of the nuclear-grade CVI SiC/SiC composites from the present work and found in the literature [69, 73, 87]. In general, it is safe to say that there are not substantial effects of neutron irradiation on the tensile strength properties in the irradiation conditions tested. In fact, the difference between the pre-irradiation and post-irradiation values for PLS or UTS for these composites barely exceeds one standard deviation, as seen in Figures 22 and 23, which visualize the effects

of irradiation on the tensile PLS and UTS, respectively. Furthermore, no significant or detrimental effects of irradiation on the tensile load-displacement curves have been noted or reported [68].

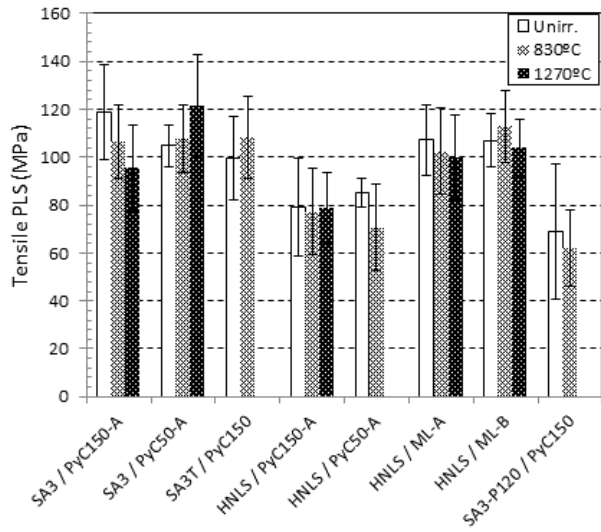


Figure 22. Effects of neutron irradiation on tensile proportional limit stress for various 2D CVI SiC/SiC composites. Irradiation conditions are 5.9 dpa at 830°C and 5.8 dpa at 1270°C. Error bars indicate \pm one standard deviation.

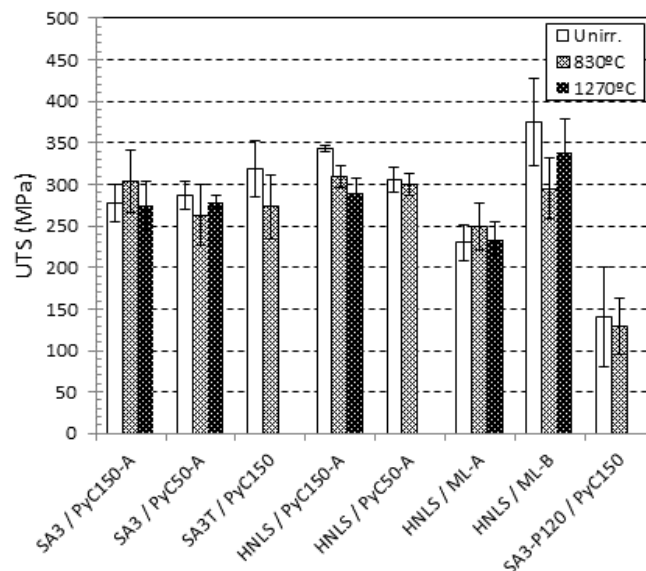


Figure 23. Effects of neutron irradiation on ultimate tensile stress for various 2D CVI SiC/SiC composites. Irradiation conditions are 5.9 dpa at 830°C and 5.8 dpa at 1270°C. Error bars indicate \pm one standard deviation.

As discussed above, the composite UTS is governed ideally by the statistical strength properties of the fibers alone. Thus the insensitivity of UTS to irradiation implies lack of irradiation effects on the in situ strength of either type fiber, if not strengthening. Some of the data published in literature indicate a slight increase in UTS for similar composites after neutron irradiation [73, 119], implying slight irradiation-induced strengthening for these fibers.

The composite proportional limit is considered to approximately correspond with the condition in which a transverse crack is developed in the matrix surrounding 0° fiber bundles, or 0° minimatrix [74]. When elastic moduli for the matrix and fibers are given and constant, tensile stress loading to the 0° minimatrix is determined solely by the tensile stress to composite and residual thermal stress. According to a model by Curtin [120], the criterion for cracking of the 0° minimatrix is proportional to the 1/3 power of the interfacial sliding stress and the matrix fracture energy, again with elastic moduli remaining constant. Katoh et al. showed the decrease in residual thermal stress, which is caused by irradiation lowering the matrix cracking stress, is compensated by the likely increase in true matrix cracking stress by irradiation [68]. The irradiation-induced increase in fracture toughness of CVD SiC has been discussed and perceived likely [17, 121]. The effects of irradiation on the interfacial sliding properties will be discussed later.

4.3.3 Statistical Strength

A comprehensive study on the statistical mechanical properties of a continuous SiC fiber composite was performed by Gonczy and Jenkins for Sylramic S-200, a 2D ceramic-grade Nicalon-reinforced silicon carbonitride matrix composite [122]. The results of the study indicate that the statistics for the UTS is best described by a normal or lognormal distribution but is only poorly described by the two-parameter Weibull distribution. Based on that, the UTS is statistically analyzed under an assumption of normal distribution in this work. Note that adequacy of the assumption for two-parameter Weibull distribution has not been validated for the PLS either, though the two-parameter Weibull analysis is provided for the PLS below.

Statistical tensile properties acquired in the present work are summarized as the coefficient of variation (CV) for the PLS and UTS and the two parameter Weibull statistic for the PLS, in Table 9. Because the tensile properties for the composites with nominally 50 nm and 150 nm PyC interphases appeared very similar, the data for both interphase composites were combined to maximize population of the data set. Data from Ref. [73] for similar materials are shown together. Among the data sets consisting of more than 10 test populations listed in

Table 9, only two data sets are based on the test populations that are considered to be the minimum to generate the two-parameter Weibull statistics (~30). However, the statistical tensile properties appear reasonably consistent across materials in different production lots or with different fiber grades or interphases.

Table 9. Statistical tensile properties for selected near-stoichiometric SiC fiber CVI SiC matrix composites in 2D architectures.

| Material ¹ | PLS [MPa], Normal Average | PLS, CV ² | PLS [MPa], Weibull Char. | PLS, Weibull Modulus | UTS [MPa], Normal Average | UTS, CV ² | No. of Tests | Ref. |
|-------------------------|---------------------------|----------------------|--------------------------|----------------------|---------------------------|----------------------|--------------|-----------------|
| SA3/PyC50&150-A | 113 | 0.16 | 120 | 7.5 | 280 | 0.08 | 28 | - |
| HNLS/PyC50&150-A | 83 | 0.15 | 88 | 7.3 | 318 | 0.04 | 12 | - |
| SA3T/PyC150-A | 100 | 0.17 | 107 | 6.9 | 318 | 0.10 | 13 | - |
| HNLS/PyC150-B | 110 | 0.14 | 117 | 7.9 | 378 | 0.13 | 12 | - |
| HNLS/PyC150-D | 111 | 0.13 | 117 | 11.0 | 346 | 0.11 | 30 | - |
| HNLS/PyC150-D (±45°) | 121 | 0.19 | 129 | 6.0 | 206 | 0.09 | 15 | - |
| SA3/PyC150-D | 107 | 0.20 | 116 | 5.8 | 249 | 0.09 | 15 | - |
| SA3/ML-F | 112 | 0.27 | 127 | 3.7 | 266 | 0.12 | 10 | Katoh, 2010[73] |
| HNLS/ML-F | 94 | 0.19 | 101 | 5.8 | 281 | 0.09 | 15 | Katoh, 2010[73] |

1: Test orientation is 0°/90° unless otherwise noted; 2: Coefficient of Variation

The UTS generally suffers moderate scatter with typical coefficients of variation (CV's) on the order of ~0.1. This is due to the fact that the UTS is determined mainly by the statistical strength properties of a large number of the reinforcing fibers, as ideally described by Eq. 9, contrasting with the larger scatter for the PLS that is determined by statistical cracking of a much smaller number of the mini-matrix elements.

In fact, CV's for the PLS fall mostly in a range 0.15 to 0.2, with an average of ~0.18. The Weibull moduli of 6 to 8 correspond with these relatively significant scatters in the PLS, with a few exceptions, as shown in Table 9. The data in Table 9 also suggests that the Weibull modulus of ~10 will be achievable for the PLS with a carefully controlled fabrication process. These values also coincide with the typical Weibull moduli for flexural strength of CVD SiC. The Weibull modulus for high-purity CVD SiC has most commonly been reported to be within a range of 6 to 10 [17].

Results of a statistical analysis on tensile properties for the irradiated composites are summarized in Table 10. No outstanding effects of irradiation on CV's for UTS or PLS were observed, confirming the general lack of significant effects on the mechanical properties for SiC/SiC composites in this class. The lack of irradiation effects on the statistical aspects of the

UTS confirms the irradiation tolerance of the fibers in terms of the in situ statistical strength. Although the CV's for the PLS appear to slightly decrease after irradiation, the changes stay within the statistical uncertainty. Overall, the effects of neutron irradiation on the statistical strength properties do not appear significant for these materials; however, more data will be needed when the failure probability as a function of loading condition is an important design concern.

Table 10. Statistical tensile properties for irradiated CVI SiC/SiC composites. Statistical flexural strength data for high-purity CVD SiC obtained in the same experiment are shown together.

| Material | Irradiation Condition | PLS ¹ [MPa], Normal Average | PLS ¹ , CV | PLS ¹ [MPa], Weibull Char. | PLS ¹ , Weibull Modulus | UTS [MPa], Normal Average | UTS, CV | No. of Tests |
|-----------------------------|----------------------------|--|-----------------------|---------------------------------------|------------------------------------|---------------------------|---------|--------------|
| SA3/PyC50&150-A | Unirradiated | 113 | 0.16 | 120 | 7.5 | 280 | 0.08 | 28 |
| | 800°C, 5.9 dpa | 101 | 0.13 | 107 | 7.1 | 291 | 0.06 | 6 |
| | 1300°C, 5.8 dpa | 108 | 0.19 | 117 | 5.9 | 273 | 0.09 | 11 |
| HNLS/PyC50&150-A | Unirradiated | 83 | 0.15 | 88 | 7.3 | 318 | 0.04 | 12 |
| | 800°C, 5.9 dpa | 74 | 0.24 | 81 | 4.6 | 305 | 0.05 | 16 |
| HNLS/ML-F | Unirradiated | 94 | 0.19 | 101 | 5.8 | 281 | 0.09 | 15 |
| | 1000°C, 5.3 dpa | 136 | 0.18 | 147 | 6.2 | 243 | 0.17 | 20 |
| | 480 – 610°C, 1.6 – 2.8 dpa | 113 | 0.16 | 121 | 7.4 | 182 | 0.16 | 11 |
| SA3/ML-F | Unirradiated | 112 | 0.27 | 124 | 4.5 | 266 | 0.12 | 10 |
| | 460 - 530°C, 1.2 – 1.8 dpa | 89 | 0.21 | 96 | 5.3 | 269 | 0.08 | 11 |
| | 610 - 780°C, 1.9 – 3.5 dpa | 88 | 0.19 | 95 | 6.2 | 248 | 0.11 | 15 |
| CVD SiC (R&H ²) | Unirradiated | 417 | 0.20 | 451 | 5.7 | - | - | 30 |
| | 800°C, 5.9 dpa | 429 | 0.17 | 458 | 7.2 | - | - | 23 |
| | 1300°C, 5.8 dpa | 412 | 0.18 | 442 | 6.5 | - | - | 27 |

1: Flexural strength for CVD SiC; 2: Rohm and Haas Advanced Materials

4.3.4 Interface Properties

4.3.4.1 Non-irradiated property

Interface properties

Single-fiber push-out tests were conducted at room temperature using a nano-indentation test system. A thin-strip sample with a thickness of 30–220 µm was bonded on the holder with narrow grooves. The fibers above the grooves were then randomly selected, and each fiber was loaded by monotonic compression. Figure 24 shows a typical load vs. displacement curve with schematic test images. From the figure, two push-out parameters, (1) a debond initiation stress (σ) and (2) a complete debonding and sliding stress (σ_{max}), are experimentally obtained. Then,

two interfacial shear properties, (1) an interfacial debond shear strength, IDSS (τ) as a critical shear stress to induce an interfacial crack along the bonded F/M interface, and (2) an interfacial friction stress, IFS (τ) at the debonded interface, are calculated using these experimental results. Of various analytical models [123-131], a non-linear double shear-lag model with consideration of the axial and radial anisotropy [131] was employed to determine τ with consideration of (1) the radial dependence of the axial stresses in both the fiber and the matrix, (2) the shear stress distribution in the matrix, (3) the exact equilibrium equation in relating the tangential stress to the radial stress at the interface, and (4) anisotropy of the constituents. Specifically, residual stresses induced by thermal expansion mismatch and by differential swelling among the fiber, F/M interphase, and matrix can be discussed together in the model, although the effect of dynamic phenomena such as irradiation creep of SiC and PyC was ignored for simplicity. In contrast, the updated Shetty's model [129] was applied to determine τ for the debonded interface. Details of the single-fiber push-out test technique have been described elsewhere [131].

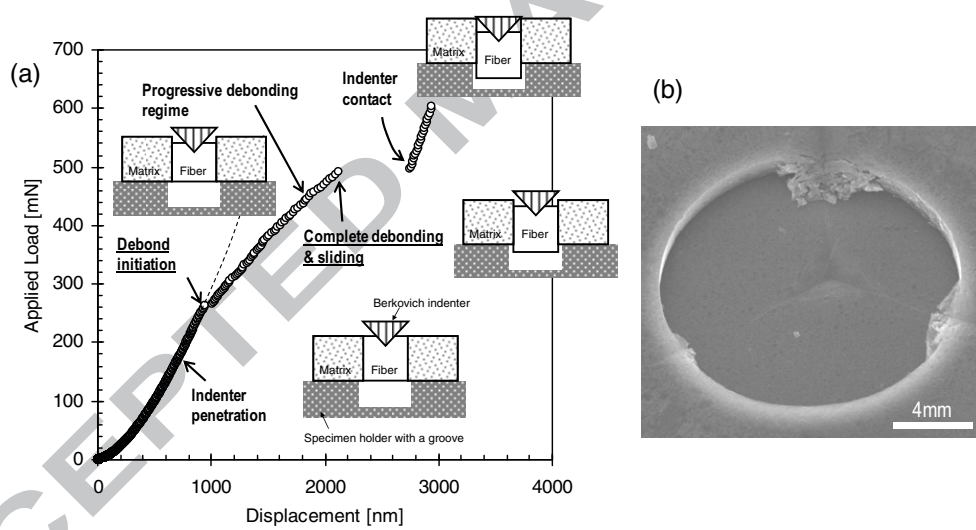


Figure 24. Typical load-vs.-displacement curve of the single-fiber push-out test for the fiber/matrix interfacial shear evaluation (a) and a typical pushed-out fiber surface image (b). The load initially increases with penetration of the indenter tip, and then an interfacial debond occurs from the loading front side. With expansion of the debonded area, the load further increases and achieves the maximum by the completion of debond, and rapid displacement increase is then obtained by sliding at the interface. Further increase of the load after sliding is due to contact of the indenter edges with matrix.

Figure 25 shows the effects of PyC interlayer thickness on the interfacial debond shear strength (IDSS) and the interfacial friction stress (IFS) at room temperature for non-irradiated CVI-SiC/SiC composites. Note that with many assumptions in analysis of the push-out test, data scatter of the plots is due primarily to the analytical aspects such as non-uniform distribution of the pores and/or scatter of the fiber diameter, as well as technical aspects such as precision of the specimen surface preparation by metallographic polishing.

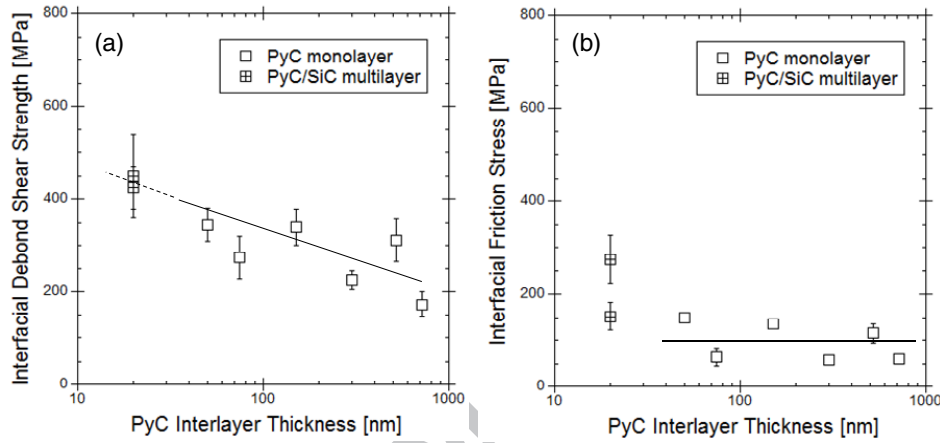


Figure 25. Effects of PyC interlayer thickness on the interfacial debond shear strength (a) and the interfacial friction stress (b) at room temperature. Note that the thickness of the inner PyC adjacent to the SiC fiber is used in the plotting of multi-layered PyC/SiC interface test cases.

For the PyC monolayer composite case, IDSS tends to decrease with increasing PyC interlayer thickness. The trend of the IDSS reduction is quite similar to that of the proportional limit stresses from tensile tests [47]. For both micro- and macro-strengths, it is well known that the thermally induced residual stress affects these strengths. Recent parametric studies by Nozawa et al. [131] demonstrated the possible degradation of the thermally induced radial clamping stress at the F/M interface with increasing PyC interlayer thickness when assuming that the coefficient of thermal expansion of Hi-Nicalon Type S fiber is greater than that of CVD-SiC. For the multilayer composites, the first PyC interlayer adjacent to the fiber is very important in precise discussion since the main crack generally propagates along or within the first PyC layer. When summarizing push-out data from the first PyC interlayer thickness, it was found that the extrapolation of the trend of IDSS for the PyC monolayer composites agreed with the data point of the multilayer composites.

In contrast, there appears no notable interlayer thickness dependency for IFS, considering the trend taken from the results of the PyC monolayer composites. However, the multilayered

interface composites with very thin (~ 20 nm) PyC layers show twice the IFS of the PyC monolayer composites. This is because the interfacial friction depends more on surface roughness rather than the thermally induced residual stress [131]. In contrast, it was reported that the effect of the surface roughness becomes very minor if the PyC interlayer thickness exceeds the maximum fiber surface roughness [132]. The maximum surface roughness of the Hi-Nicalon Type S fiber is approximately 8~15 nm [132, 133], and therefore the present data for the PyC monolayer composites were nearly equivalent. Since the multilayer composites have a very thin (20 nm) PyC layers, strong friction at the F/M interface will be anticipated. Specifically, in most cases, the main crack propagated within the first PyC interlayer, giving a more tortuous crack path, that is, increased surface roughness. The increased surface roughness eventually raised the interfacial friction significantly.

4.3.4.2 Effect of irradiation

Figure 26 shows the neutron irradiation effects on the interfacial debond shear strength (IDSS) and the interfacial friction stress (IFS) for CVI-SiC/SiC composites. At lower dose (~ 10 dpa) irradiation, both IDSS and IFS first decrease with increasing neutron dose and then approach a constant. Specifically, it is speculated that the higher temperature (~ 1100 °C) irradiation may enhance the reduction of the interfacial shear strength. This trend is quite similar to that of the proportional limit tensile stress of neutron-irradiated SiC/SiC composites, but of particular importance is that no significant degradation of the bulk strength was identified even though the reduction in interfacial strength was notable [131].

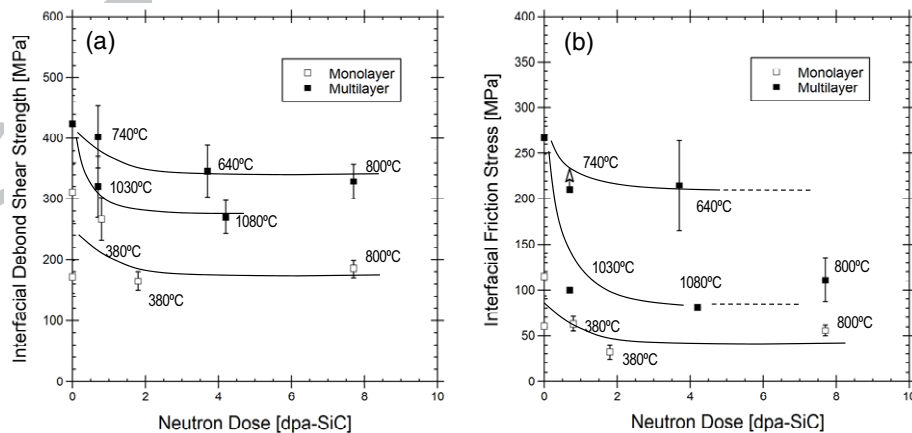


Figure 26. Neutron irradiation effects on (a) the interfacial debond shear strength and (b) the interfacial friction stress. Note that the numbers embedded in the figures show the irradiation temperatures [131].

The F/M interfacial properties depend significantly on the residual stress. The differential swelling among constituents (i.e., SiC fiber, SiC matrix, and PyC interphase) will generate a complex stress state at the F/M interface. Specifically, an irradiation-induced dimensional change of carbon, for example, well-known “turn-around” behavior, will have a greater effect than that observed for SiC, the swelling of which saturates with a few dpa. By taking swelling data of high-density isotropic carbon and high-purity CVD-SiC, the analytical results clearly show the “turn-around” behavior of the irradiation-induced residual stress [131]. This preliminary analysis includes some uncertainty in assumptions because of data scarcity such as irradiation creep, but it clearly shows good agreement with the trend of the push-out test results.

Katoh et al. claimed that a reduction in the proportional limit tensile stress by neutron irradiation does not imply a reduction in the true matrix cracking stress [68]. Alternatively it is reasonable to assume the possible irradiation-enhanced modification of the residual stress at the F/M interface to be similar to the irradiation-induced change of the interfacial shear properties. In contrast, the recent high-dose irradiation study implies probable deterioration of the Hi-Nicalon Type S fiber itself, as well as interfacial degradation by irradiation up to 70 dpa, although further investigations are necessary to support this conclusion [100].

4.3.5 Trans-plane Strength

4.3.5.1 *Inter-laminar shear strength*

Results from the present inter-laminar shear strength (ILSS) evaluation as determined by the double-notched shear test are summarized in Table 11 for the unirradiated condition. All the SA3 2D composites exhibited similar values of shear strength at 30 to 35 MPa despite the different fiber thickness, interphase coating, and different yarns. The HNLS/ML composite has a shear strength of ~23 MPa. The HNLS/PyC150 and PyC50 composites exhibited significantly lower ILSS values of ~10 MPa. All three HNLS composites evaluated were of higher-than-usual porosity, as shown in Table 2, and in particular, the HNLS/PyC150 and PyC50 suffered distinctively large inter-laminar porosity, as shown in Figure 6.

Table 11. Inter-laminar shear (or trans-plane) strength for various CVI SiC/SiC composites as determined by double-notch shear test per ASTM C1292-00. See text for explanation for anomalously low strength of the two Hi-Nicalon Type S composites.

| Material | Condition | ILSS* [MPa] | No. of valid tests |
|-----------------|-----------------|-------------|--------------------|
| SA3/PyC150-A | Unirradiated | 30.1 (3.3) | 6 |
| | 830°C, 5.9 dpa | 26.6 (6.7) | 4 |
| | 1270°C, 5.8 dpa | 30.7 (2.4) | 4 |
| SA3/PyC50-A | Unirradiated | 31.5 (4.0) | 5 |
| | 1270°C, 5.8 dpa | 27.2 (3.3) | 5 |
| SA3T/PyC150-A | Unirradiated | 33.4 (5.9) | 5 |
| HNLS/PyC150-A | Unirradiated | 10.7 (5.7) | 8 |
| | 830°C, 5.9 dpa | 11.4 (2.6) | 4 |
| | 1270°C, 5.8 dpa | 11.1 (2.3) | 4 |
| HNLS/PyC50-A | Unirradiated | 8.3 (3.8) | 5 |
| HNLS/ML-A | Unirradiated | 23.3 (5.5) | 8 |
| SA3-P120/PyC150 | Unirradiated | 24.8 (3.5) | 6 |

*Inter-laminar shear strength or trans-plane shear strength (Numbers in parentheses denote standard deviations.)

ILSS of CVI SiC/SiC reinforced with either UD HNLS or UD SA3 fiber, with various coatings, has been evaluated [113] by the same method. The results showed that there was no significant difference among the shear strength values between the two fiber grades or among different interphase coatings with the measured ILSS values over the range of 54 to 63 MPa. This report suggests that the variation in ILSS observed in the present study is due primarily to the porosity effect. The significantly higher ILSS for the UD composites likely reflects the lack of large inter-laminar pores in the uni-directional architecture.

It is known that the ILSS of 2D SiC/SiC may be affected by the interphase thickness. Lara-Curzio has demonstrated that the ILSS of a CG-Nicalon reinforced CVI-SiC matrix composite significantly decreases when the interphase PyC thickness is increased from 0.3 μm to 1.1 μm [134]. This trend is explained by the observation that when a critical thickness is reached, the interphase itself becomes the weakest link replacing the matrix pores. In this study, the ILSS is not affected by PyC coating thicknesses of 150 or 50 nm for either fiber grade, suggesting that the critical interphase thickness is greater than 150 nm.

Detailed fracture surface examination revealed that failure occurs when cracks connect large inter-laminar pores of high-porosity composites, whereas the cracks propagate through (and/or originate within) the transverse fiber tows in low-porosity composites. Therefore, the ILSS for these materials with adequate matrix densification is anticipated to be in the 30 to 35 MPa range. These values appear comparable with the ILSS of 36 ± 6 MPa reported for high-density melt-infiltrated SiC/SiC composites in 2D architecture [135]. Because of the crack propagation path that is through the fabric planes in the adequately matrix-densified composites, the term trans-plane shear strength may be more appropriate than the commonly used ILSS.

The Hybrid 3D composite exhibited an ILSS of ~ 25 MPa, which is slightly lower than that exhibited by the SA3 2D composites, despite the presence of trans-thickness graphite fibers. This low ILSS measured for the hybrid 3D composite may be attributed to the extensive matrix cracking introduced by the thermal expansion mismatch between the SiC matrix and the graphite fibers.

There is no statistically significant change in the ILSS following neutron irradiation up to a fluence of 5.9 dpa at temperatures up to 1270°C for all the materials studied, as shown in Table 11. Even though the interphase properties presumably degrade at this fluence and temperature [63, 131], the apparent inter-laminar shear strength of the composites is retained. This result supports the observation that the trans-laminar shear failure is determined by the crack propagation from the pore surfaces or fiber tows through the intact matrix.

4.3.5.2 Trans-thickness tensile strength

As described in Section **Error! Reference source not found.**, the trans-thickness tensile strength (TTS) was determined by the diametral compression of truncated disc specimens. In this test method, historically, the calculated tensile stress at the center of the specimens at the apparent failure in the load-displacement record has been used as the nominal TTS for the test specimens. However, the first cracking as detected by a pair of strain gauges attached to both flat faces of the test specimen was found to be significantly lower than the stress at the apparent failure [136]. Therefore, in Table 12, the stress at the first cracking is shown to better represent the true TTS, while the stress at apparent failure is also presented for comparison with the previous data. The current result shows the TTS of 20–25 MPa and the apparent failure stress of 30–35 MPa for the SA3/PyC150 composite, regardless of the neutron irradiation. The CV's appear comparable with those for the in-plane tensile PLS.

Table 12. Trans-thickness tensile strength for near-stoichiometric SiC fiber CVI SiC matrix composites in 2D architectures as determined by diametral compression test.

| Material | Irradiation condition | First cracking stress ¹ [MPa] | | Failure stress ² [MPa] | |
|------------|-----------------------|--|----------------------|-----------------------------------|------------|
| | | Average | (S.D. ³) | # ⁴ | Average |
| SA3/PyC150 | Unirradiated | 23.9 | (5.4) | 3 | 34.1 (3.2) |
| | 830°C, 5.9 dpa | 25.4 | (11.3) | 3 | 34.8 (6.2) |
| | 1270°C, 5.8 dpa | 20.5 | (0.9) | 4 | 29.7 (2.8) |

1: Considered to correspond with straight trans-thickness tensile strength; 2: shown to allow comparison with historical data; 3: standard deviation; 4: number of valid tests

2D SiC/SiC composites with CVI SiC matrices were tested in a similar manner by Hinoki et al. [82]. The reported TTS values, 25 – 31 MPa for the SA3 fiber composite and 18 – 27 MPa for the HNLS fiber composite, appear consistent with the present results of the apparent failure stress. They also reported the negative correlation between the TTS and the porosity and the insensitivity of porosity-normalized TTS to the interphase thickness up to ~500 nm. The fracture surface presented in Figure 27 exposes the interior of the fiber tows, indicating that the major cracks are propagating through and/or initiating from inside the fiber tows [137]. This observation, along with the negative porosity-TTS correlation, indicates the importance of the matrix surrounding the fiber tows in determining the TTS.



Figure 27. Typical fracture surface of SA3/PyC150 specimens after diametral compression trans-thickness tensile test. The inset shows extensive fiber breakage after the intra-tow failure.

Moreover, Hinoki et al. studied the TTS for UD SiC/SiC composites by both the diametral disc compression method and the straight tensile test using adhesive bond per ASTM C1468 [113]. The strength values obtained were 26.9 MPa and 20.2 MPa for the straight TTS of HNLS and SA3 composites, respectively, and 23.8 MPa for the diametral compression TTS of the same SA3 composite, showing a good agreement between results from the two test methods. The fact that the UD composites exhibited significantly higher ILSS than the similar 2D composites while the TTS appeared similar for UD and 2D composites implies the key role of the transverse fiber tows in the trans-plane shear failure of the 2D composites.

Table 12 also summarizes the TTS properties of the SA3/PyC150 after neutron irradiation. The results show a negligible effect of irradiation at 800°C and only a very slight effect (if at all) at 1270°C. This observation supports previous findings that the TTS is determined primarily by the matrix, which is insensitive to irradiation in terms of strength or toughness.

Overall, it is conceivable that the trans-plane strength properties of the 2D composites are determined by the intrinsic toughness of the CVI SiC matrix and the morphological features and porosity of the matrix, as determined by the fabric architecture, lay-up scheme, and the degree of densification. Large interlaminar and/or mesh pores may act as the fracture origin. However, the fiber tows incorporating a network of the low-strength carbon interphase may also act as flaws in the matrix continuum.

4.3.6 Damage Tolerance

The damage tolerance properties of CVI SiC-matrix composites and the toughening mechanism of composites by fiber bridging (i.e., rising R-curve behavior) have been summarized in Refs. [86] and [138], respectively. According to these references, two basic approaches are mainly adopted for the analysis of experimental results: (a) extended linear elastic fracture mechanics (LEFM) and (b) energy-based non-linear fracture mechanics. In either case, two issues must always be considered: (1) to what extent the LEFM is applicable to the complex failure behavior of composites and (2) whether “effective” crack length by the compliance method, which is based on the LEFM and inherently for homogeneous materials, can be representative of actual crack length. Additionally, for the irradiation study, issues associated with the use of small specimens need to be addressed.

As the practical procedure to estimate the reasonable damage tolerance of ceramic matrix composites, Nozawa et al. proposed a model of the composite damage progression [84, 139]. This model relies on analytical models of non-linear fracture mechanics [84, 140, 141] using global energy balance, making it suitable for the nuclear-grade SiC/SiC composites that exhibit

quasi-ductile failure. Quantification of damage tolerance was defined as fracture resistance G (kJ/m^2) contributed by macro-crack formation energy instead of K_{Ic} . For evaluating the crack length, microscopic observation by replica films at each damage state was chosen. The results of Mode I damage tolerance tests conducted are given below.

Technical detailed procedures and the results of the damage tolerance evaluation in the current experiment are summarized and published elsewhere by Ozawa et al.[142, 143] As the typical load-crack opening displacement (COD) evolutions during the SENB damage tolerance tests are shown in Figure 28, the HNLS composites in unirradiated and irradiated conditions exhibited the typical quasi-ductile fracture behavior. Microscopy examination of the replica films taken intermittently from the SENB specimens revealed the three distinct stages in the fracture process: (i) microcracking-enabled deformation around the notch tip without macro-cracking, (ii) initiation and linear extension of a macro-crack, and (iii) macro-crack branching and progressive failure of the bridging fibers.

In the HNLS/PyC150-A and HNLS/PyC50-A composite curves, the hysteresis loops of load-COD unloading/reloading sequences did not close at the end of the tests. The replica film observation revealed that compressive failure had occurred at a support pin due to the relatively high porosity, and the cracks originated there propagated with increasing displacement toward the end of the tests. Moreover, the SA3 composites exhibited the significantly less quasi-ductile behavior, contributed by the higher interfacial strength. The very rapid crack propagation across the specimens prohibited detailed analysis of the progressive damage evolution. Particularly, the SA3T/PyC150-A composites failed in a brittle manner, whereas the other SA3 composites did not.

Analyzing the load-COD behavior based on the model [84] in conjunction with the crack replica examination, one can estimate the breakdowns of the work during a SENB test into elastic energy, frictional energy dissipation at the interfaces, residual strain energy, and macro- and micro-crack surface formation energy. From this analysis, as listed in Table 13, apparent fracture resistance as a sum of macro- and micro-crack surface formation energy was obtained to be $\sim 3.4 \text{ kJ/m}^2$ for the unirradiated HNLS/ML-A composite. With the energy release rate contribution from micro-cracking estimated to be on the order of $\sim 0.34 \text{ kJ/m}^2$, the fracture resistance for macro-cracking is estimated to be $\sim 3 \text{ kJ/m}^2$. Significant scatters in energy release rate of the composites are likely attributed to the limited specimen size (the ligament length of 2 mm with 4 mm width) as compared to the weave unit cell size ($\sim 2\text{--}2.5 \text{ mm square}$).

As shown in Figure 28, no significant changes in various features of the load-COD curves such as peak load and hysteresis loop width were observed for either composite type following neutron irradiation. For the HNLS/ML-A composite, no remarkable change in crack length development was observed after neutron irradiation; hence, no obvious effects of neutron

irradiation on damage tolerance were estimated from the current model analytical result: $3.5 \pm 2.3 \text{ kJ/m}^2$ irradiated at 830°C to 5.9 dpa and $4.0 \pm 1.8 \text{ kJ/m}^2$ at 1270°C to 5.8 dpa. However, taking into consideration for the tensile test results reported above, the analysis of the hysteresis loop using the unloading/reloading tensile curves for interfacial property estimation and this energy release rate analysis based on non-linear fracture mechanics [143], it is reasonable to conclude that the effects of neutron irradiation in the current conditions on the damage tolerance of these composites are insignificant.

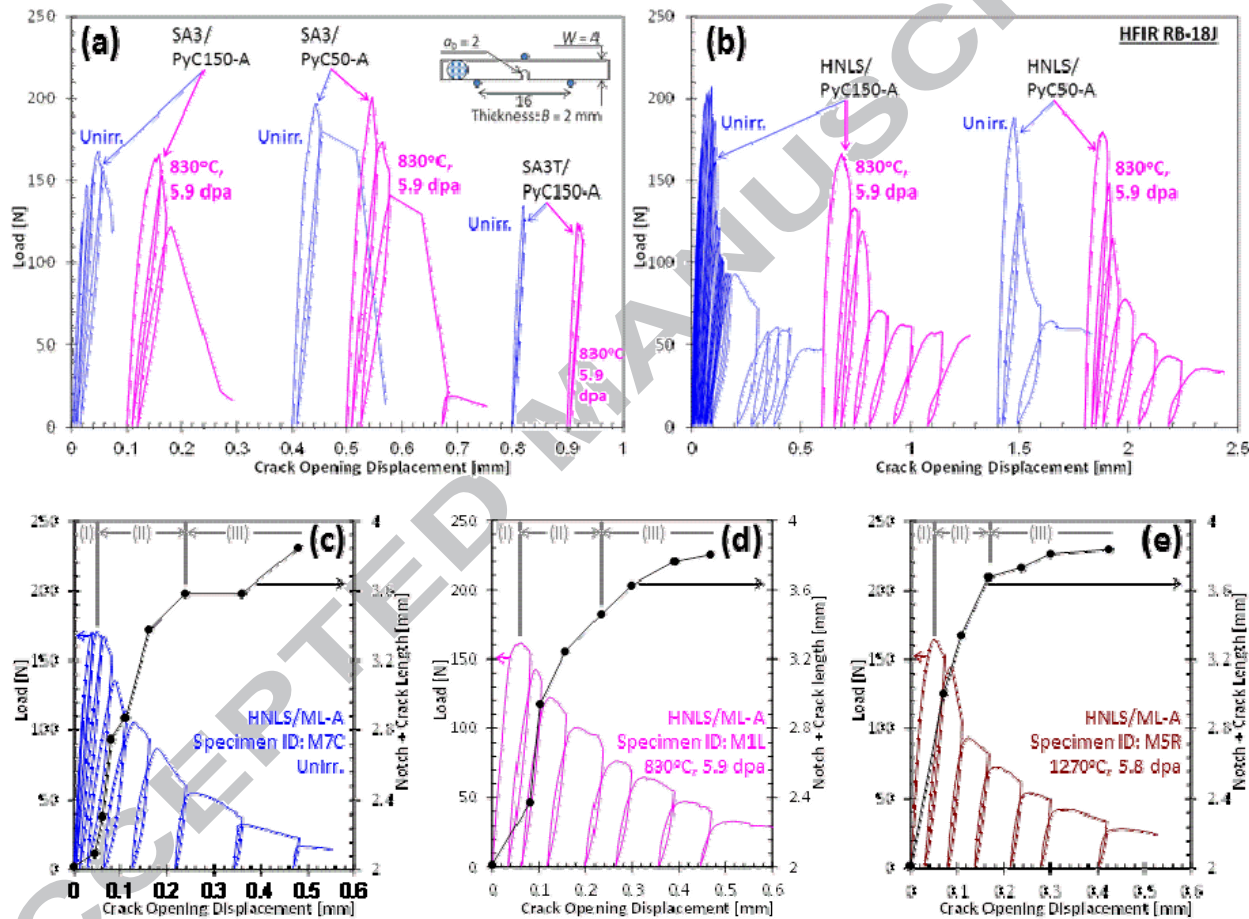


Figure 28. Crack-extension behavior of 2D CVI SiC/SiC composites as evaluated using single-edge notched beam specimens in unirradiated and irradiated conditions [142, 143]. Load – crack opening displacement (COD) curves in (a) and (b) are horizontally offset for visibility.

Table 13. Experimental data for damage tolerance properties of the 2D CVI SiC/SiC composites in unirradiated and neutron-irradiated conditions [143]. Numbers in parenthesis denote one standard deviation.

| Material | Irradiation Condition | G_{total} [kJ/m ²] | G_{micro} [kJ/m ²] | G_{macro} [kJ/m ²] | No. of Tests | Ref. |
|-----------|-----------------------|-------------------------------------|-------------------------------------|-------------------------------------|--------------|-------------|
| HNLS/ML-A | unirradiated | 3.41 (2.01) | 0.34 (0.09) | 3.08 (2.10) | 3 | Ozawa, 2011 |
| | 830°C, 5.9 dpa | 3.48 (2.34) | 0.44 (0.05) | 3.04 (2.29) | 2 | Ozawa, 2011 |
| | 1270°C, 5.8 dpa | 4.00 (1.81) | 0.37 (0.10) | 3.63 (1.91) | 2 | Ozawa, 2011 |

G_{total} , G_{micro} , and G_{macro} denote the energy release rate contributed both from macro- and micro-crack, only from micro-cracks, and only from the macro-crack, respectively; i.e., $G_{macro} = G_{total} - G_{micro}$ is an apparent fracture resistance of a composite.

4.3.7 Life Prediction and Time-Related Failure

Nuclear-grade SiC/SiC composites have a robust microstructure with regards to time-related thermal stability. All current nuclear-grade SiC/SiC composites exhibit an inherent stability, without consideration of irradiative effects, at temperatures up to 1400°C, while stability can be as high as 1800°C for some types of nuclear-grade SiC/SiC [144-146]. This stability is primarily limited by grain growth in the fibers and an associated time-related decrease in the properties as the grains coarsen with time. The grain coarsening results in both a decrease in fiber strength and an increase in fiber roughness that is detrimental to obtaining tough composite behavior. This inherent, non-irradiated stability is beyond the requirements of currently conceived nuclear applications; thus, the usable life of these materials will most typically be determined by the stress state and environmental effects. Of these, the most significant environmental factors are the presence of oxidizing species (O₂, H₂O, CO₂, etc.) and/or stress combined with elevated temperatures. Life prediction is highly dependent on service conditions. The estimates of capabilities of SiC/SiC composites in the following discussion attempt to utilize what are believed to be conservative estimates for the operating conditions of a high-temperature gas-cooled reactor. These estimates have been made to demonstrate viability and must be considered as estimates of a likely suitable life envelope, but significant testing is required to verify these preliminary estimates.

An overview of life-limiting mechanisms is best started by considering the effect of stress and temperature independent of other environmental effects. Creep of SiC fibers has been well studied [147, 148]. With regards to commercially available nuclear-grade SiC fibers, Hi-Nicalon Type S has superior creep resistance as compared to Tyranno SA3. However, creep in CVD SiC [149] is only measurable, $>1 \times 10^{-9} \text{ s}^{-1}$, along the preferred {111} slip plane at temperatures up to 1750°C, and an unoriented CVI SiC matrix is likely more creep resistant than either fiber, and undoubtedly more creep resistant at temperatures in excess of 1350°C. The creep rate for NITE

matrix material can reasonably be assumed to be similar to that of Tyranno SA3 fiber due to the presence of similar sintering aids. The controlling mechanism for steady-state creep deformation of all these forms of SiC is diffusional controlled grain boundary sliding with different limiting diffusional pathways [147, 149]. The relative creep rates based on extrapolation to lower temperatures relevant to HTGR's are shown in Figure 29. In general, the creep rates for all the SiC constituent materials are low. This extrapolation to temperatures relevant to HTGR's presumes that there is no mechanism change at the lower temperatures, and provides an initial estimate that the SiC materials are no better than this limit. Based upon the fiber data in Figure 29, a stress-temperature envelope can be defined at different times. The conservative case is that the SiC/SiC components would be "life of the reactor" components with an expected service life of up to 60 years. A common normal reactor operating temperature for planned HTGR's that would incorporate SiC/SiC composites is 900–950°C [150]. The ASME Boiler Code [151] provides one means to calculate equivalent hours normalized to maximum service temperature. Equation 10 shows the sum of the different operating times after normalization to the maximum operating temperature as normalized using Equation 11.

$$t_{equiv} = \sum_{i=1}^n (t_{equiv})_i \quad (10)$$

$$\log_{10}(t_{equiv})_i = (10 + \log_{10}(t_i)) \left(\frac{T_i}{T_{max}} \right) - 10 \quad (11)$$

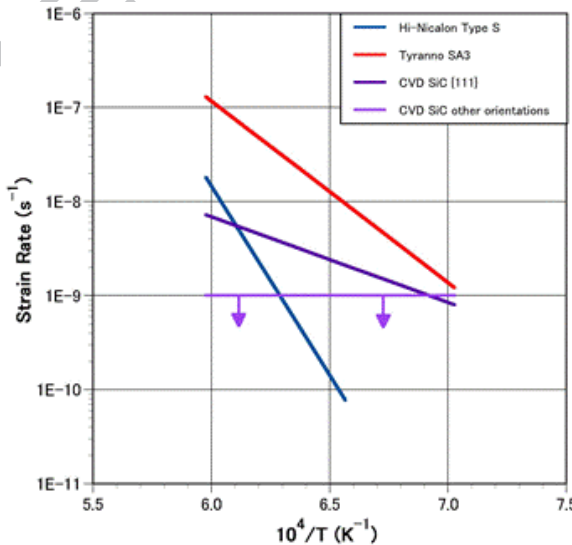


Figure 29. Extrapolated creep rates for nuclear-grade SiC/SiC constituents showing that Tyranno SA3 is most susceptible to creep deformation, and that Hi-Nicalon Type S may or may not be more creep resistant than CVD SiC based on temperature and the resolution of the non-{111} orientations.

Thus a plot of stress versus maximum service temperature can be calculated for the intrinsic creep limitation of the composites. This plot is shown in Figure 30 as a function of maximum operating temperature for a normal service temperature of 950°C and a duration of 60 years. The higher creep resistance of Hi-Nicalon Type S is evident; however, both fibers are capable of at least 69 MPa with a maximum service temperature of 1200°C. Maximum composite stress was calculated assuming a 0.5% creep strain limit and a nominal 36% fiber volume in a 0°/90° 2D laminate, with the additional assumption that the entire load is carried by the fibers in the stressed direction, that is, the matrix is not carrying load. This assumption is made as the matrix material may become cracked during service and thus is assumed have occurred at $t = 0$. In addition to unintended loadings and slow crack growth that may result in matrix cracking, stress redistribution during creep occurs with the more creep-resistant phase increasing load as a function of time. For a CVI SiC matrix SiC/SiC composite, the matrix stress will increase with time and will result in matrix cracking unless the initially applied stress is below a threshold stress such that when the asymptotic load in the fiber is achieved, the matrix is below its cracking strength. Models for determining the stress distribution in a composite have been developed to aid in determining this stress [152].

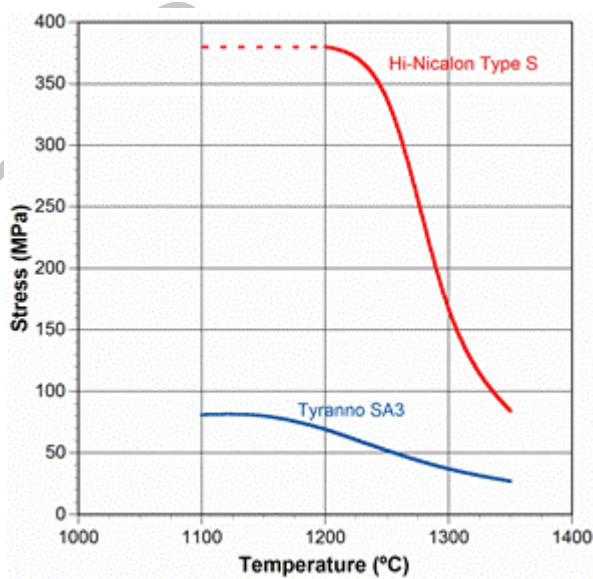


Figure 30. Estimated stress temperature limit for nuclear-grade SiC fibers for an HTGR application involving a 60-year service life and 500-hour maximum temperature event with the only limitation being the creep of the fibers.

An understanding of the time-dependent behavior of the composites in the environment of an HTGR is also needed. In particular, the effects of small oxidizing partial pressures must be considered due to the high flow rates of coolant gas. In the case of a SiC/SiC with an uncracked matrix, the effect of the oxidizing species is purely on the matrix and will generate a passivating oxide at conditions below the passive/active oxidation threshold for SiC. In this regime, the effect of the environment is limited to possible enhancement of subcritical crack growth due to the time-related formation of the oxide flaw population. Active oxidation rate of the matrix is highly operational condition dependent and is not of concern at temperatures below 1250°C if the partial pressure of oxygen is 1 Pa or more [153, 154]. However returning to the assumption that the matrix may crack, composite degradation can occur due to oxidation embrittlement that bonds the matrix strongly to the fibers, interfacial removal and decoupling of the fibers that reduces load transfer in addition to the creep-related life-limiting mechanism [155]. The effect of environmental degradation on the reinforcing fiber and the change in fiber properties must also be considered. In particular, SiC fibers have been demonstrated to be susceptible to environmentally assisted slow crack growth [156, 157]. Gauthier et al. showed that at moderate temperatures of 500–800°C in air that the life of SiC fibers can be substantially reduced by the slow crack propagation of surface defects resulting from the consumption of carbon at the grain boundaries and by stresses induced from the oxidation of silicon carbide at the crack tip. This reduction can be catastrophic in that the time to failure for Hi-Nicalon Type S can be reduced to less than 1 week at 800°C. Tyranno SA3 was found to be more resistant to this environmental degradation, but still experienced a severe reduction in life. Gauthier et al. found that the data followed a power law relation of the form shown in Equation 12.

$$t\sigma^n = A_0 \exp\left(\frac{-Q}{RT}\right). \quad (12)$$

The A_0 term can be modified to include the pressure dependence and the order of the reaction as shown in Equation 12 to consider the effect of lower partial pressures of oxygen.

$$A_0 = A p_{O_2}^m. \quad (13)$$

Hi-Nicalon Type S/CVI SiC composites with a thin pyrolytic carbon fiber coating were tested in stress rupture in air and at reduced oxygen partial pressures after pre-cracking the matrix by straining to 0.05%. Figure 31 shows that the oxygen partial pressure dependence can be divided into two regimes. At high stress levels and lower temperatures, the pressure dependence was found to be nominally 1.0. In contrast, lower pressure sensitivity was identified at low stress levels and higher temperatures, where a reaction order of 0.3 was measured. It was not possible to force failure of the composites at low stress levels and lower temperatures combined with low oxygen partial pressures within a 500 hour experimental test

time. Thus a conservative estimate on the order of a pressure dependence of 0.3 was assumed for estimating life behavior at lower oxygen partial pressures where failures did not occur within the experimental test time. Two sets of stress rupture data were accumulated at P_{O_2} of 20 kPa and 100 Pa. This data was reduced to a single time/temperature parameter using Larson-Miller criteria of

$$LMP = T(\log_{10}(t) + 22), \quad (14)$$

where T is the absolute temperature, and t is the stress rupture life in hours. Figure 32 shows this data along with an extrapolated behavior to 2 Pa oxidizing partial pressure expected in an HTGR. Application of this Larson-Miller plot at 2 Pa must be restricted at least by conditions where active oxidation is not dominant, <1250°C. Utilizing the same equivalent hours method of Equations 10 and 11, the LMP value required would be 37719 to meet the HTGR service conditions of 950°C for 60 years with maximum operating temperature of 1250°C for 500 hours. The stress level estimated to correspond to this at 2 Pa oxidizing pressure is 480 MPa fiber stress, which conservatively assuming that the cracked matrix carries no load would correspond to a composite stress of 86 MPa for a 36% fiber volume 0°/90° Hi-Nicalon Type S/CVI SiC composite. Thus the introduction of the environment is significantly expected to reduce the load-carrying capacity of Hi-Nicalon Type S as compared to creep limitation.

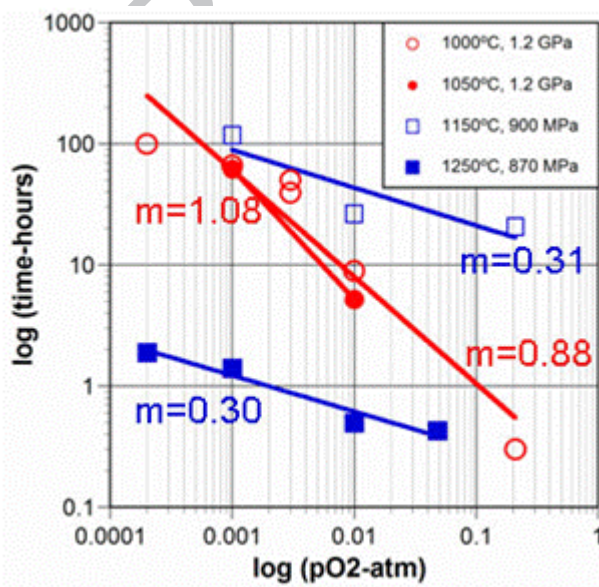


Figure 31. Stress rupture dependence on oxygen partial pressure of Hi-Nicalon Type S/CVI SiC with pre-cracked matrix showing two regimes $m = \sim 1$ at lower temperatures and high stress levels and $m = \sim 0.3$ at higher temperatures and lower stress levels.

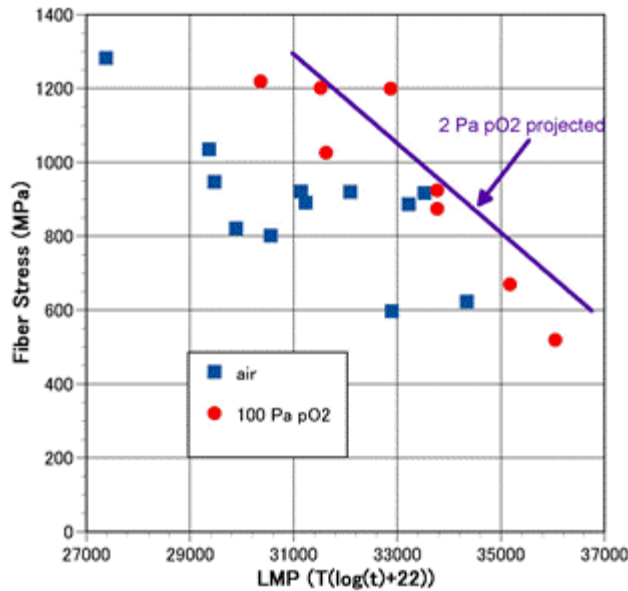


Figure 32. Larson Miller plot of Hi-Nicalon Type S/CVI SiC with a pre-cracked CVI SiC matrix showing the effect of oxygen partial pressure and a projection to 2 Pa based on a $p_{O_2}^{0.3}$ dependence.

Thus, for the example case of an HTGR with a 60-year life and a normal reactor temperature of 950°C, a 36% fiber volume, 0°/90° fabric-based nuclear-grade Hi-Nicalon Type S/CVI SiC composite can meet the requirements under a low oxidizing partial pressure with maximum temperature event(s) of not more than 1250°C and a 90 MPa maximum stress level, and at one estimate [158] of 1150°C for maximum material temperature, a maximum stress level of 110 MPa is acceptable. For comparison, a Tyranno SA3/ CVI SiC composite would be limited by at least creep to a 52 MPa stress level. For design, these stress levels would be subject to either a statistical variance, based on the lowest measured data point, or other material property factor of safety.

5 Summary and Conclusions

The primary purpose of this work was to provide a summary compilation of properties for continuous near-stoichiometric SiC fiber-reinforced, CVI SiC-matrix composites in as-fabricated and neutron-irradiated conditions. Included in this compilation was significant new work on the properties of such materials neutron-irradiated at elevated temperatures. Typical properties of composites with the 2D 0°/90° layup architecture are summarized in Table 14.

It is worth noting that the baseline properties for nuclear-grade SiC/SiC composites are reasonably reproducible and the statistical data indicate small scatters in strength, particularly the in-plane tensile strength. The effects of neutron irradiation summarized in this work are minimal with an exception of thermal conductivity change. This favors the design and safety analysis of nuclear components constructed from these materials.

Table 14. Summary to typical properties for nuclear-grade CVI SiC/SiC composites in flat, orthotropic, 2D lay-up architectures.

| Property | Unirradiated | Neutron-Irradiated |
|--|--|--|
| Density / Fiber Volume Fraction / Swelling | 2.5 – 2.7 g/cm ³ at RT for most materials. 15 – 20% porosity. 35 – 40% fiber volume fraction. | Swelling in a very similar manner to CVD SiC (Figs. 7 and 8, Equations 3 and 4). |
| Thermal Expansivity (CTE) | Same with CVD SiC (Fig. 8). | Very minor effect of irradiation (Fig. 9) (apparent CTE changes as defect anneals at T > T _{irr}) |
| Specific Heat (C _p) | Very similar with CVD SiC. | No change assumed by irradiation (apparent C _p may change as defect anneals at T > T _{irr}) |
| Thermal Diffusivity (a) / Conductivity (K) | At RT, K = 8 – 15 W/m-K for HNLS and 15 – 24 W/m-K for SA3 composites. For T>RT, d(1/a)/dT = 0.02±0.005 s/cm ² -K | Eq. 6 and Fig. 12. See discussion in Section 4.2.2.2. |
| Electrical Conductivity | Highly tailorable (see Section 4.2.3.1). Typically 5 – 20 S/m through-thickness and 100 – 500 S/m in-plane at RT < T < ~800°C | Irradiation effect not very significant. |
| Young's Modulus | 200 – 280 GPa at RT (in-plane). | Minor decrease; $\Delta E/E_0 = -(swelling) / 3 \times \sim 10$ |
| Poisson's Ratio | ~0.13 for 0°/90°, ~0.25 for ±45° (in plane). | No significant change anticipated. |
| Proportional Limit Stress (in-plane) | Mostly 90 – 120 MPa. | No significant irradiation effect. |
| Ultimate Tensile Strength (in-plane) | 250 – 350 MPa for 0°/90°. Significant orientation dependence. | No significant irradiation effect. |
| Statistical Strength (in-plane) | For PLS, CV = 0.15 – 0.2, Weibull modulus 6 – 8. For UTS, CV = ~0.1. | No significant irradiation effect. |
| Trans-laminar Shear Strength | 25 – 35 MPa. | No significant irradiation effect. |
| Trans-thickness Tensile Strength | 20 – 25 MPa. | No significant irradiation effect. |
| Damage Tolerance | Macro-crack propagation resistance estimated to be ~3 kJ/m ² . | No significant irradiation effect. |
| Time-dependent Failure | Larson-Miller approach is proposed. See discussion in Section Error! Reference source not found. | Not sufficiently studied. |

Acknowledgment

This work was supported by Office of Fusion Energy Sciences and Office of Nuclear Energy, U.S. Department of Energy under contract DE-C05-00OR22725 with UT-Battelle, LLC, and U.S.-Japan TITAN Collaboration on Fusion Blanket Technology and Materials. Research supported in part by ORNL's Shared Research Equipment (ShaRE) User Facility and High Flux Isotope Reactor, which are sponsored by the Office of Basic Energy Sciences, U.S. Department of Energy. The authors are thankful to J. Hemrick for providing a technical review of the manuscript, G. Youngblood for providing the HNLS/PyC150-B test specimens, W. Porter for generating the thermo-physical properties data, and D. Stevens for an editorial review.

This manuscript has been authored by the Oak Ridge National Laboratory, managed by UT-Battelle LLC under Contract No. DE-AC05-00OR22725 with the US Department of Energy. The US Government retains and the publisher, by accepting the article for publication, acknowledges that the US Government retains a nonexclusive, paid-up, irrevocable, worldwide license to publish or reproduce the published form of this manuscript, or allow others to do so, for US Government purposes.

References

- [1] L.L. Snead, T. Nozawa, M. Ferraris, Y. Katoh, R. Shinavski, M. Sawan, Silicon carbide composites as fusion power reactor structural materials J. Nucl. Mater., 417 (2011) 330-339.
- [2] L. Giancarli, H. Golfier, S. Nishio, A.R. Raffray, C.P.C. Wong, R. Yamada, Progress in blanket designs using SiCf/SiC composites, Fusion Eng. Design, 61-62 (2002) 307-318.
- [3] Y. Katoh, L.L. Snead, I. Szlufarska, W.J. Weber, Radiation Effects in SiC for Nuclear Structural Applications, Current Opinion in Solid State & Materials Science, 16 (2012) 143-152.
- [4] L.L. Snead, Y. Katoh, T. Nozawa, Radiation Effects in SiC and SiC-SiC, in: R.J.M. Konings (Ed.) Comprehensive Nuclear Materials, Elsevier, Amsterdam, 2012, pp. 215-240.
- [5] R. Naslain, Design, preparation and properties of non-oxide CMCs for application in engines and nuclear reactors: an overview, Composites Science and Technology, 64 (2004) 155-170.
- [6] K. Yueh, D. Carpenter, H. Feinroth, Clad in Clay, Nuclear Engineering International, (2010) 14-16.
- [7] K.E. Barrett, M.P. Teague, I. van Rooyen, S. Bragg-Sitton, K. Ellis, C. Glass, G. Roth, K. McHugh, J. Garnier, G. Griffith, M.C. Teague, G. Bell, L.L. Snead, Y. Katoh, Engineering Challenges of LWR Advanced Fuel Cladding Technology in Preparation for In-Reactor Demonstration, Trans. Ameri. Nucl. Soc., (2012).
- [8] S. Fazluddin, K. Smit, J. Slabber, The use of advanced materials in VHTR's, in: 2nd International Topical Meeting on High Temperature Reactor Technology, Beijing, 2004, pp. E06.
- [9] L.L. Snead, Y. Katoh, W. Windes, K. Smit, Candidate structural materials for in-core VHTR application, Trans. Ameri. Nucl. Soc., 98 (2008) 1019-1020.
- [10] C.W. Forsberg, P.F. Peterson, R.A. Kochendarfer, Design options for the advanced high-temperature reactor, in: International Conference on Advances in Nuclear Power Plants, ICAPP 2008, 2008, pp. 733-749.
- [11] A. Kohyama, T. Hinoki, T. Mizuno, T. Kunugi, M. Sato, Y. Katoh, J.S. Park, R&D of advanced material systems for reactor core component of gas cooled fast reactor, in: Proceedings of 2005 International Congress on Advances in Nuclear Power Plants (ICAPP-05), 2005.
- [12] L. Charpentier, K. Dawi, M. Balat-Pichelin, E. Beche, F. Audubert, Chemical degradation of SiC/SiC composite for the cladding of gas-cooled fast reactor in case of severe accident scenarios, Corrosion Science, 59 (2012) 127-135.
- [13] A.R. Raffray, R. Jones, G. Aiello, M. Billone, L. Giancarli, H. Golfier, A. Hasegawa, Y. Katoh, A. Kohyama, S. Nishio, B. Riccardi, M.S. Tillack, Design and material issues for high performance SiCf/SiC-based fusion power cores, Fusion Eng. Design, 55 (2001) 55-95.
- [14] N.B. Morley, Y. Katoh, S. Malang, B.A. Pint, A.R. Raffray, S. Sharafat, S. Smolentsev, G.E. Youngblood, Recent US research and development for the dual coolant blanket concept, Fusion Eng. Design, 83 (2008) 920-927.
- [15] R.J. Price, Effects of fast-neutron irradiation on pyrolytic silicon carbide, J. Nucl. Mater., 33 (1969) 17-22.

- [16] R.J. Price, Properties of silicon carbide for nuclear fuel particle coatings, *Nucl. Tech.*, 35 (1977) 320-336.
- [17] L.L. Snead, T. Nozawa, Y. Katoh, T.S. Byun, S. Kondo, D.A. Petti, Handbook on SiC Properties for Fuel Performance Modeling, *J. Nucl. Mater.*, 371 (2007) 329-377.
- [18] Y. Pramono, M. Imai, T. Yano, Helium release and physical property change of neutron-irradiated a-SiC containing B4C of different 10B concentrations, *J. Nucl. Sci. Tech.*, 40 (2003) 531-536.
- [19] T.D. Burchell, Fission Reactor Applications of Carbon, in: T.D. Burchell (Ed.) *Carbon Materials for Advanced Technologies*, Elsevier Science Ltd, Oxford, 1999, pp. 429-484.
- [20] B.T. Kelly, The behavior of graphite under neutron irradiation, *Journal of Vacuum Science and Technology, A* 4 (1986) 1171-1178.
- [21] B.T. Kelly, Irradiation behavior of fine-grain graphites, *Fusion Technology*, 16 (1989) 96-103.
- [22] Y.S. Virgil'ev, I.G. Lebedev, Effect of neutron irradiation on properties of glassy carbon, *Inorganic Materials*, 38 (2002) 668-673.
- [23] S. Yajima, J. Hayashi, Development of a silicon carbide fibre with high tensile strength, *Nature*, 261 (1976) 683-685.
- [24] H. Ichikawa, Development of high performance SiC fibers derived from polycarbosilane using electron beam irradiation curing-a review, *Journal of the Ceramic Society of Japan*, 114 (2006) 455-460.
- [25] L.L. Snead, M.C. Osborne, K.L. More, Effects of radiation on SiC-based Nicalon fibers, *Journal of Materials Research*, 10 (1995) 736-747.
- [26] L.L. Snead, E. Lara-Curcio, Interphase integrity of neutron irradiated SiC composites, *Materials Research Society Symposium Proceedings*, 540 (1999) 273-278.
- [27] G.W. Hollenberg, C.H. Henager Jr., G.E. Youngblood, D.J. Trimble, S.A. Simonson, G.A. Newsome, E. Lewis, The effect of irradiation on the stability and properties of monolithic silicon carbide and SiCf/SiC composites up to 25 dpa, *J. Nucl. Mater.*, 219 (1995) 70-86.
- [28] A.R. Bunsell, A. Piant, A review of the development of three generations of small diameter silicon carbide fibres, *Journal of Materials Science*, 41 (2006) 823-839.
- [29] M. Takeda, A. Saeki, J. Sakamoto, Y. Imai, H. Ichikawa, Effect of hydrogen atmosphere on pyrolysis of cured polycarbosilane fibers, *J. Ameri. Ceram. Soc.*, 83 (2000) 1063-1069.
- [30] T. Tanaka, S. Shibayama, M. Takeda, A. Yokoyama, Recent progress of Hi-Nicalon Type S development, *Ceram. Eng. Sci. Proc.*, 24 (2003) 217-223.
- [31] T. Ishikawa, Y. Kohtoku, K. Kumagawa, T. Yamamura, T. Nagasawa, High-strength alkali-resistant sintered SiC fibre stable to 2,200°C, *Nature*, 391 (1998) 773-775.
- [32] H.M. Yun, J.A. DiCarlo, Thermostructural Properties of Stoichiometric SiC Fibers, in: R.H. Jones, A. Kohyama (Eds.) *The Third International Energy Agency Workshop on SiC/SiC Ceramic Composites for Fusion Structural Applications*, Cocoa Beach, Florida, 1999, pp. 37-52.
- [33] A. Kohyama, J.S. Park, H.C. Jung, Advanced SiC fibers and SiC/SiC composites toward industrialization, *J. Nucl. Mater.*, 417 (2011) 340-343.
- [34] J.B. Davis, R.S. Hay, D.B. Marshall, P.E.D. Morgan, A. Sayir, Influence of interfacial roughness on fiber sliding in oxide composites with La-monazite interphases, *J. Ameri. Ceram. Soc.*, 86 (2003) 305-316.
- [35] C. Sauder, A. Brusson, J. Lamon, INFLUENCE OF INTERFACE CHARACTERISTICS ON THE MECHANICAL PROPERTIES OF Hi-NICALONS AND SA3 FIBER REINFORCED

- SiC/SiC MINICOMPOSITES, International Journal of Applied Ceramic Technology, 7 (2010) 291-303.
- [36] L.L. Snead, Y. Katoh, A. Kohyama, J.L. Bailey, N.L. Vaughn, R.A. Lowden, Evaluation of neutron irradiated near-stoichiometric silicon carbide fiber composites, *J. Nucl. Mater.*, 283 (2000) 551-555.
- [37] Y. Katoh, A. Kohyama, L.L. Snead, T. Hinoki, A. Hasegawa, Neutron Tolerance of Advanced SiC-Fiber / CVI-SiC Composites, in: 19th IAEA Fusion Energy Conference, 2002, pp. FT/P1-03.
- [38] T. Hinoki, L.L. Snead, Y. Katoh, A. Hasegawa, T. Nozawa, A. Kohyama, The effect of high dose/high temperature irradiation on high purity fibers and their silicon carbide composites, *J. Nucl. Mater.*, 307 (2002) 1157-1162.
- [39] C. Droillard, J. Lamon, Fracture toughness of 2D woven SiC/SiC CVI-composites with multilayered interphases, *J. Ameri. Ceram. Soc.*, 79 (1996) 849-858.
- [40] R. Naslain, R. Pailler, J. Lamon, Single- and Multilayered Interphases in SiC/SiC Composites Exposed to Severe Environmental Conditions: An Overview, *International Journal of Applied Ceramic Technology*, 7 (2010) 263-275.
- [41] Y. Katoh, S. Kondo, L.L. Snead, DC Electrical Conductivity of Silicon Carbide Ceramics and Composites for Flow Channel Insert Applications, *J. Nucl. Mater.*, 386 (2009) 639-642.
- [42] L.L. Snead, T.D. Burchell, Y. Katoh, Swelling of Nuclear Graphite and High Quality Carbon Fiber Composite Under Very High Irradiation Temperature, *J. Nucl. Mater.*, 381 (2008) 55-61.
- [43] Y. Katoh, T. Nozawa, L.L. Snead, K. Ozawa, H. Tanigawa, Stability of SiC and its Composites at High Neutron Fluence, *J. Nucl. Mater.*, 417 (2011) 400-405.
- [44] W. Yang, H. Araki, T. Noda, J.Y. Park, Y. Katoh, T. Hinoki, J.N. Yu, A. Kohyama, Hicalon (TM) fiber-reinforced CVI-SiC matrix composites: I. Effects of PyC and PyC-SiC multilayers on the fracture behaviors and flexural properties, *Materials Transactions*, 43 (2002) 2568-2573.
- [45] W. Yang, A. Kohyama, Y.T. Katoh, H. Araki, J.N. Yu, T. Noda, Effect of carbon and silicon carbide/carbon interlayers on the mechanical Behavior of tyranno-SA-fiber-reinforced silicon carbide-matrix composites, *J. Ameri. Ceram. Soc.*, 86 (2003) 851-856.
- [46] Y. Katoh, L.L. Snead, T. Nozawa, T. Hinoki, A. Kohyama, N. Igawa, T. Taguchi, Mechanical properties of chemically vapor-infiltrated silicon carbide structural composites with thin carbon interphases for fusion and advanced fission applications, *Materials Transactions*, 46 (2005) 527-535.
- [47] Y. Katoh, T. Nozawa, L.L. Snead, Mechanical properties of thin pyrolytic carbon interphase SiC-Matrix composites reinforced with near-stoichiometric SiC fibers, *J. Ameri. Ceram. Soc.*, 88 (2005) 3088-3095.
- [48] R.A. Lowden, Characterization and Control of the Fiber-Matrix Interface in Ceramic Matrix Composites, ORNL/TM-11039, in, Oak Ridge National Laboratory, Oak Ridge, 1989.
- [49] T. Nozawa, Y. Katoh, L.L. Snead, The effects of neutron irradiation on shear properties of monolayered PyC and multilayered PyC/SiC interfaces of SiC/SiC composites, *J. Nucl. Mater.*, 367 (2007) 685-691.
- [50] T.M. Besmann, B.W. Sheldon, R.A. Lowden, D.P. Stinton, Vapor-phase fabrication and properties of continuous-filament ceramic composites, *Science*, 253 (1991) 1104-1109.
- [51] T.M. Besmann, J.C. McLaughlin, H. Lin, Fabrication of ceramic composites: forced CVI, *J. Nucl. Mater.*, 219 (1995) 31-35.

- [52] T. Noda, A. Kohyama, Y. Katoh, Recent progress of SiC-fibers and SiC/SiC-composites for fusion applications, *Physica Scripta*, T91 (2001) 124-129.
- [53] T. Noda, H. Araki, H. Suzuki, F. Abe, Processing of carbon fiber/SiC composite for low activation, *Materials Transactions*, JIM, 34 (1993) 1122-1129.
- [54] A. Kohyama, Present status of NITE-SiC/SiC for advanced nuclear energy systems, in: 31st International Conference on Advanced Ceramics and Composites, Daytona Beach, 2007.
- [55] T. Hinoki, A. Kohyama, Current status of SiC/SiC composites for nuclear applications, *Annales de Chimie (Science des Materiaux)*, 30 (2005) 659-671.
- [56] Y. Katoh, S.M. Dong, A. Kohyama, Thermo-mechanical properties and microstructure of silicon carbide composites fabricated by nano-infiltrated transient eutectoid process, *Fusion Eng. Design*, 61-2 (2002) 723-731.
- [57] S.M. Dong, Y. Katoh, A. Kohyama, Processing optimization and mechanical evaluation of hot pressed 2D Tyranno-SA/SiC composites, *J. Eu. Ceram. Soc.*, 23 (2003) 1223-1231.
- [58] T. Koyanagi, T. Hinoki, K. Ozawa, Y. Katoh, The effect of neutron irradiation on the mechanical properties of NITE SiC/SiC composites, *J. Nucl. Mater.*, (submitted).
- [59] R.B. Matthews, Irradiation damage in reaction-bonded silicon carbide, *J. Nucl. Mater.*, 51 (1974) 203-208.
- [60] A.M. Carey, F.J. Pineau, C.W. Lee, J.C. Corelli, Radiation response of reaction-bonded and sintered SiC: effects of boron isotopes, *J. Nucl. Mater.*, 103&104 (1981) 789-794.
- [61] S. Suyama, Y. Itoh, A. Kohyama, Y. Katoh, Development of high strength reaction-sintered silicon carbide, *Journal of the Ceramic Society of Japan*, 109 (2001) 315-321.
- [62] Y. Katoh, M. Kotani, H. Kishimoto, W. Yang, A. Kohyama, Properties and radiation effects in high-temperature pyrolyzed PIP-SiC/SiC, *J. Nucl. Mater.*, 289 (2001) 42-47.
- [63] T. Nozawa, T. Hinoki, Y. Katoh, A. Kohyama, Effects of fibers and fabrication processes on mechanical properties of neutron irradiated SiC/SiC composites, *J. Nucl. Mater.*, 307 (2002) 1173-1177.
- [64] S. Bertrand, R. Pailler, J. Lamon, Influence of strong fiber/coating interfaces on the mechanical behavior and lifetie of Hi-Nicalon/(PyC/SiC)n/SiC minicomposites, *J. Ameri. Ceram. Soc.*, 84 (2001) 787-794.
- [65] J.Y. Yan, C.W. Chen, P.C. Fang, K.M. Yin, F.R. Chen, Y. Katoh, A. Kohyama, J.J. Kai, The investigation of crack mechanism for Tyranno-SA SiC/SiC composites with ESI method, *J. Nucl. Mater.*, 329 (2004) 513-517.
- [66] C.S. Kim, Oxidation Beahvior of SiC/SiC Composites in Chemically Controlled Gas Envriornment, in: Seminar at Oak Ridge National Laboratory, Oak Ridge, 2010.
- [67] G.A. Newsome, L.L. Snead, T. Hinoki, Y. Katoh, D. Peters, Evaluation of neutron irradiated silicon carbide and silicon carbide composites, *J. Nucl. Mater.*, 371 (2007) 76-89.
- [68] Y. Katoh, K. Ozawa, T. Hinoki, Y.B. Choi, L.L. Snead, A. Hasegawa, Mechanical Properties of Advanced SiC Fiber Composites Irradiated at Very High Temperatures, *J. Nucl. Mater.*, 417 (2011) 416-420.
- [69] T. Nozawa, Y. Katoh, L.L. Snead, T. Hinoki, A. Kohyama, Tensile and thermal properties of chemically vapor-infiltrated silicon carbide composites with various high-modulus fiber reinforcements, *Ceram. Eng. Sci. Proc.*, 26 (2005) 311-318.
- [70] T. Nozawa, E. Lara-Curzio, Y. Katoh, R.J. Shinavski, Tensile Properties of Advanced SiC/SiC Composites for Nuclear Control Rod Applications, in: E. Lara-Curzio (Ed.) *Mechanical Properties and Performance of Engineering Ceramics and Composites III*, Wiley, 2007, pp. 223-234.

- [71] T. Nozawa, K. Ozawa, Y.B. Choi, A. Kohyama, H. Tanigawa, Determination and prediction of axial/off-axial mechanical properties of SiC/SiC composites, *Fusion Eng. Design*, 87 (2012) 803-807.
- [72] Y. Katoh, T. Nozawa, L.L. Snead, T. Hinoki, A. Kohyama, Property tailorability for advanced CVI silicon carbide composites for fusion, *Fusion Eng. Design*, 81 (2006) 937-944.
- [73] Y. Katoh, L.L. Snead, T. Nozawa, S. Kondo, J.T. Busby, Thermophysical and Mechanical Properties of Near-Stoichiometric Fiber CVI SiC/SiC Composites after Neutron Irradiation at Elevated Temperatures, *J. Nucl. Mater.*, 403 (2010) 48-61.
- [74] G.N. Morscher, V.V. Pujar, Design Guidelines for In-Plane Mechanical Properties of SiC Fiber-Reinforced Melt-Infiltrated SiC Composites, *International Journal of Applied Ceramic Technology*, 6 (2009) 151-163.
- [75] D.B. Marshall, Indentation Method for Measuring Matrix-Fiber Frictional Stresses in Ceramic Composites, *J. Ameri. Ceram. Soc.*, 67 (1984) C259-C260.
- [76] A.G. Evans, J.-M. Domergue, E. Vagaggini, Methodology for relating the tensile constitutive behavior of ceramic-matrix composites to constituent properties, *J. Ameri. Ceram. Soc.*, 77 (1994) 1425-1435.
- [77] J. Lamon, F. Rebillat, A.G. Evans, Microcomposite test procedure for evaluating the interface properties of ceramic matrix composites, *J. Ameri. Ceram. Soc.*, 78 (1995) 401-405.
- [78] J.W. Hutchinson, H.M. Jensen, Models of fiber debonding and pullout in brittle composites with friction, *Mechanics of Materials*, 9 (1990) 139-163.
- [79] T. Nozawa, K. Ozawa, S. Kondo, T. Hinoki, Y. Katoh, L.L. Snead, A. Kohyama, Tensile, Flexural, and Shear Properties of Neutron Irradiated SiC/SiC Composites with Different Fiber-Matrix Interfaces, *J. ASTM. Int.*, 2 (2005) 12884-12881-12813.
- [80] E. Lara-Curzio, D. Bowers, M.K. Ferber, The Interlaminar Tensile and Shear Behavior of a Unidirectional C-C Composite, *J. Nucl. Mater.*, 230 (1996) 226-232.
- [81] E. Lara-Curzio, M.K. Ferber, Shear Strength of Continuous Fiber Ceramic Composites, in: Thermal and Mechanical Test Methods and Behavior of Continuous Fiber Ceramic Composites, ASTM STP 1309, ASTM International, West Conshohocken, PA, 1997, pp. 31-48.
- [82] T. Hinoki, Y. Maki, A. Kohyama, E. Lara-Curzio, L.L. Snead, Effect of interphase on transthickness tensile strength of high-purity silicon carbide composites, *Ceram. Eng. Sci. Proc.*, 25 (2004) 65-70.
- [83] Y.B. Choi, T. Hinoki, K. Ozawa, Y. Katoh, K. Matsugi, T. Kelimu, Transthickness Tensile Properties of NITE SiC/SiC Composite Irradiated at High Temperatures, *Materials Transactions*, 53 (2012) 2060-2063.
- [84] T. Nozawa, H. Tanigawa, J.S. Park, A. Kohyama, Fracture resistance of silicon carbide composites using various notched specimens, *Ceram. Eng. Sci. Proc.*, 30 (2009).
- [85] L.L. Snead, A.M. Williams, A.L. Qualls, Revisiting the Use of SiC as a Post Irradiation Temperature Monitor, in: M.L. Grossbeck, T.D. Allen, R.G. Lot, A.S. Kumar (Eds.) *The Effects of Radiation on Materials: 21st International Symposium*, ASTM STP 1447, ASTM International, West Conshohocken, PA, 2003.
- [86] E. Lara-Curzio, Properties of CVI-SiC Matrix Composites, *Comprehensive Composite Materials*, 4 (2000) 533-577.
- [87] K. Ozawa, T. Nozawa, Y. Katoh, T. Hinoki, A. Kohyama, Mechanical Properties and Microstructure of Advanced SiC/SiC composites after Neutron Irradiation, *J. Nucl. Mater.*, 367 (2007) 713-718.

- [88] M. Sawan, Y. Katoh, L.L. Snead, Transmutation of Silicon Carbide in Fusion Nuclear Environment, *J. Nucl. Mater.*, (Submitted).
- [89] K. Ozawa, Y. Katoh, L.L. Snead, T. Nozawa, T. Hinoki, A. Hasegawa, The effects of neutron irradiation on dimensional change in advanced silicon carbide composites, DOE/ER-0313/46 Fusion Reactor Materials Semiannual Progress Report for Period Ending June 30, 2009, (2009) 4-15.
- [90] R. Blackstone, E.H. Voice, The expansion of silicon carbide by neutron irradiation at high temperature, *J. Nucl. Mater.*, 39 (1971) 319-322.
- [91] R.J. Price, Neutron irradiation-induced voids in β -silicon carbide, *J. Nucl. Mater.*, 48 (1973) 47-57.
- [92] L.L. Snead, M.C. Osborne, R.A. Lowden, J. Strizak, R. Shinavski, K.L. More, W.S. Eatherly, J.L. Bailey, A.M. Williams, Low dose irradiation performance of SiC interphase SiC/SiC composites, *J. Nucl. Mater.*, 253 (1998) 20-30.
- [93] L.L. Snead, Y. Katoh, S. Connery, Swelling of SiC at Intermediate and High Irradiation Temperatures, *J. Nucl. Mater.*, 367 (2007) 677-684.
- [94] J.B.J. Hegeman, J.G. van der Laan, M. van Kranenburg, M. Jong, D.S. d'Hulst, P. ten Pierick, Mechanical and thermal properties of SiCf/SiC composites irradiated with neutrons at high temperatures, *Fusion Eng. Design*, 75-59 (2005) 789-793.
- [95] Y. Katoh, Final Report on Irradiation of Bonded-fiber SiC Composite, ORNL/TM-2012/201, in, Oak Ridge National Laboratory, Oak Ridge, 2010.
- [96] Y. Katoh, L.L. Snead, S.I. Golubov, Analyzing irradiation-induced creep of silicon carbide, in: E. Lara-Curzio (Ed.) *Mechanical Properties and Performance of Engineering Ceramics and Composites III*, Wiley, 2007, pp. 297-306.
- [97] Y. Katoh, A. Clerk, K. Ozawa, Dilatometry of irradiated silicon carbide as a method for determination of irradiation temperature, *Fusion Reactor Materials*, DOE/ER-0313/48, 48 (2010) 158-163.
- [98] T. Ishikawa, K. Bansaku, N. Watanabe, Y. Nomura, M. Shibuya, T. Hirokawa, Experimental stress/strain behavior of SiC-matrix composites reinforced with Si-Ti-C-O fibers and estimation of matrix elastic modulus, *Composites Science and Technology*, 58 (1998) 51-63.
- [99] G.E. Youngblood, R.H. Jones, A new type of SiC composite for fusion, in: *Fusion Materials*, Oak Ridge National Laboratory, 2000, pp. 112-120.
- [100] Y. Katoh, T. Nozawa, A.M. Williams, T. Cheng, P. Dou, L.L. Snead, Properties of Hi-Nicalon Type-S CVI SiC Composite Irradiated to 70 dpa at Elevated Temperatures, ORNL/TM-2012/459, in, Oak Ridge National Laboratory, 2012.
- [101] L.L. Snead, S.J. Zinkle, D.P. White, Thermal conductivity degradation of ceramic materials due to low temperature, low dose neutron irradiation, *J. Nucl. Mater.*, 340 (2005) 187-202.
- [102] R.J. Price, Thermal conductivity of neutron-irradiated pyrolytic β -silicon carbide, *J. Nucl. Mater.*, 46 (1973) 268-272.
- [103] D.J. Senor, G.E. Youngblood, L.R. Greenwood, D.V. Archer, D.L. Alexander, M.C. Chen, G.A. Newsome, Defect structure and evolution in silicon carbide irradiated to 1 dpa-SiC at 1100C, *J. Nucl. Mater.*, 317 (2003) 145-159.
- [104] L.L. Snead, Degradation in thermal conductivity of SiC and SiC composites, in: A. Kohyama, R.H. Jones, B. Riccardi (Eds.) *The Sixth IEA International Workshop on SiC/SiC Ceramic Composites for Fusion Applications*, Boston, 2004, pp. 197-208.

- [105] A. Pacault, A. Marchand, J. Amiell, E. Dupart, J. Rappeneau, C. Micaud, R. Wlodarsky, Thermal annealing of neutron-irradiated carbons; changes in electronic properties, *Carbon*, 10 (1971) 355.
- [106] G.E. Youngblood, R.J. Kurtz, R.H. Jones, SiC/SiC design for a flow channel insert, in: *Fusion Materials*, Oak Ridge National Laboratory, 2005, pp. 3-8.
- [107] G.N. Morscher, Modeling the elastic modulus of 2D woven CVI SiC composites, *Composite Sci. Tech.*, 66 (2006) 2804-2814.
- [108] Z. Hashin, Analysis of properties of fiber composites with anisotropic constituents, *Journal of Applied Mechanics*, 46 (1979) 543-550.
- [109] T.W. Chou, *Microstructural Design of Fiber Composites*, Cambridge University Press, New York, 1992.
- [110] M. Sakata, H. Ohnabe, Measurements of Orthotropic Elastic Constants of Ceramic Matrix Composites from Impact Sound, in: M.G. Jenkins, S.T. Gonczy, E. Lara-Curzio, N.E. Ashbaugh, L.P. Zawada (Eds.) *Thermal and Mechanical Test Methods and Behavior of Continuous-Fiber Ceramic Composites*, ASTM STP 1309, American Society for Testing and Materials, West Conshohocken, PA, 1997.
- [111] E. Vagaggini, J.-M. Domergue, A.G. Evans, Relationships between hysteresis measurements and the constituent properties of ceramic matrix composites: I, theory, *J. Ameri. Ceram. Soc.*, 78 (1995) 2709-2720.
- [112] J.-M. Domergue, E. Vagaggini, A.G. Evans, Relationships between hysteresis measurements and the constituent properties of ceramic matrix composites: II, experimental studies on unidirectional materials, *J. Ameri. Ceram. Soc.*, 78 (1995) 2721-2731.
- [113] T. Hinoki, E. Lara-Curzio, L.L. Snead, Mechanical properties of high purity SiC fiber-reinforced CVI-SiC matrix composites, *Fusion Science and Technology*, 44 (2003) 211-218.
- [114] J.M. Hodgkinson, *Mechanical Testing of Advanced Fibre Composites*, Woodhead Publishing Limited, Cambridge, 2000.
- [115] S.W. Tsai, E.M. Wu, A general theory of strength for anisotropic materials, *Journal of Composite Materials*, 5 (1970) 58-80.
- [116] T. Nozawa, Y. Katoh, A. Kohyama, Evaluation of tensile properties of SiC/SiC composites with miniaturized specimens, *Materials Transactions*, 46 (2005) 543-551.
- [117] T. Nozawa, T. Hinoki, Y. Katoh, A. Kohyama, E. Lara-Curzio, Specimen Size Effects on the Tensile Properties of 2D/3D SiC/SiC Composites, in: M.A. Sokolov, J.D. Landes, G.E. Lucas (Eds.) *Small Specimen Test Techniques: Fourth Volume*, ASTM STP 1418, ASTM International, West Conshohocken, PA, 2002, pp. 294-305.
- [118] T. Nozawa, Y. Katoh, A. Kohyama, E. Lara-Curzio, Specimen Size Effect on the In-Plane Shear Properties of SiC/SiC Composites, in: J.P. Singh, N.P. Bansal, M. Singh (Eds.) *Advances in Ceramic Matrix Composites VIII: Ceramic Transactions*, Vol. 139, The American Ceramic Society, Westerville, OH, 2002, pp. 127-138.
- [119] Y. Katoh, T. Nozawa, L.L. Snead, T. Hinoki, Effect of Neutron Irradiation on Tensile Properties of Unidirectional Silicon Carbide Composites, *J. Nucl. Mater.*, 367 (2007) 774-779.
- [120] W.A. Curtin, Theory of mechanical properties of ceramic-matrix composites, *J. Ameri. Ceram. Soc.*, 74 (1991) 2837-2845.
- [121] Y. Katoh, L.L. Snead, Mechanical Properties of Cubic Silicon Carbide after Neutron Irradiation at Elevated Temperatures, *J. ASTM. Int.*, 2 (2005) 12377-12371-12313.
- [122] S.T. Gonczy, M.G. Jenkins, Tensile and Flexure Properties of 2-D NicalonTM Reinforced SylramicTM S-200 Ceramic Matrix Composites, in: M.G. Jenkins, E. Lara-Curzio, S.T. Gonczy

- (Eds.) Mechanical, Thermal and Environmental Testing and Performance of Ceramic Composites and Components, ASTM STP 1392, American Society for Testing and Materials, West Conshohocken, PA, 2000.
- [123] E. Lara-Curzio, M.K. Ferber, Journal of Materials Science, 29 (1994) 6152-6158.
 - [124] P. Lawrence, Journal of Materials Science, 7 (1972) 1-6.
 - [125] R.J. Kerans, T.A. Parthasarathy, J. Ameri. Ceram. Soc., 74 (1991) 1585-1596.
 - [126] C.-H. Hsueh, Mater. Sci. Eng. A, 154 (1992) 125-132.
 - [127] C.-H. Hsueh, Mater. Sci. Eng. A, 165 (1993) 189-195.
 - [128] C. Liang, J.W. Hutchinson, Mechanics of Materials, 14 (1993) 207-221.
 - [129] D.K. Shetty, J. Ameri. Ceram. Soc., C107-109 (1988).
 - [130] T. Nozawa, L.L. Snead, Y. Katoh, J.H. Miller, Shear Properties at the PyC/SiC Interface of TRISO-Coating, J. Nucl. Mater., 371 (2007) 304-313.
 - [131] T. Nozawa, Y. Katoh, L.L. Snead, The effect of neutron irradiation on the fiber/matrix interphase of silicon carbide composites, J. Nucl. Mater., 384 (2009) 195-211.
 - [132] C. Sauder, A. Brusson, J. Lamon, International Journal of Applied Ceramic Technology, 7 (2010) 291-303.
 - [133] K. Ozawa, Y. Katoh, E. Lara-Curzio, L.L. Snead, T. Nozawa, Comparative Study of Tensile Properties of Uni-Directional Single-Tow SiC-Matrix Composites Reinforced with Various Near-Stoichiometric SiC Fibers, Ceram. Eng. Sci. Proc., 31 (2010) 207-220.
 - [134] E. Lara-Curzio, Comprehensive Composites Encyclopedia, in, Elsevier, 2000, pp. 545.
 - [135] S.R. Choi, N.P. Bansal, Interlaminar tension/shear properties and stress rupture in shear of various continuous fiber-reinforced ceramic matrix composites, Ceram. Trans., 175 (2006) 119-134
 - [136] T. Nozawa, Y. Choi, T. Hinoki, H. Kishimoto, A. Kohyama, H. Tanigawa, Tensile, Compressive and In-Plane/Inter-Laminar Shear Failure Behavior of CVI- and ITE-SiC/SiC Composites, IOP Conference Series: Materials Science and Engineering, 18 (2011) 162011.
 - [137] C. Shih, Y. Katoh, K. Ozawa, E. LARA-CURZIO, L.L. Snead, Trans-laminar Mechanical Properties of Chemical Vapor Infiltration and Nano-infiltration and Transient Eutectic-phase Processed SiC/SiC Composites, International Journal of Applied Ceramic Technology, (submitted).
 - [138] V. Kostopoulos, Y.Z. Pappas, Toughening Mechanisms in Long Fiber Ceramic Matrix Composites, Comprehensive Composite Materials, 4 (2000) 95-114.
 - [139] T. Nozawa, H. Tanigawa, Cracking resistance of silicon carbide composites by single- and double-notched specimen techniques, International Journal of Applied Ceramic Technology, 7 (2010) 304-315.
 - [140] V. Kostopoulos, Y.P. Markopoulos, Y.Z. Pappas, S.D. Peteves, J. Eu. Ceram. Soc., 18 (1998) 69.
 - [141] M. Sakai, K. Urashima, M. Inagaki, J. Ameri. Ceram. Soc., 66 (1983) 868.
 - [142] K. Ozawa, Y. Katoh, T. Nozawa, L.L. Snead, Effect of Neutron Irradiation on Fracture Resistance of Advanced SiC/SiC Composites, J. Nucl. Mater., 417 (2011) 411-415.
 - [143] K. Ozawa, Y. Katoh, T. Nozawa, T. Hinoki, L.L. Snead, Evaluation of Damage Tolerance of Advanced SiC/SiC Composites after Neutron Irradiation, IOP Conference Series: Materials Science and Engineering, 18 (2011) 162005.
 - [144] H.M. Yun, J.A. DiCarlo, Thermomechanical Characterization and Implications for CMC, NASA TM-1999-0209283, in, 1999.

- [145] J.A. DiCarlo, H.M. Yun, Non-Oxide (Silicon Carbide) Fibers, in: N.P. Bansal (Ed.) Handbook of Ceramic Composites, Kluwer Academic Publishers, Boston, 2005.
- [146] A.R. Bunsell, J. Renard, Fundamentals of Fibre Reinforced Composite Materials, Institute of Physics, London, 2005.
- [147] C. Sauder, J. Lamon, Tensile Creep Behavior of SiC-Based Fibers With a Low Oxygen Content, *J. Ameri. Ceram. Soc.*, 90 (2007) 1146-1156.
- [148] H.M. Yun, J.A. DiCarlo, Comparison of the tensile, creep, and rupture strength properties of stoichiometric SiC fibers, *Ceram. Eng. Sci. Proc.*, 20 (1999) 259-272.
- [149] C.H. Carter, Jr., R.F. Davis, J. Bentley, Kinetics and mechanisms of high-temperature creep in silicon carbide: II, chemically vapor deposited, *J. Ameri. Ceram. Soc.*, 67 (1984) 732-740.
- [150] Y. Katoh, L.L. Snead, T.D. Burchell, W.E. Windes, Composite Materials for High Temperature Reactors: Technology Development Roadmap, in: 5th International Conference on High Temperature Reactor Technology, Prague, 2010.
- [151] ASME Boiler Code Section NH, Class 1 Components in Elevated Temperature Service, American Society for Mechanical Engineers, New York, 2007.
- [152] R.M. McMeeking, Models for the Creep of Ceramic Matrix Composite Materials, in: S. Nair, K. Jakus (Eds.) High Temperature Mechanical Behaviour of Ceramic Composites, Butterworth-Heinemann, Burlington, 1995.
- [153] B. Schneider, A. Guette, R. Naslain, M. Cataldi, A. Costecalde, A theoretical and experimental approach to the active-to-passive transition in the oxidation of silicon carbide: Experiments at high temperatures and low total pressures, *Journal of Materials Science*, 33 (1998) 535-547.
- [154] E.A. Gulbransen, K.F. Andrew, F.A. Brassart, The Oxidation of Silicon Carbide at 1150° to 1400°C and at 9×10^{-3} to 5×10^{-1} Torr Oxygen Pressure, *Journal of the Electrochemical Society*, 113 (1966) 1311-1314.
- [155] R.H. Jones, C.H. Henager Jr., C.A. Lewinsohn, C.F. Windisch, Stress-Corrosion Cracking of Silicon Carbide Fiber/Silicon Carbide Composites, *J. Ameri. Ceram. Soc.*, 83 (2000) 1999-2005.
- [156] W. Gauthier, J. Lamon, Delayed Failure of Hi-Nicalon and Hi-Nicalon S Multifilament Tows and Single Filaments at Intermediate Temperatures (500°–800°C), *J. Ameri. Ceram. Soc.*, 92 (2009) 702-709.
- [157] W. Gauthier, F. Pailler, J. Lamon, R. Pailler, Oxidation of Silicon Carbide Fibers During Static Fatigue in Air at Intermediate Temperatures, *J. Ameri. Ceram. Soc.*, 92 (2009) 2067-2073.
- [158] J.K. Wright, W.R. Lloyd, Analysis of Potential Materials for the Control Rod Sleeves of the Next Generation Nuclear Plant, INL/EXT-06-11614, (2006).